Utilization of pedestal energy from pre-compressed pump pulse for high efficiency and enhanced tunability in soliton self-frequency shift

Fariha Mehjabin

Department of Electrical & Computer Engineering

McGill University

Montreal, Canada

June 2024

A thesis report submitted to McGill University in partial fulfillment of the requirement for the degree of Master of Science

Abstract

The soliton self-frequency shift (SSFS) phenomenon holds particular significance as it provides the opportunity to access the mid-infrared (MIR) (2-20 μm) spectral range, which has numerous applications in sensing and spectroscopy. SSFS is best observed with short pulse width; hence, a common approach to enhance SSFS involves the pre-compression of optical pulses prior to an SSFS stage. Higher-order soliton-effect compression involves the propagation of a higher-order soliton that results in a transitory temporal profile, which deviates from the ideal hyperbolic secant profile. This transitory temporal profile features a short main lobe, however, accompanied by side lobes, termed pedestal. There is thus a compromise to be made between shortening the main lobe and transferring energy to the pedestal. Pulse compression therefore impacts the energy conversion efficiency (ECE) of the SSFS process, where ECE is defined as the ratio of the red-shifted soliton's energy to the total output energy.

This thesis investigates the impact of the pedestal that evolves during the pulse pre-compression stage (a silica-based compressing fiber (CF)) on SSFS and ECE within the nonlinear fiber (NLF). It has been demonstrated that the energy transferred to the pedestal is partly recycled by the shifting soliton during the SSFS process, enhancing its ECE and overall wavelength shift.

Résumé

Le phénomène de décalage de fréquence de soliton (SSFS) revêt une importance particulière car il offre la possibilité d'accéder à la gamme spectrale de l'infrarouge moyen (MIR) (2-20 µm), qui a de nombreuses applications en détection et en spectroscopie. Le SSFS est mieux observé avec une largeur d'impulsion courte ; ainsi, une approche courante pour améliorer le SSFS implique la pré-compression des impulsions optiques avant une étape de SSFS. La compression des solitons d'ordre supérieur implique la propagation d'un soliton d'ordre supérieur qui entraîne un profil temporel transitoire, qui dévie du profil idéal en cosécante hyperbolique. Ce profil temporel transitoire présente un lobe principal court, mais accompagné de lobes latéraux, appelés pédestaux. Il y a donc un compromis à faire entre la réduction de la durée du lobe principal et le transfert d'énergie vers le pédestal. La compression des impulsions impacte donc l'efficacité de conversion énergétique (ECE) du processus de SSFS, où l'ECE est définie comme le rapport de l'énergie du soliton décalé vers le rouge à l'énergie totale en sortie.

Cette thèse étudie l'impact du pédestal qui évolue pendant la phase de pré-compression des impulsions (une fibre de compression à base de silice (CF)) sur le SSFS et l'ECE dans la fibre non linéaire (NLF). Il a été démontré que l'énergie transférée au pédestal est en partie recyclée par le soliton décalé pendant le processus de SSFS, améliorant ainsi son ECE et le décalage de longueur d'onde global.

Acknowledgments

I express my gratitude to the *Almighty Allah (SWT*) for granting me the opportunity to pursue my graduate studies.

I am deeply grateful to my thesis advisor, *Prof. Martin Rochette*, for offering me a graduate student position, providing financial support, and granting me the opportunity to conduct research in the fascinating field of Nonlinear Photonics. I would like to express my sincere appreciation to my colleague, *Hosne Mobarak Shamim*, from whom I had many opportunities to learn. His continuous assistance, valuable comments, and suggestions in the experimental and numerical analysis of this project have benefited me immensely and played a significant role in shaping the outcome of this research endeavor.

I am forever indebted to my mother *Farhana Naz*, my father *S M Motaher Hossain*, and my younger sister *Maisha Mehnaz* for their immense support and faith in me. I extend my gratitude to my friend and colleague *Md Moinul Islam Khan* for his constant encouragement and invaluable support throughout this entire journey. Additionally, I express my gratitude towards *Khadija bint Abdur Rouf*, *Nafila Farheen Aytija*, and *Progya Khan* for their constant guidance and inspiration, which greatly contributed to my well-being during my time abroad. I am thankful to my amazing roommates *Gershyn Marian Lobo* and *Hemapriya Sampathkumar*.

Table of Contents

List of Figures

List of tables

1. Chapter 1: Introduction

The MIR region typically ranges in wavelength from 2 to 20 μm, is crucial for numerous scientific and technical fields [1]. This spectral range is characterized by unique molecular absorption features, making it important for spectroscopy [2], chemical sensing [3], environmental monitoring [4], and medical diagnostics [5]. With the use of optical fibers, nonlinear wavelength conversion techniques such as optical parametric sideband conversion [6,7], supercontinuum generation [8–10], and soliton self-frequency shift (SSFS) [11] show potential as effective approaches for accessing the MIR region. Among those nonlinear wavelength conversion mechanisms, SSFS holds particular significance due to its ability to produce tunable and ultrashort pulses in MIR [12–14]. Unlike other wavelength conversion methods, it does not require an additional probe laser or temporal synchronization. Furthermore, the power spectrum density (PSD) of the SSFS pulse stays focused on a narrow range of wavelengths [14].

Generally, a mode-locked laser emits pulses within a specific spectral region due to its limited gain bandwidth. To achieve pulses in a different spectral region through SSFS, they are passed through a nonlinear optical fiber with anomalous dispersion (discussed in section 2.2). Then the Raman nonlinear effect (discussed in section 2.3.2) causes the pulses to shift continuously to longer wavelengths via an inelastic interaction that transfers a portion of energy to the red side of the spectrum. This is how a specific spectral region can be accessed through wavelength conversion via SSFS [15,16]. Incorporating a compression stage before injecting the pulses into optical nonlinear fibers can significantly enhance the system's performance by increasing the extent of the wavelength shift and improving ECE simultaneously. The following section will briefly discuss wavelength conversion through SSFS using the pre-compression technique.

1.1 Literature Review

SSFS is a consequence of intra-pulse Raman scattering where the blue portion of the soliton spectrum pumps the red portion of the spectrum, leading to a gradual redshift of the soliton spectrum with propagation distance [17]. Figure 1.1 illustrates that the entire spectrum is shifted towards the red due to the SSFS. The wavelength shift through SSFS is best observed with short pulse width, as it increases proportionally with the fourth power of inverse pulse duration [11,17]. Hence, fiber-based pulse pre-compression of the input pulse before the SSFS stage stands as a crucial technique for attaining high SSFS.

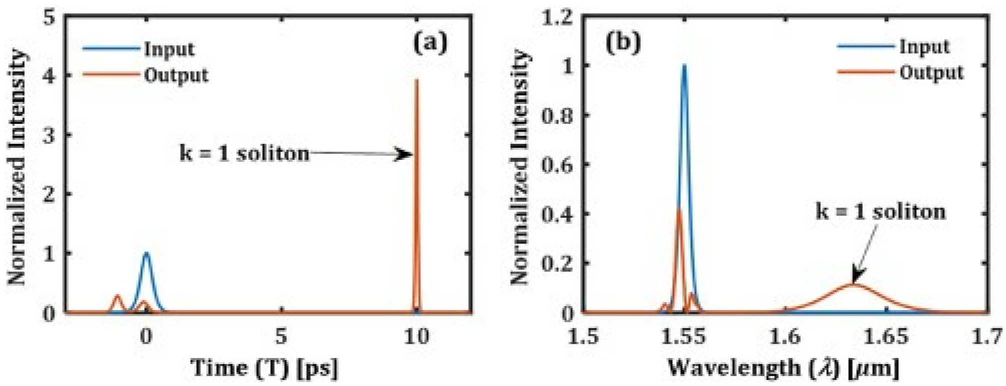

Figure 1.1. Simulated (a) temporal and (b) spectral evolution of SSFS process in a 15 m long fiber (taken from [18]*).*

Seed pulses with widths of a few picoseconds or less can be compressed to generate ultrashort pulses through various optical fiber-based compression techniques such as higher-order soliton-effect compression [19,20], adiabatic pulse compression with DDF (dispersion decreasing fiber) [21], self-similar pulse compression with nonlinear fiber Bragg gratings (FBGs) [22], intensity discrimination with the nonlinear induced birefringence in the fibers [23,24], and the nonlinear optical loop mirror (NOLM) [25]. Higher-order nonlinear fiber phenomena, such as stimulated Raman scattering (SRS) and higher-order dispersion are typically considered negligible for solitons within the picosecond range. However, the resulting soliton post-compression exhibits high peak powers, narrow widths (in the order of femtoseconds), and, consequently, extremely wide bandwidths (in the order of terahertz). In such scenarios, the impact of higher-order nonlinear effects becomes significant, leading to soliton fission and subsequent SSFS.

In addition to the initial compression of the input pulse, enhancing SSFS requires an increase in the energy input into the system. Earlier studies on SSFS [26–28] demonstrated that under high input energy conditions, although the short pulses with solitons of the higher order (N>2) are involved, the formation of higher-order solitons (as suggested by [29] and [30]) was not observed. Instead, the pulses undergo fission, giving rise to N number of fundamental solitons, each subsequently undergoing individual frequency shifts. In other words, as the higher-order soliton propagates through the nonlinear medium during the fission, it transfers energy to an expanding number of fundamental solitons. However, it's observed that with an increase in soliton order, the efficiency of the system tends to decrease as it reduces the fraction of energy imparted to the most spectrally shifted soliton [18,31]. This results in a reduction of ECE, defined as the ratio of the energy of the red-shifted soliton to the total output energy [16,32]. Therefore, while higher SSFS is achieved with higher soliton orders, there is a trade-off with reduced ECE. In a recent work, Shamim *et al.* demonstrated that employing pulse pre-compression with a CF before injecting it into the NLF allows for the retention of the soliton order within a specific range at the input of the NLF. This approach enables a wide range of soliton tunability while maintaining high ECE [31]. Here, this fiber-based pulse pre-compression process is facilitated by the higher-order soliton-effect compression method within the CF.

The technique of soliton-effect compression, a well-explored method in ultrafast optics, achieved significant development within a decade of its proposal in the early 1970s [33–35]. This approach relies on the interplay between self-phase modulation (SPM) and anomalous group velocity dispersion (GVD) to create optical soliton. The fundamental principle involves SPM broadening the spectral bandwidth, resulting in an up-chirp in the time domain. Simultaneously, anomalous GVD compensates for this induced up-chirp, leading to the compression of the temporal waveform [36]. For a fundamental or first-order soliton, the impact of SPM precisely counteracts the effects of anomalous GVD. Consequently, the soliton maintains its sech^2 shape without distortion as it propagates through a lossless optical fiber. Conversely, a high-order soliton experiences phases of periodic compression and broadening of its temporal and spectral form during propagation. This soliton initially narrows its pulse shape before restoring the original sech^2 profile at integral multiples of the soliton period. This characteristic behavior is exploited for the purpose of achieving pulse compression [20]. The crucial factors influencing pulse compression include the length of the fiber, the duration of the input pulse, and the input energy of the pulse. However, the compressed pulse achieved through higher-order soliton compression yields the evolution of a short main lobe surrounded by two side lobes, termed pedestal. There seems to be a compromise to make between shortening the main lobe and transferring energy toward the pedestal [20]. Thus, pulse compression has a significant impact on the ECE of the SSFS process.

This thesis investigates how the degree of pulse compression, determined by the length of the CF using the pre-compression technique, impacts the energy dynamics within the SSFS system. This analysis has demonstrated that the energy transferred to side lobes in the pre-compression stage is partially recycled by the moving soliton during SSFS in NLF, thereby increasing the overall wavelength shift and ECE.

1.2 Context

The work presented in this thesis took place in a context where the *Nonlinear Photonics Group* at McGill University has increased research interest in the fundamentals of soliton dynamics in dispersive and nonlinear fibers [11,12,14,18,31,37–39], where exploiting the compression of a high-order soliton was instigated further with Shamim [31,38], opening an exciting research avenue. This research fits well among other interests of the *Nonlinear Photonics Group*, such as the fabrication of all-fiber components, including tapers [40–55], optical fiber couplers [56–60], optical filters [61–67], and microspheres [68–70]; optical fiber devices such as spectroscopy instruments [71,72] and frequency-resolved optical gating devices [73,74]; and optical fiber sources such as wavelength converters [6,7,75–79], supercontinuum sources [8,9,80–83], frequency combs [84,85], Mamyshev oscillators [86–93] fiber lasers based on nonlinear gain [94–104], and fiber lasers based on resonant gain [105–110].

1.3 Thesis Outline

The thesis is divided into four chapters, where the first chapter includes the introduction and context to the topic. Chapter 2 provides a basic overview of wave propagation in optical fiber. Basic principles and theories pertaining to dispersion, nonlinearity, and solitonic effects are thoroughly discussed. These concepts are utilized throughout the rest of the thesis. In Chapter 3, a comprehensive study of the soliton pre-compression technique (Higher-order soliton-effect pulse compression) is provided, in addition to the detailed SSFS experimental setup with the pre-compression stage. The experimental result is then validated numerically to illustrate the influence of different CF lengths on the wavelength shift (via SSFS) when the compressed pulse is propagated through the NLF. Chapter 4 presents a comprehensive analysis of the impact of the pedestal in the context of SSFS in NLF, which originates from the pulse pre-compression in CF. Finally, a summary with the future scope of the work is presented.

2. Chapter 2: Basic Concepts

This chapter describes the fundamental idea behind light propagation in optical fibers. Following an introduction to the material's linear and nonlinear responses to an external optical field, the generalized nonlinear Schrödinger equation (GNLSE), which controls the propagation of light in optical fibers, is discussed. Finally, this section provides an explanation for the nonlinear phenomena related to the creation of optical solitons in the fibers and several solitonic effects in the context of GNLSE. This chapter provides the theoretical framework required to understand the work presented in the rest of the thesis.

2.1 Pulse Propagation in Optical Fiber

Total internal reflection (TIR) is the basic principle behind the guiding of the light in the optical fiber. Figure 2.1 shows an optical fiber consisting of a cylindrical dielectric core of refractive index n_1, surrounded by a cladding dielectric of refractive index n_2. TIR takes place only when $n_1 > n_2$ and for light rays with an angle of incidence that is higher than the critical angle defined as $\theta_c = \sin^{-1}\left(\frac{n_2}{n_1}\right)$.

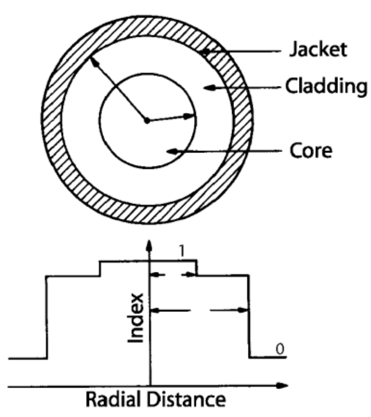

Figure 2.1. Schematic illustration of the cross-section and the refractive-index profile of a step-index fiber[taken from [111]].

Light entering a fiber within a cone of acceptance angle can propagate along the fiber as guided modes. Incident light beyond this acceptance angle radiates into the cladding and decays. Two parameters that characterize an optical fiber are the numerical aperture (NA):

$$\mathrm{NA} = (n_1^2 - n_2^2)^{\frac{1}{2}} \tag{2.1}$$

and the V number which is expressed as:

$$V = \frac{2\pi}{\lambda} a(n_1^2 - n_2^2)^{\frac{1}{2}} = \frac{2\pi a}{\lambda} \mathrm{NA} \tag{2.2}$$

Where a is the core radius, and λ is the wavelength of light. The V parameter determines the number of modes propagating through the fiber. If $V < 2.405$, the optical fiber supports only one mode; termed as the single mode fiber. Throughout this thesis (both in numerical and experimental section), we have only used the single mode fibers.

Another important characteristic of the fiber is loss. If the input power is P_0, the transmitted power after a fiber length of L is P_t, and the attenuation constant is α (dB/km). It can be expressed as:

$$\alpha_{\mathrm{dB}} = -\frac{10}{L} \log\left(\frac{P_T}{P_0}\right) \tag{2.3}$$

Impurities present in glasses are responsible for losses. Metal residues and OH^- ions from water vapor increase the light absorption coefficient. Rayleigh scattering arises from random density fluctuations in the material, causing local fluctuations in the refractive index. Consequently, light is scattered in all directions. This phenomenon is characterized by a dependence on the inverse fourth power of the wavelength (λ^{-4}), making it less pronounced at longer wavelengths. Losses can also be caused by fiber bending and light scattering at the core-cladding interface [111]. Moreover, multiple splicing or cabling might increase the total optical loss of fiber.

2.2 Dispersion

When light interacts with the bound electrons of the dielectric, the response from the medium depends on the optical frequency ω. This wavelength-dependent behavior of the refractive index (RI), denoted as $n(\lambda)$ is referred to as chromatic dispersion. This behavior arises from characteristic resonances within the material, which establish a correlation between the RI and the absorption coefficient, as described by the Kramers-Kronig relations [112]. Far from the material resonances, the refractive index is well approximated by the Sellmeier equation.

$$n^2(\omega) = 1 + \sum_{j=1}^{m} \frac{B_j \omega_j}{\omega_j^2 - \omega^2} \tag{2.4}$$

Where ω_j is the resonance frequency and B_j is the strength of j^{th} resonance. For optical fibers, the ω_j and B_j parameters are found experimentally by fitting the dispersion curve to equation 2.4. In the case of bulk-fused silica, these parameters are found by considering $m = 3$, and the parameters are mentioned in the following table [111]:

Table 2.1. Resonance wavelengths and amplitude coefficients of bulk silica.

Resonant Wavelength, λ_j [μm]	**Resonance Amplitude, B_j**
0.0684043	0.6961663
0.1162414	0.4079426
9.896161	0.8974794

where $\lambda_j = \frac{2\pi c}{\omega_j}$ and c is the speed of light in vacuum. Figure 2.2 shows the wavelength-dependent refractive index for fused silica.

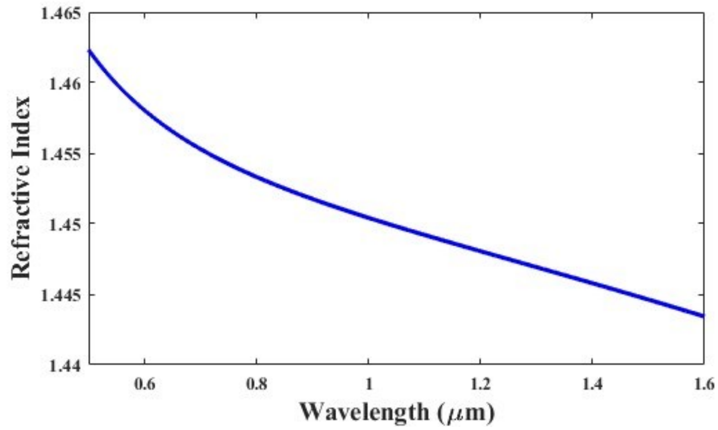

Figure 2.2. The linear refractive index of fused silica as a function of wavelength, calculated from eq. 2.1.

Short optical pulse propagation depends on fiber dispersion since the spectral components of the pulse move at different speeds, which are determined by $c/n(\omega)$. The effects of fiber dispersion are taken into consideration by expanding the mode-propagation constant β in a Taylor series at the frequency ω_0, which is the center of the pulse spectrum:

$$\beta(\omega) = \eta(\omega)\frac{\omega}{c} = \beta_0 + \beta_1(\omega - \omega_0) + \frac{1}{2}\beta_2(\omega - \omega_0)^2 + \cdots, \tag{2.5}$$

Where $\beta_m = \left(\frac{d^m\beta}{d\omega^m}\right)_{\omega=\omega_0}$ and $m = 0, 1, 2, \ldots$

β_m terms represent dispersion coefficients of different orders where β_1 and β_2 are related to the refractive index through the following relation:

$$\beta_1 = \frac{1}{v_\mathrm{g}} = \frac{n_\mathrm{g}}{c} = \frac{1}{c}\left(n + \omega\frac{dn}{d\omega}\right) \tag{2.6}$$

$$\beta_2 = \frac{1}{c}\left(2\frac{dn}{d\omega} + \omega\frac{d^2n}{d\omega^2}\right) \tag{2.7}$$

Where n_g is the group index and v_g is the group velocity.

β_2 represents the GVD, which accounts for the varying propagation speeds of different frequency components associated with the pulse. This phenomenon is also responsible for pulse broadening in the temporal domain. In general, the dispersion coefficient β_2 is taken solely into account when discussing pulse propagation. When the pulse width is ultrashort (less than 1 ps) or $\beta_2 \approx 0$, the third-order term β_3 has to be included. The dispersion parameter D, expressed as $d\beta_1/d\lambda$, is related to β_2 as follows:

$$D = \frac{d\beta_1}{d\lambda} = -\frac{2\pi c}{\lambda^2}\beta_2 = -\frac{\lambda}{c}\frac{d^2 n}{d\lambda^2} \tag{2.8}$$

The dispersion slope S is used to provide information on higher-order dispersion and is expressed as:

$$S = \frac{dD}{d\lambda} = \left[\frac{2\pi c}{\lambda^2}\right]^2 \beta_3 \tag{2.9}$$

It is important to distinguish between two dispersion regimes based on the sign of GVD. In the normal dispersion regime ($\beta_2 > 0$), the group velocity increases with wavelength, whereas in the anomalous dispersion regime ($\beta_2 < 0$), it is the opposite. In other words, in the normal dispersion regime, longer wavelengths (red components of the spectrum) travel faster than the shorter ones (blue components of the spectrum), whereas, with the anomalous dispersion regime, shorter wavelengths travel faster than longer ones. The wavelength at which two dispersion regimes cross and the sign is reversed for longer wavelengths is called the zero-dispersion wavelength (ZDW). Figure 2.3 shows the dispersive behavior of fused bulk silica, where the ZDW is around 1.27 μm.

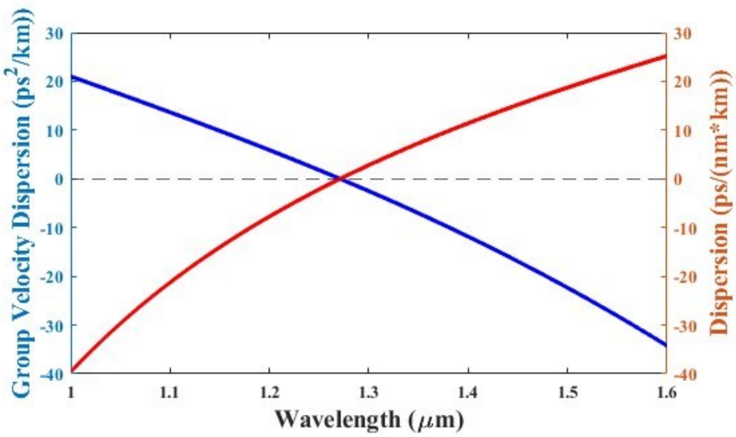

Figure 2.3. The GVD spectrum of fused silica as a function of wavelength.

For the reasons listed below, the dispersion characteristics of the silica glass fibers may differ from the curve displayed in Figure 2.3. First, doping with GeO_2 and P_2O_2 may exist in the fibers. The degree of doping in various materials determines the dispersion properties. Secondly, the overall dispersion in the fiber may differ slightly from Figure 2.3 owing to the waveguide contribution in addition to the material contribution. ZDW of the fiber can be shifted to a certain extent as a result of this waveguide contribution.

2.3 Fiber Nonlinearities

In linear optics, the polarization density P has a linear relationship with the electric field E, such that $P = \varepsilon_0 \chi E$, where ε_0 is the vacuum electric permittivity, χ represents the linear contribution to the polarization, the effects of which are included as attenuation and dispersion in sections 2.1 and 2.2. During light propagation in a medium, the polarization P is the sum of all dipole contributions and is not always linear concerning E. A Taylor series expression can be used to describe the polarisation caused by the medium's electric dipoles in response to an external electromagnetic field.

$$P = \varepsilon_0 \left[\chi^{(1)} : E + \chi^{(2)} : EE + \chi^{(3)} : EEE + \cdots \right] \quad (2.10)$$

where $\chi^{(i)}$ is i-th order susceptibility.

$\chi^{(1)}$ represents the linear contribution to the polarization whereas the second-order susceptibility $\chi^{(2)}$ requires a non-centrosymmetric medium available in crystals. In such media, both the second harmonic generation (SHG) and the Pockels effect have been documented [113]. Applications utilizing $\chi^{(2)}$ nonlinearity includes the measurement of ultrashort pulses and light modulation using devices like Mach-Zehnder interferometers (MZI). Silica-based optical fiber glasses possess an inherent centrosymmetric structure on a macroscopic level which forces the second-order and the subsequent even higher-order susceptibilities to vanish, leaving the $\chi^{(3)}$ term as the most dominant nonlinear contribution to the polarization. Hence, the silica-based fibers only respond to the $\chi^{(3)}$ based nonlinearity that gives rise to the Kerr effect and Raman scattering.

2.3.1 Nonlinear Refraction

Nonlinear refraction, also known as the Kerr effect is a process that refers to the intensity dependence of the RI. In its simplest form, the RI is expressed as:

$$n(\omega, I) = n_0(\omega) + n_2 I = n_0(\omega) + n_2 |E|^2 , \qquad \alpha(\omega, I) = \alpha_0(\omega) + \alpha_2 |E|^2 \quad (2.11)$$

where n_0 is the linear part given by equation 2.1, I is the optical intensity in the fiber associated with the EM field E. n_2 is the nonlinear index coefficient, which is theoretically related to the real part of $\chi^{(3)}_{xxxx}$ by the following expression.

$$n_2 = \frac{3}{8n_0} Re(\chi^{(3)}_{xxxx}) , \qquad \alpha_2 = \frac{3\omega_0}{4n_0 c} Im(\chi^{(3)}_{xxxx}) \quad (2.12)$$

As α_2 is insignificant for silica fibers, we neglect it in what follows. Despite being a fourth-rank tensor, $(\chi^{(3)}_{xxxx})$ has only one component contributing when the EM field is linearly polarized. This is considered the dielectric response when an intense EM field perturbs the electronic molecule structure and gives rise to an intensity-dependent alteration in polarizability. The bound electron clouds can be distorted by the applied field within a few femtoseconds. Accordingly, for pump pulses lasting a few hundred femtoseconds or less, this electrical response can be regarded as an instantaneous effect. The intensity dependence of the refractive index leads to numerous nonlinear effects, among which self-phase modulation (SPM) is widely known and covered in section 2.4.

2.3.2 Raman Scattering

Third-order susceptibility $\chi^{(3)}$ governs the nonlinear effects, which are elastic in the sense that there is no energy exchange between the dielectric medium and the electronic field. However, in stimulated inelastic scattering, a portion of the optical field's energy is transferred to the nonlinear medium, giving rise to a second class of nonlinear effects. This category includes two major nonlinear effects in optical fibers that are pertinent to silica vibrational excitation modes. These phenomena, known as stimulated Raman scattering (SRS) and stimulated Brillouin scattering (SBS), were among the earliest nonlinear effects discovered in optical fibers [111]. With CW and quasi-CW light up to the ns pulse duration, SBS is the most dominant nonlinear process in silica fibers. For pulses with a duration less than the ps range, Raman scattering becomes the dominant [27].

For short pulses with pulse width < 1 ps, the spectrum becomes wide. If the spectrum of the pulses is wide enough (> 1 THz), the Raman gain can amplify the low-frequency components of a pulse by transferring energy from the high-frequency components of the same pulse. This phenomenon is called intrapulse Raman scattering. As a result, the pulse spectrum shifts toward the low-frequency (red) side as the pulse propagates inside the fiber, and SSFS happens.

The Raman response function $R(t)$ includes both the Kerr and Raman contributions and is given by:

$$R(t) = (1 - f_{\mathrm{R}})\delta(t) + f_{\mathrm{R}} h_{\mathrm{R}}(t) \tag{2.13}$$

where f_R represents the fractional contribution of the delayed Raman response to nonlinear polarization, $\delta(t)$ is the Dirac delta function, which is assumed to be instantaneous. $h_R(t)$ is the delayed Raman response function originating from photon-phonon interaction [114]. $h_R(t)$ can be determined from the following equation [115].

$$h_{\mathrm{R}}(t) = (\tau_1^{-2} + \tau_2^{-2})\tau_1 \exp\left(-\frac{t}{\tau_2}\right) \sin\left(\frac{t}{\tau_1}\right) \tag{2.14}$$

Here, $1/\tau_1$ and $1/\tau_2$ are the phonon frequency associated with stimulated Raman scattering and the bandwidth of the Raman gain spectrum or inversed phonon lifetime, respectively [114]. τ_1 and τ_2 are respectively 12.2 fs and 32 fs for silica fibers [111]. The Raman gain is given by the imaginary part of the $h_{\mathrm{R}}(t)$ in the frequency domain.

$$g_{\mathrm{R}}(\omega) = \frac{2\omega_{\mathrm{p}}}{c_0} n_2 f_{\mathrm{R}} \mathrm{Im}\left(\tilde{h}_{\mathrm{R}}(\Delta\omega)\right) \tag{2.15}$$

Where $\Delta\omega = \omega - \omega_0$ and Im indicates the imaginary part. The f_{R} can be approximated from equation 2.15 and found to be 0.18 for silica fibers [114]. Figure 2.4 shows the normalized Raman gain spectra of silica and the temporal form of the Raman response function estimated from the gain data.

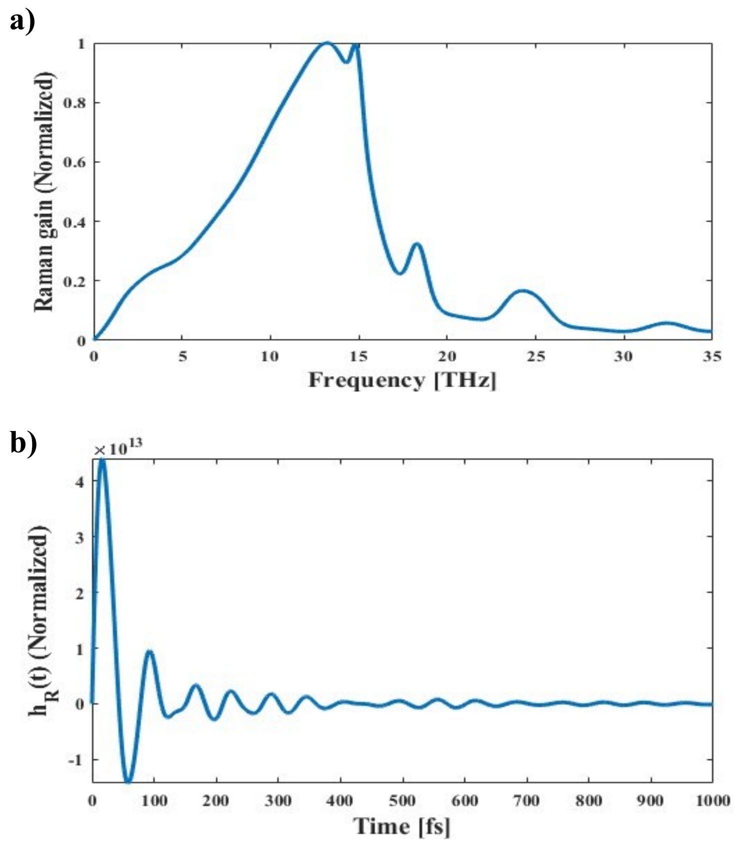

Figure 2.4. (a) Measured Raman gain spectrum of silica fibers. (b) The temporal form of the Raman response function [taken from [111]*]*

2.4 Generalized Nonlinear Schrödinger Equation

The propagation of the light inside a fiber can be modeled by solving the Maxwell equations:

$$\nabla \times E = -\frac{\partial B}{\partial t} \tag{2.16}$$

$$\nabla \times H = J + \frac{\partial D}{\partial t} \tag{2.17}$$

$$\nabla . D = \rho f \tag{2.18}$$

$$\nabla . B = 0 \tag{2.19}$$

Here, B is the magnetic flux density, D is the electric flux density, ρf is the source of the EM field, E is the electric field, H is the magnetic field and J is the current density. For optical fibers, $J = 0$ and $\rho f = 0$. Electric and magnetic fields are related to flux densities as follows:

$$B = \mu_0 H + M \tag{2.20}$$

$$D = \varepsilon_0 E + P \tag{2.21}$$

where μ_0 is the vacuum permeability, ε_0 is the vacuum permittivity, and P and M are the induced electric and magnetic polarizations. For a nonmagnetic medium such as optical fibers, $M = 0$. B and D in equations 2.16 and 2.17 are replaced by equations. 2.20 and 2.21 by the following equations:

$$\nabla \times E = -\frac{\partial}{\partial t}(\mu_0 H) \tag{2.22}$$

$$\nabla \times H = -\frac{\partial}{\partial t}(\varepsilon_0 E + P) \tag{2.23}$$

By replacing Equation 2.23 in the curl of equation 2.22 and using the relation $\varepsilon_0 = \frac{1}{\mu_0 c^2}$, where c is the speed of light in vacuum, it is rewritten as:

$$\nabla \times \nabla \times E = -\frac{1}{c^2}\frac{\partial^2 E}{\partial t^2} - \mu_0 \frac{\partial^2 P}{\partial t^2} \tag{2.24}$$

If we consider the polarization effects are governed by third-order nonlinearity, $\chi^{(3)}$, P consists of two parts:

$$P(r,t) = P_L(r,t) + P_{\mathrm{NL}}(r,t) \tag{2.25}$$

where P_L is the linear part and P_{NL} is the nonlinear part. As $\nabla \times \nabla \times E = \nabla(\nabla.E) - \nabla^2 E$ and $\nabla.E = 0$, the equation 2.25 can be expressed as:

$$\nabla^2 E = \frac{1}{c^2}\frac{\partial^2 E}{\partial t^2} + \mu_0 \frac{\partial^2 P_{\mathrm{L}}}{\partial t^2} + \mu_0 \frac{\partial^2 P_{\mathrm{NL}}}{\partial t^2} \tag{2.26}$$

It is assumed that the pulse retains its polarization for the duration of its propagation. The fast-varying component is isolated in this slowly varying envelope approximation and the electric field is written as,

$$E(r,t) = \frac{1}{2}\hat{x}\left[E(r,t)e^{-i\omega_0 t} + \mathrm{c.c}\right] \tag{2.27}$$

where $\hat{x}$ is the polarization unit vector and ω_0 is the center frequency of the pulse. If P_{NL} is assumed to be instantaneous, it can be expressed as:

$$P_{\mathrm{NL}}(r,t) \approx \epsilon_0 \epsilon_{\mathrm{NL}} E(r,t) \tag{2.29}$$

Here, $\epsilon_{\mathrm{NL}} = \frac{3}{4}\chi^{(3)}_{xxxx}|E(r,t)|^2$ indicates the nonlinear contribution to the dielectric constant.

This section provides a basic overview of the derivation; a more thorough explanation is provided in Agrawal's textbook [111]. The separation of the variable method is used to represent the electric field in equation 2.27, where $F(x,y)$ is the radial field distribution, β_0 is the propagation constant at the center frequency, and $A(z,t)$ is the slowly varying function.

$$E(r,t) = \frac{1}{2}\{F(x,y)A(z,t)\exp[i(\beta_0 z - \omega_0 t)] + \mathrm{c.c}\}\hat{x} \tag{2.30}$$

Using equation 2.30 and considering both the linear and nonlinear propagation dynamics in an optical fiber a new pulse propagation equation, the standard nonlinear Schrödinger equation (NLSE) is estimated in the following form:

$$\frac{\partial A}{\partial z} + \beta_1 \frac{\partial A}{\partial t} + i\beta_2 \frac{\partial^2 A}{\partial t^2} + \frac{\alpha}{2}A = i\gamma(\omega_0)|A|^2 A \tag{2.31}$$

Here, γ is the new nonlinear parameter known as the waveguide nonlinearity and is defined as:

$$\gamma(\omega_0) = \frac{\omega_0 n_{2\mathrm{I}}}{cA_{\mathrm{eff}}} \tag{2.32}$$

where A_{eff} is the effective area of the fundamental mode, represented as:

$$A_{\mathrm{eff}} = \frac{\left(\iint_{-\infty}^{+\infty} |F(x,y)|^2 dxdy\right)^2}{\iint_{-\infty}^{+\infty} |F(x,y)|^4 dxdy} \tag{2.33}$$

$n_{2\mathrm{I}}$ is the nonlinear refractive index, which is related to n_2 as, $n_{2\mathrm{I}} = 2n_2/\varepsilon_0 nc$. Equations 2.6 and 2.7 yield two dispersion coefficients, β_1 and β_2, which incorporate dispersion effects. The nonlinear losses are disregarded and the absorption coefficient α accounts for the linear fiber losses.

The intensity dependence of a medium's refractive index n, caused by the Kerr effect, is the source of the nonlinear effect. Therefore, spectral broadening results from the introduction of a nonlinear phase shift in the frequency domain. Dispersion, loss, self-steepening, and the Raman effect are ignored in order to examine a pure SPM effect. The NLSE can be written as:

$$\frac{\partial A}{\partial z} = i\gamma(\omega_0)|A|^2 A \tag{2.34}$$

The general solution of equation 2.34 is:

$$A(z,T) = A(0,T)\exp\big(i\phi_{\mathrm{NL}}(z,T)\big) \tag{2.35}$$

where the intensity-dependent phase shift ϕ_{NL} defined as:

$$\phi_{\mathrm{NL}}(z,T) = |A(0,T)|^2 \left(\frac{L_{\mathrm{eff}}}{L_{\mathrm{NL}}}\right) \tag{2.36}$$

where L_{eff} and L_{NL} are the effective length and nonlinear length respectively and expressed as:

$$L_{\mathrm{eff}} = \frac{1-\exp(-\alpha L)}{\alpha}, \qquad L_{\mathrm{NL}} = \frac{1}{\gamma P_0} \tag{2.37}$$

Here, P_0 is the peak power of the pulse and L is the length of the fiber. The maximum value of phase shift occurs at the pulse center located at $T = 0$. By normalizing the envelope such that $|A(0,0)| = 1$, it is given by:

$$\phi_{\max} = \frac{L_{\text{eff}}}{L_{\text{NL}}} = \gamma P_0 L_{\text{eff}} \tag{2.38}$$

Since the SPM effect induces a time-dependent phase shift, that leads to the instantaneous frequency shift of the pulse, which is understood as:

$$\delta\omega(T) = -\frac{\partial \phi_{\text{NL}}}{\partial T} = -\left(\frac{L_{\text{eff}}}{L_{\text{NL}}}\right)\frac{\partial}{\partial T}|A(0,T)|^2 \tag{2.39}$$

While the temporal profile remains unchanged, Figure 2.5 illustrates how the SPM effect causes the spectral broadening of an originally unchipped Gaussian pulse as it propagates through the fiber.

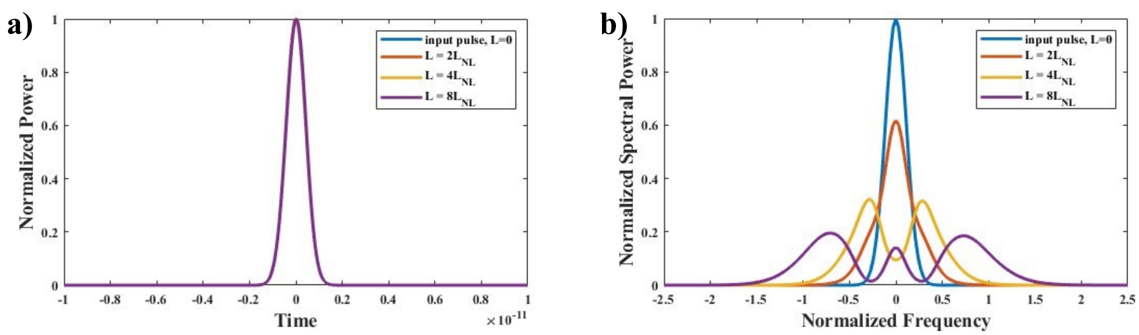

Figure 2.5. (a) Temporal profile (b) Spectrum generated for 1 ps Gaussian pulse with $\beta_2 = 0$, $\gamma = 2 \times 10^{-3} W^{-1} m^{-1}$

In NLSE, the nonlinear polarization consists of only instantaneous response like SPM. The overall nonlinear response function $R(t)$ considers both the instantaneous response (Kerr effect) and the delayed molecular effect (Raman effect). Now the nonlinear polarization P_{NL} can be estimated as:

$$P_{\text{NL}}(r,t) = \frac{3\epsilon_0}{4}\chi^{(3)}_{xxxx}E(r,t)\int_0^\infty R(t')|E(r,t-t')|^2 dt' \tag{2.40}$$

Here is the generalized pulse propagation equation, which takes into consideration the higher-order terms of the propagation constant and the frequency dependence of γ and α.

$$\frac{\partial A(z,t)}{\partial z} + \frac{1}{2}\left(\alpha(\omega_0) + i\alpha_1 \frac{\partial}{\partial t}\right)A - i\sum_{n=1}^{\infty} \frac{i^n \beta_n}{n!}\frac{\partial^n A}{\partial t^n}$$
$$= i\left(\gamma(\omega_0) + i\gamma_1 \frac{\partial}{\partial t}\right)A(z,t)\int_0^{\infty} R(t')|A(z,t-t')|^2 dt') \tag{2.41}$$

If there are enough higher-order dispersion terms in the equation, it can be applied to pulse lengths as short as a few optical cycles. Here, $\gamma_1 = (\partial\gamma/\partial\omega)_{\omega=\omega_0}$, where the frequency dependency of both $n_{2\mathrm{I}}$ and A_{eff} is incorporated and the ratio γ_1/γ represented as follows:

$$\frac{\gamma_1(\omega_0)}{\gamma(\omega_0)} = \frac{1}{\omega_0} + \frac{1}{n_2}\left(\frac{dn_2}{d\omega}\right)_{\omega=\omega_0} - \frac{1}{A_{\mathrm{eff}}}\left(\frac{dA_{\mathrm{eff}}}{d\omega}\right)_{\omega=\omega_0} \tag{2.42}$$

In the context of this thesis, only the first term is considered significant and can lead to self-steepening and group velocity dependence on light intensity.

In the numerical example presented in this work, n_2 will be considered constant because silica has a negligible contribution to the $\gamma(\lambda)$ for the range of λ used in this thesis. For silica, losses vary significantly with wavelength between 2.2~3 μm [31]. Since the pulse center wavelengths used in this thesis do not exceed 2.2 μm, the fiber losses are considered a constant value to simplify the equation.

2.5 Numerical Method

As the GNLSE is a nonlinear partial differential equation, only under certain conditions there will be an analytical solution to the GNLSE. To study pulse propagation in optical fiber, encompassing both linear and nonlinear effects, a numerical technique is therefore necessary. In this section, the split-step Fourier method (SSFM) and an updated version of SSFM with an adaptive step size method are introduced for solving GNLSE.

2.5.1 Split-step Fourier Method

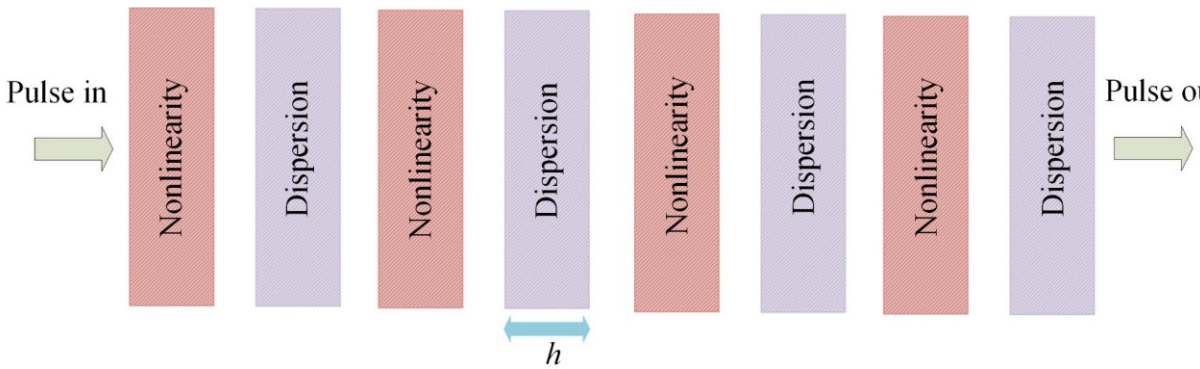

Figure 2.6. Schematics of SSFM.

The GNLSE is a partial differential equation with no analytical solution, which is solved numerically using the split-step Fourier method (SSFM). The GNLSE can be expressed as follows considering the time frame, $T = t - z/v_g$; where the pulse is at a group velocity v_g:

$$\frac{\partial A}{\partial z} = (\widehat{D} + \widehat{N})A \tag{2.43}$$

The dispersion operator $\widehat{D}$ accounts for linear propagation features, including dispersion and losses, while the nonlinear operator $\widehat{N}$ determines nonlinear effects during pulse propagation.

$$\widehat{D} = -\sum_{n=1}^{\infty} \frac{i^{n-1}\beta_n}{n!}\frac{\partial^n A}{\partial t^n} - \frac{\alpha}{2} \tag{2.44}$$

$$\widehat{N} = i\big(\gamma(\omega_0)\big)\int_0^{\infty} R(t')|A(z, t - t')|^2 dt') \tag{2.45}$$

The entire propagation length in SSFM is split up into small segments, h, and for each segment, the dispersion and nonlinearity are treated independently to yield an approximate solution of equation 2.37. Whereas in the second stage, $\widehat{N} = 0$ and dispersion acts alone, in the first step nonlinearity acts alone and $\widehat{D}$ is set to zero. Figure 2.6 shows an illustration of this procedure.

2.5.2 Adaptive Step Size Method

In order to accurately model the effects of the nonlinearity and dispersion, h should be much smaller than the nonlinear length, L_{NL} and dispersion length, L_{D}:

$$h \ll L_{\mathrm{NL}} = \frac{1}{\gamma P_0}\,, \qquad h \ll L_{\mathrm{D}} = \frac{T_0^2}{\beta_2} \tag{2.46}$$

where P_0 is the peak power, and T_0 is the pulse width. With appropriate peak power, pulse width, and fiber characteristics, higher order soliton is formed (discussed in detail in section 2.6.1). If the fiber has enough perturbations (higher-order dispersion and nonlinearity), then the higher-order soliton breaks into several fundamental solitons with variable peak power and pulse duration. This is termed soliton fission, which is explained in the later section 2.6.2. So, the condition $h \ll L_{\mathrm{NL}}$ can change during the propagation through the fiber. Hence, the choice of h is not quite straightforward in this case.

To accommodate for this, our methods employ an adaptive step size method known as the nonlinear phase-rotation method (see [8,116] for more information). With this method, the step size h is adjusted at each iteration by restricting the nonlinear phase-shift, $\phi_{\mathrm{NL}} = \gamma P_0 L$ to a small enough value. For a train of soliton pulses, the maximum phase shift ($\phi_{\max}$) is computed using the maximum soliton peak power P_0, which is obtained from equation 2.38. For each iteration i, the step size h is calculated as follows:

$$h(i) = \frac{\phi_{\max}}{\gamma P_0(i)} \tag{2.47}$$

2.6 Soliton and Solitonic Effects

In this section, the formation of soliton and other solitonic effects like dispersive wave, and Raman-induced SSFS are discussed.

2.6.1 The Formation of Soliton

During propagation in the fiber, an optical pulse with anomalous GVD experiences both nonlinear and linear chirps from the effect of SPM and GVD, respectively. These combined effects result in a pulse with a stable or periodically changing temporal and spectral profile. These nonlinear waves are referred to as optical solitons. Zakharov and Shabat used the inverse scattering method in 1971 to solve the NLS equation [117]. If this equation is analytically solved without higher-order perturbation, sech solution of the optical soliton can be achieved. The hyperbolic secant input pulse takes the following form:

$$A(0,T) = \sqrt{P_0}\,\mathrm{sech}\left(\frac{T}{T_0}\right) \tag{2.48}$$

In practice, several higher-order effects perturb the soliton as they propagate through the fiber. A soliton's response to such perturbations is determined by its order, which is measured by the quantity N and is defined as the ratio of the dispersion length (L_{D}) and the nonlinear length (L_{N}), where T_0 and P_0 are the pulse duration and peak power of the soliton.

$$N = \sqrt{\frac{L_{\mathrm{D}}}{L_{\mathrm{N}}}} = \sqrt{\frac{\gamma T_0^2 P_0}{|\beta_2|}} \tag{2.49}$$

When $N = 1,$ it is called a fundamental soliton, distinguished by its remarkable stability in maintaining both spectral and temporal shape during fiber propagation. If the soliton number falls between 0.5 and 1.5, the input pulse naturally adapts its shape, dissipates excess energy, and transforms into a fundamental soliton. Figure 2.7 shows the evolution of a fundamental soliton with $T_0 = 10$ ps, $\beta_2 = -1$ ps^2/km, $\gamma = 3$ W^{-1}/km. Here, the peak power, P_0 is calculated from:

$$P_0 = \frac{|\beta_2|}{\gamma T_0^2} \approx 3.11 \frac{|\beta_2|}{\gamma T_{\mathrm{FWHM}}^2} \tag{2.50}$$

Here, the full width at half maxima (FWHM) of the soliton is $T_{\mathrm{FWHM}} \approx 1.76 T_0$.

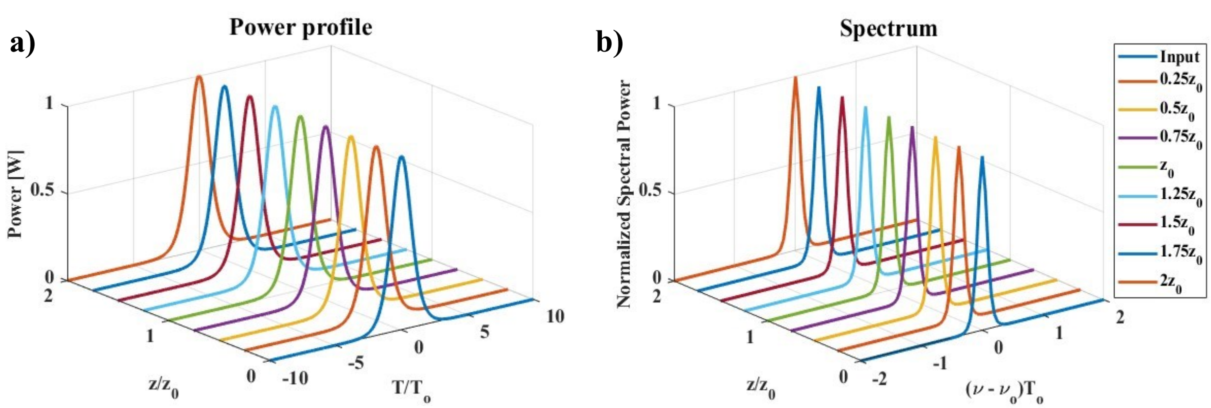

Figure 2.7. Evolution of a fundamental soliton (a) Temporal profile (b) Spectral profile

However, when $N \geq 2$, it is defined as higher-order solitons. Without the presence of higher-order perturbations, the higher-order solitons periodically change their shape. After a certain period, known as the soliton period ($z_0 = \frac{\pi}{2} L_{\mathrm{D}} = \frac{\pi}{2} \frac{T_0^2}{|\beta_2|}$), the soliton recovers its original shape. With $N = 3$

and the previously specified fiber characteristics, Figure 2.8 depicts the evolution of higher-order soliton. It is observed that this pattern is maintained over each section of length z_0.

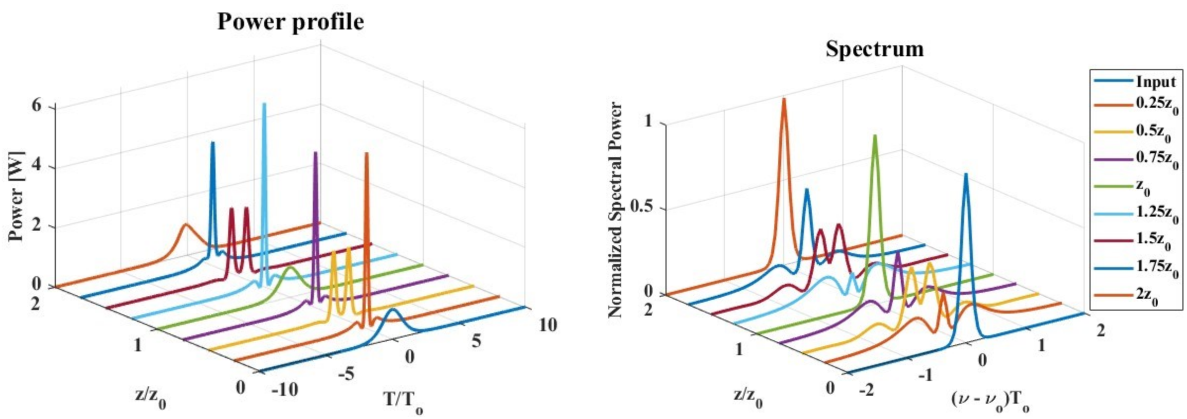

Figure 2.8. Evolution of a higher-order (N=3) soliton (a) Temporal profile (b) Spectral profile

2.6.2 Soliton Fission

In the previous section, only the scenario was discussed where the higher-order perturbation was not present. In this case, a superposition of N fundamental solitons periodically evolve as one entity. However, in practice, the higher-order perturbation is present throughout the fiber, which influences the pulse properties. When $N > 1.5$, an optical pulse propagates as a second- or higher-order soliton. When perturbed by the higher-order dispersion and nonlinear effects, the higher-order soliton deviates from its ideal periodic behavior, resulting in a pulse breakup to a series of fundamental solitons. This process is known as soliton fission. Once the developing soliton reaches its maximum bandwidth, fission starts to occur. The propagation distance that corresponds to that point is referred to as the maximum compression length, L_c. Figure 2.9 shows the evolution of higher-order soliton ($N = 3$) with third-order dispersion (TOD) $\beta_3 = 1\ \text{ps}^3/\text{km}$. Here, the higher-order soliton experiences fission in the presence of TOD and splits into three fundamental solitons, which become more apparent after it propagates $2z_0$ length. The duration and peak power of these fundamental solitons are expressed as[111]:

$$P_{\mathrm{k}} = \frac{(2N+1-2k)^2}{N^2} P_0 \quad ; \quad T_{\mathrm{k}} = \frac{T_0}{2N+1-2k} \tag{2.51}$$

where k varies from 1 to N.

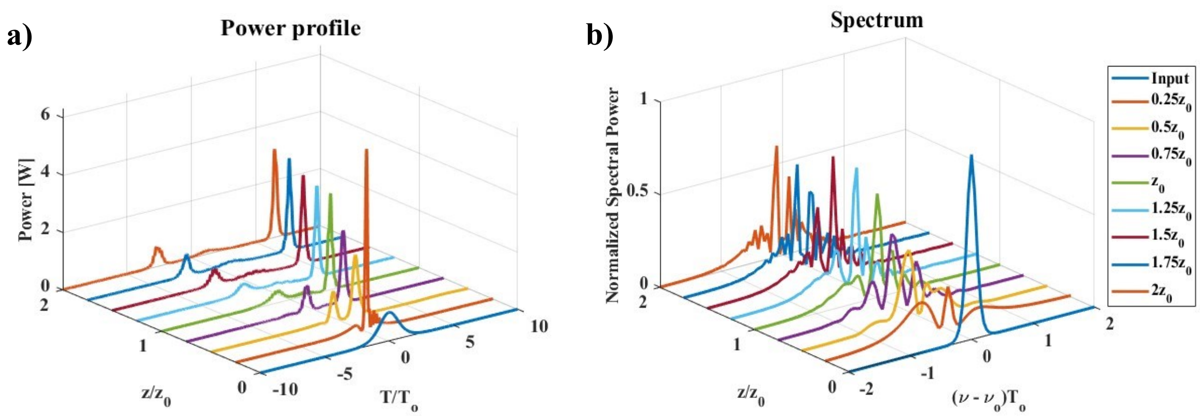

Figure 2.9. Fission of a higher-order soliton with the presence of TOD (a) Temporal profile (b) Spectral profile

2.6.3 Raman-Induced Soliton Self-Frequency Shift

High-order solitons are perturbed by several effects inside optical fibers, including TOD, self-steepening, and intra-pulse Raman scattering. Following fission, the generated fundamental solitons can attain femtosecond durations. For solitons of such small pulse width, the spectral bandwidth is expansive enough for the high-frequency components to amplify the low-frequency components via Raman scattering. In this intra-pulse Raman scattering process, it continuously transfers energy from the blue portion to the red portion of the soliton. Earlier studies demonstrated that under high input energy conditions with intra-pulse Raman scattering effect, the pulses undergo fission, giving rise to N number of fundamental solitons, each subsequently undergoing individual frequency shifts [26–28]. As the higher-order soliton propagates through the nonlinear medium during the fission, it transfers energy to an expanding number of fundamental solitons. This continuous transfer of energy leads to a spectral shift towards longer wavelengths, which is termed SSFS. The first ejected soliton ($k = 1$ in equation 2.51) in the fission process attains the highest peak power and shortest pulse duration, hence experiencing the maximum redshift. The spectral shift can be approximated from Gordon's formula that predicts the SSFS in any fiber [17,111]:

$$\Omega_{\mathrm{G}}(z) = -\frac{8T_{\mathrm{R}}|\beta_2|}{15\,T_0^4}z \tag{2.52}$$

where Ω_{G} is SSFS in $\mathrm{rad/s}$, β_2 is the GVD coefficient, T_{R} is Raman time, T_0 is soliton duration, and z is propagation distance.

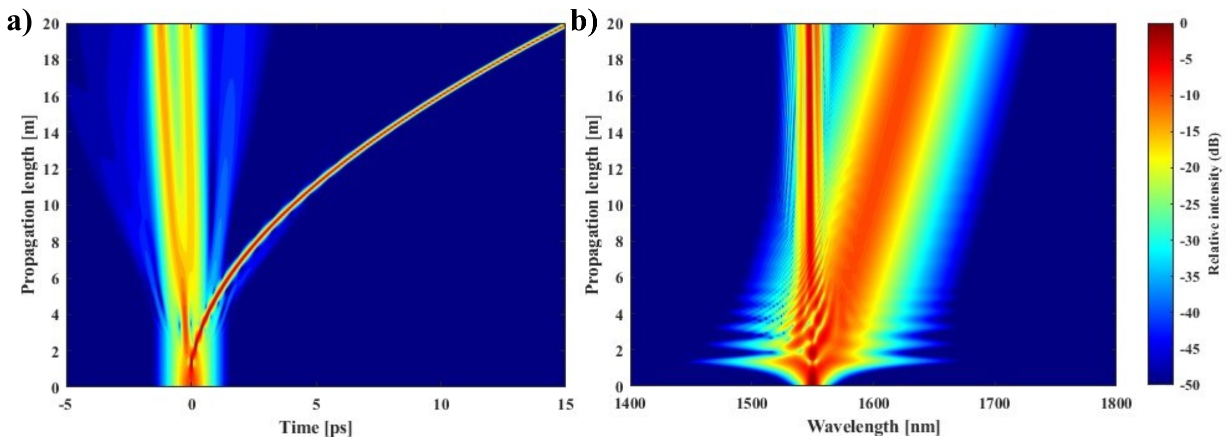

Figure 2.10. Simulated (a) temporal and (b) spectral evolution of a third-order soliton following a Raman-induced fission and SSFS process.

An example of the spectra and temporal evolution of higher-order soliton ($N = 3$) during the SSFS process and soliton fission is depicted in Figure 2.10. The fiber parameters are taken from [18] where the pulse initially has a center wavelength of $\lambda_0 = 1550$ nm, pulse duration of 283 fs, and peak power of 1.7 kW. The medium is a 20 m long lossless SSMF with $\beta_2 = -21.61\ \mathrm{ps^2/km}$, $\gamma = 1.42\ \mathrm{W^{-1}/km}$ at the initial pulse wavelength. The Raman response function for silica is calculated using equation 2.13.

3. Chapter 3: Relation between Higher-order Soliton-Effect Pulse Compression and SSFS

In this chapter, the principle of high-order soliton pulse compression is elucidated, with a comprehensive discussion of its impact on pulse quality, ECE, and SSFS.

3.1 Principle of Higher-order Soliton-Effect Pulse Compression

Depending on whether the pulse goes through anomalous or normal GVD inside the fiber, two different compression techniques are applied. In the case of fibers with normal GVD, it imposes a nearly linear frequency chirp across the pulse. After experiencing the normal GVD regime, the pulse is compressed by passing it through a grating pair. However, in fibers exhibiting anomalous GVD, the same fiber responsible for generating the chirped pulse also compresses it, simplifying the compression mechanism. This compression mechanism is known as soliton-effect compression, an extensively studied technique in the field of ultrafast optics because of its simplicity. This strategy relies on the intricate interplay between SPM and anomalous GVD to compress optical solitons. The fundamental principle involves SPM widening the spectral bandwidth, inducing an up-chirp in the time domain. Concurrently, anomalous GVD compensates for this induced up-chirp, resulting in the compression of the temporal waveform [36]. In the case of a fundamental or first-order solution, the influence of SPM precisely counterbalances the effects of anomalous GVD. As a result, the fundamental soliton maintains its sech^2 shape without distortion as it traverses through a lossless optical fiber. On the other hand, a higher-order soliton undergoes phases of periodic compression and broadening in its temporal and spectral form during propagation. As Figure 2.8 suggests, initially this higher-order soliton narrows its pulse shape before reverting to the original sech^2 profile at integral multiples of the soliton period. It is possible to make the pulse exit the fiber at its narrowest point [20]. Therefore, by amplifying the pulses up to the power level required for forming high-order solitons and by passing them through the correct length of the fiber, highly compressed pulses can be obtained.

The compression factor (F_c) is a measure to express the extent of temporal compression of the output pulse compared to the input pulse. It is defined as the ratio of T_FHWM of the input pulse to that of the compressed pulse [118].

$$F_\text{c} = \frac{T_\text{FHWM} \text{ of input pulse}}{T_\text{FHWM} \text{ of output compressed pulse}} \tag{3.1}$$

The basic structure of a pulse compression setup is shown in Figure 3.1(a), where CF is the compressing fiber, and an amplifier is utilized to enhance the input pulse power at CF in order for a higher-order soliton to form.

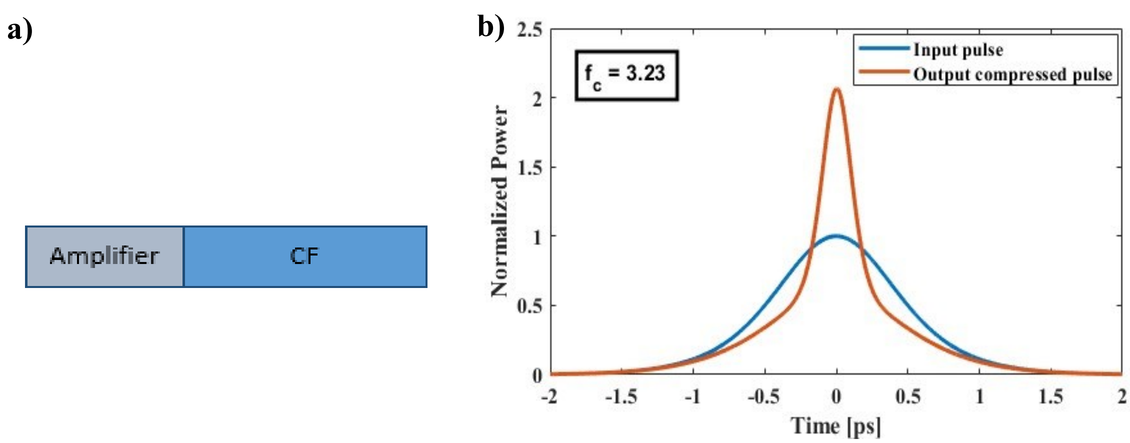

Figure 3.1. (a) Basic setup for pulse compression (b) Temporal profile of input and compressed output pulse

As an example, Figure 3.1(b) shows the temporal profile of input and compressed output pulse after propagating through 1 m long CF. Here, the parameters for this lossless SMF28 fiber are, $\beta_2 = -76\ \text{ps}^2/\text{km}$ and $\gamma = 1.1\ \text{W}^{-1}\text{km}^{-1}$. The input pulse wavelength is 1940 nm, peak power of 2 kW and the FWHM duration of 1 ps. Figure 3.2(a) demonstrates that the pulse compresses more as input power increases from 1 kW to 3.5 kW. At 3.5 kW, the soliton gets maximum compression and beyond that power input, the soliton starts to broaden. According to equation 2.49, the soliton order increases as the pump power increases (shown in Figure 3.2 (b)).

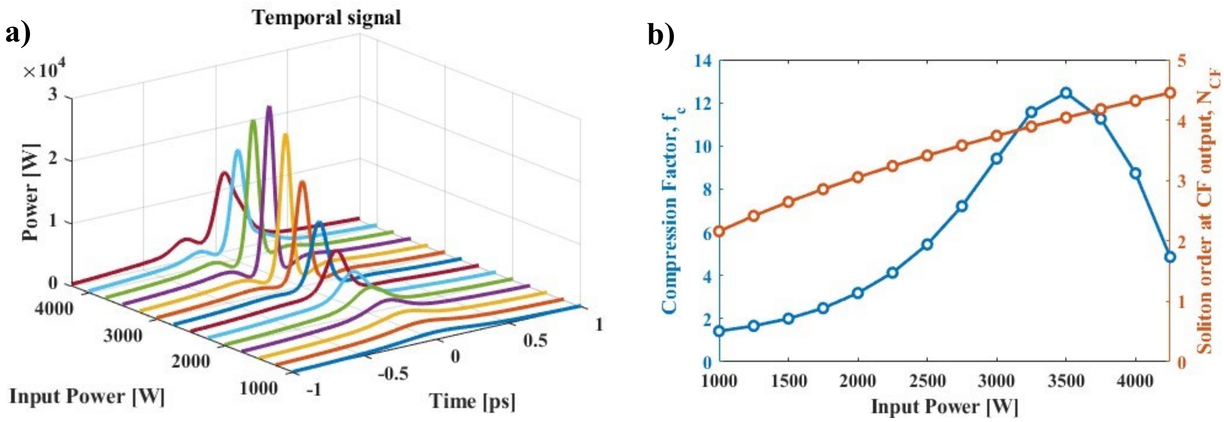

Figure 3.2. (a) Pulse compression with stretched input power (b) Compression factor (f_c) and Soliton order at CF input (N_{CF}) as a function of input power.

The pulse's pre-chirping before injection into the fiber utilized for pulse compression is another crucial component. To address this pre-chirping, the input pulse can be expressed as follows:

$$A(0,T) = \sqrt{P_0}\,\mathrm{sech}(\left(\frac{T}{T_0}\right)\exp\,(-\frac{iCT^2}{2T_0^2})) \tag{3.2}$$

where C is the chirp parameter. In the context of an initially chirped pulse, there are two types of chirp: positive chirp ($C > 0$) and negative chirp ($C < 0$). As the pulse propagates through an optical fiber with β_2, the value of its chirp parameter will evolve gradually along propagation distance z. More specifically, red components travel faster than blue components in the normal-GVD region ($\beta_2 > 0$), while the opposite occurs in the anomalous-GVD region ($\beta_2 < 0$). It is known that if $\beta_2 C > 0$, pulse broadening happens. The reason is related to the fact that the dispersion-induced chirp adds to the input chirp because the two contributions have the same sign.

When $\beta_2 C < 0$, the pulse leads to compression (during the initial stages of the evolution) as the dispersion-induced chirp is opposite to that of the input chirp [33]. Note that the nonlinearity of the fiber adds a positive chip (up-chirp) to the pulse, which helps the pulse to compress as well. This compression happens only during the initial stages of the evolution and once the peak is reached, the pulse starts to broaden again, and fission happens.

The soliton inherently possesses zero chirp, a characteristic arising from the cancellation of chirp through the interplay of nonlinear and dispersive effects. When an external chirp is introduced, the soliton actively attempts to eliminate it. This process involves the SPM broadening the pulse spectrum, ultimately aiding in pulse compression. Consequently, this phenomenon is crucial for effective soliton compression.

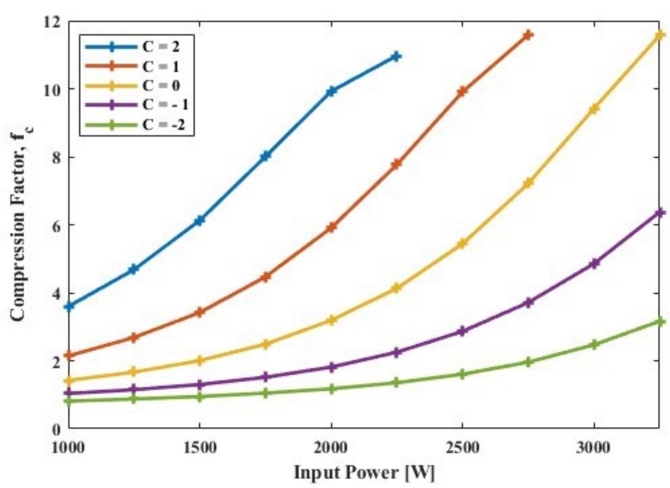

Figure 3.3. Effect of various chirp values on soliton-effect pulse compression

Using the aforementioned fiber characteristics, Figure 3.3 shows that the additional chirp significantly contributes to the overall compression of the soliton. For a positive chirp, achieving the same compression point as the chirp-free case requires less power. As $\beta_2 < 0$, it is an anomalous medium. As the soliton with positive chirp propagates through the fiber and experiences anomalous dispersion, the velocity of the high-frequency components becomes higher than the velocity of the low-frequency component. This results in temporal compression. Conversely, in the case of negative chirp, the opposite effect occurs.

Another crucial term is the quality factor (Q_c), which is numerically evaluated from the following equation [119]:

$$Q_{\mathrm{c}}(\%) = 1 - \frac{E_{\mathrm{pedestal}}}{100} \tag{3.3}$$

which quantifies the fraction of the energy contained in the main lobe of the compressed pulse. When a pulse is compressed or shifted, its pedestal contains a portion of the overall input energy, which is expressed as E_{pedestal}, or pedestal energy. In definition, it is [120]:

$$E_{\mathrm{pedestal}}(\%) = \frac{|E_{\mathrm{total}} - E_{\mathrm{sech}}|}{E_{\mathrm{total}}} \times 100 \tag{3.4}$$

where E_{total} is the total energy in the output pulse. E_{sech} is determined by the proportion of energy contained in the sech-fitted portion of the pulse as shown in Figure 3.4.

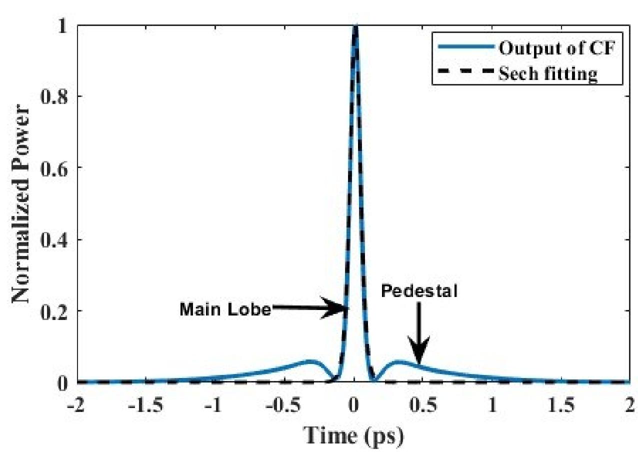

Figure 3.4. The output of the CF and sech-fitted curve using the same peak amplitude and pulse width of the compressed pulse.

Two methods can be used to achieve this. The first one involves taking the CF's output pulse and extracting the pulse width (FWHM) and peak power. Then the peak power and pulse width (FWHM) are inserted in a sech^2 pulse and the energy E_{sech} in the main lobe is calculated with the following equation [120]:

$$E_{\text{sech}} = \frac{2P_{\text{peak}}T_{\text{FWHM}}}{1.7627} \tag{3.5}$$

In the second process, a sech^2 curve fitting is applied to the central narrow spike within the compressed pulse. The quality factor is subsequently determined as the ratio of the area beneath the curve-fitted spike to the overall area of the compressed pulse. This corresponds to the ratio of the energy within the spike, denoted as E_{sech}, to the overall pulse energy, denoted as E_{total}. The use of a sech^2 curve for fitting the spike is based on soliton theory, where a Nth-order soliton is considered a collective state of N fundamental solitons. In this context, the central spike represents a fundamental soliton resulting from the interaction of *N*-bound solitons during fiber propagation, hence exhibiting a naturally occurring sech^2 pulse shape. Figure 3.5 shows that this process demonstrated an exact fit of the sech^2 shape, except at the spike's edges where it connects to the broader pedestal.

In addition, it shows that as the input energy is increased; the pedestal become more prominent. Similarly, these studies [20,121] demonstrated that as the soliton order increases at the fiber input, a higher pedestal formation is observed. The reason behind this is, that as the pump power increases, it gives rise to the soliton order. Hence, a higher amount of energy goes toward the pedestal, which causes the degradation of the quality of the compressed pulse.

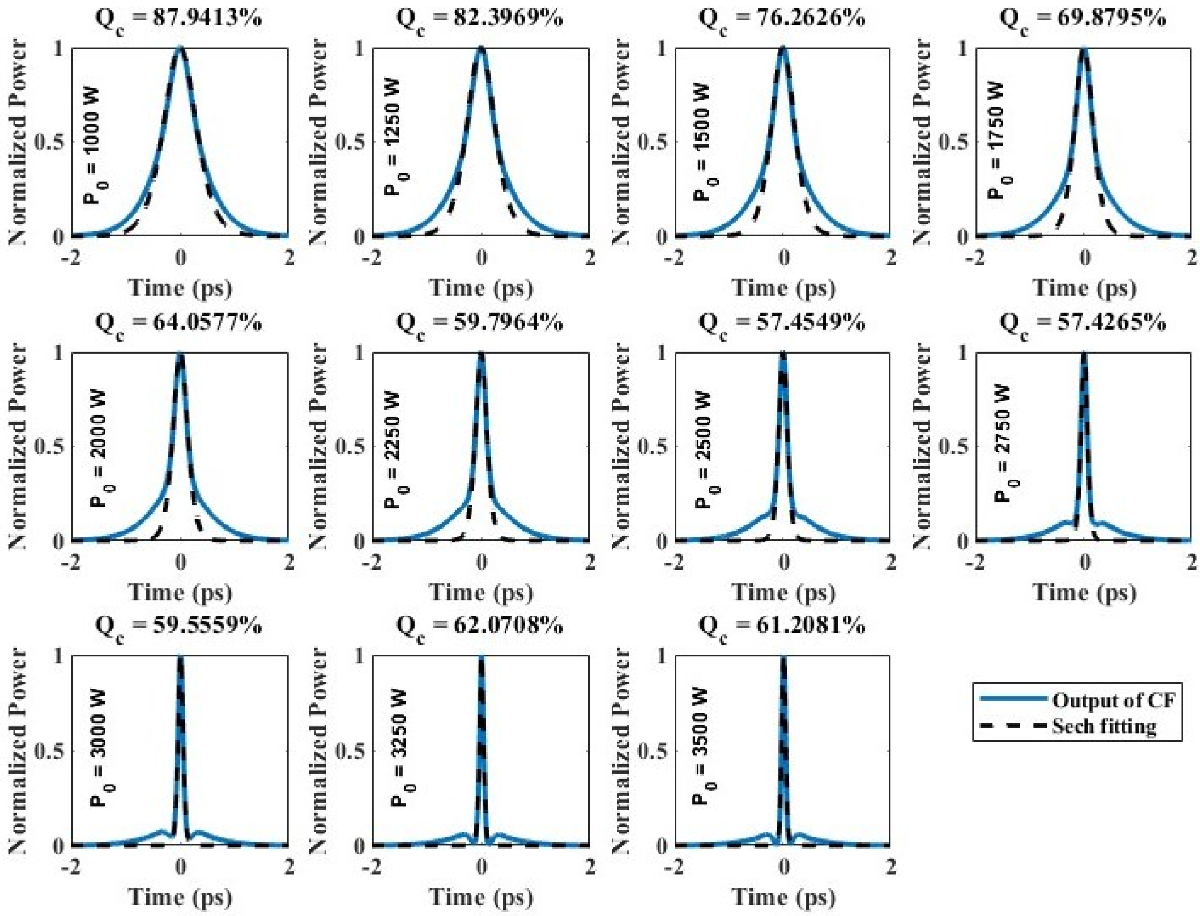

Figure 3.5. Compressed pulse with sech-fitting

The following Figure 3.6 shows the spectrum of the compressed pulses, and the evolution of the pedestal is prominent with the increase of power input. Figure 3.7 agrees with the calculations of [20,121], and it illustrates how the dynamics of the higher-order soliton compression in fibers are the only cause of the intrinsic decrease of the compressed pulse quality as a function of soliton order at the fiber input (N).

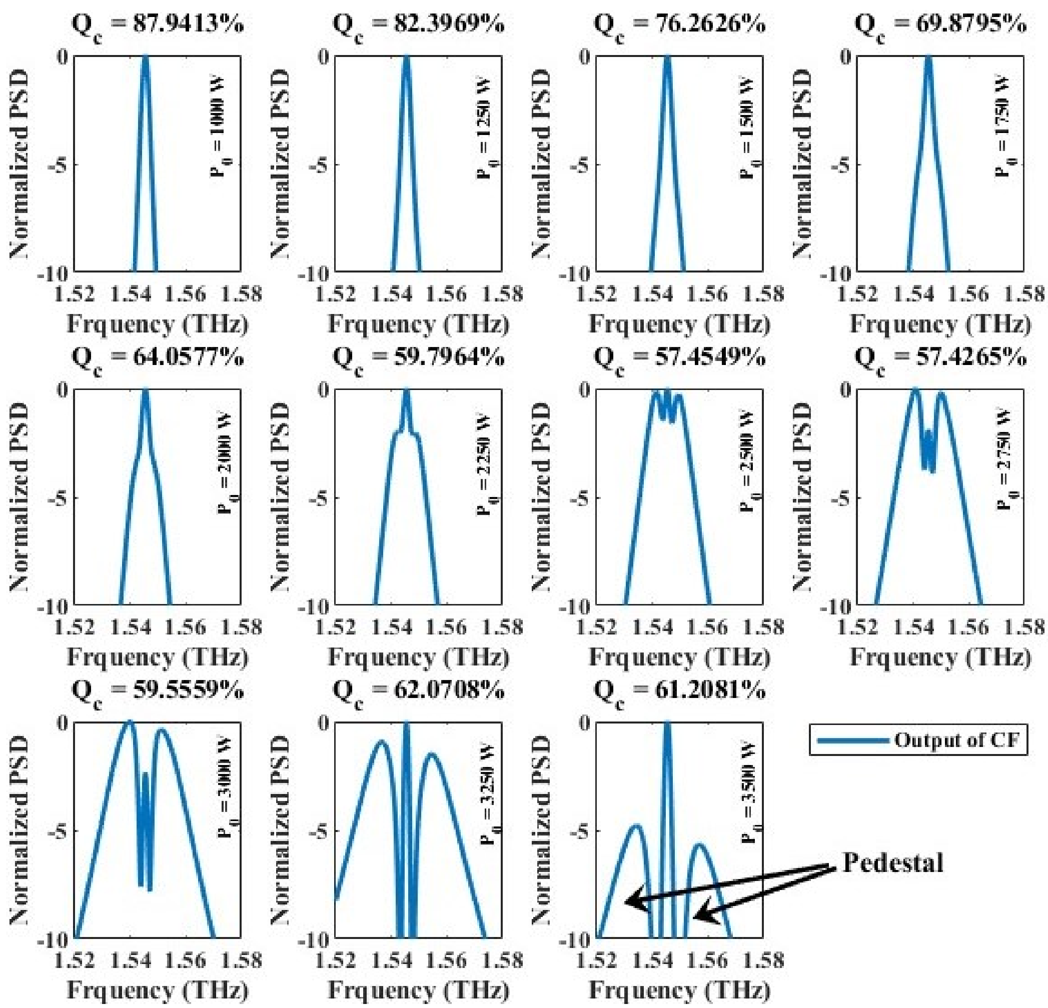

Figure 3.6. The spectrum of the compressed pulse

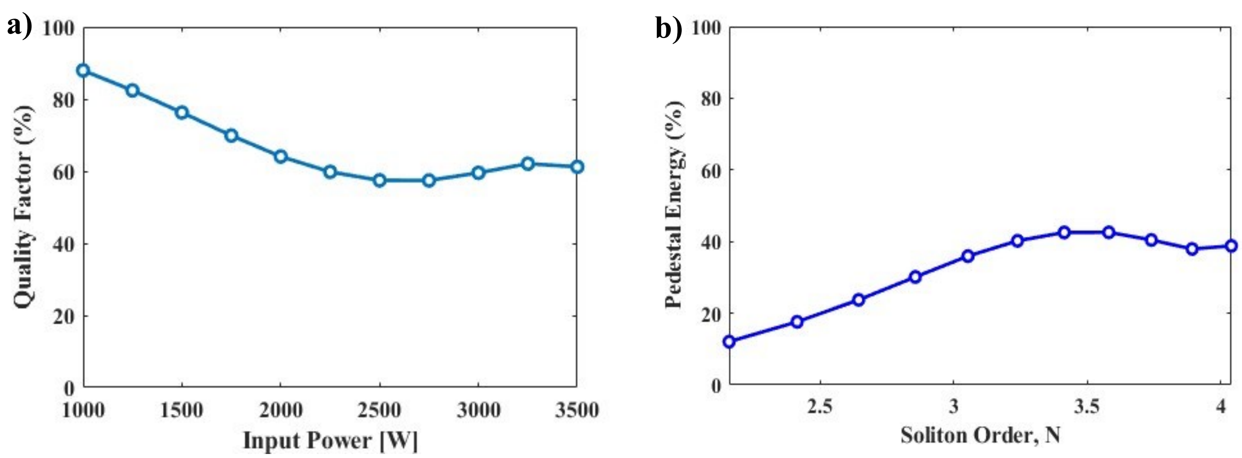

Figure 3.7. (a) Pulse quality factor of compressed pulse as a function of pump power (b) Pedestal energy as a function of soliton order

In a recent study [31], Shamim *et al*. proposed a mechanism in the context of SSFS to maintain the soliton order at the fiber's input. This technique involves the insertion of a CF before the NLF, aiming to retain the soliton number at the NLF's input, which further enables high SSFS maintaining improved ECE. In this technique, the pulse undergoes compression within the CF, and the resulting compressed pulse is directly transmitted through the NLF to simultaneously enhance the ECE and SSFS.

3.2 Effect of CF on Soliton Order, SSFS, and ECE

Figure 3.8 is the schematic for an SSFS pumping mechanism [31]. It comprises an amplifier that is used to provide the energy of the pump soliton, followed by a CF where pulse pre-compression occurs and an NLF where SSFS takes place. The CF is an anomalous dispersion fiber and experiences input soliton order, $N_{\mathrm{CF}} > 1$ so that the pulse undergoes compression due to the higher-order soliton effect as it propagates in the fiber. Here, CF is a single-mode silica fiber, and the properties have been specified in the previous section. The NLF fiber is classified as a high numerical aperture (HNA) fiber due to its high numerical aperture (see equation 2.1). This indicates that the nonlinearity will be strong due to the small core diameter (see equation 2.32). The impact of the CF fiber on soliton order, SSFS, and ECE at the NLF will be covered in the section that follows.

Figure 3.8. Schematic of an SSFS based on soliton order preservation pumping mechanism. CF: compressing fiber; NLF: nonlinear fiber.

3.2.1 *Comparison of Soliton order (in NLF input) with and without CF:*

Passing from 1 m long CF to NLF of 5 m, the soliton order at the input of NLF (N_{NLF}) will be different from the soliton order at the input of the CF (N_{CF}) because of the unequal fiber parameters. Figure 3.9(a) shows the N_{NLF} as a function of the input power, where the N_{NLF} can be written as,

$$N = \sqrt{\frac{\Gamma\gamma_{\mathrm{NLF}} T_0^2 P_0}{|\beta_{2,\mathrm{NLF}}|}} \tag{3.8}$$

where Γ is the transmittance from CF to NLF. Here, NLF is a high numerical aperture silica fiber with a NA= 0.23, a dispersion, of $\beta_2 = -71$ ps^2/km, and a nonlinearity, of γ = 2.6 W^{-1}km^{-1}. The output values for duration and peak power, as depicted in Figure 3.9(b), are used to provide an approximation of the N_{NLF}, which predicts the accurate number of fundamental solitons that may appear after soliton fission.

Figure 3.9(a) shows that the soliton order increases from 4 to about 6 at the NLF input (without CF). On the other hand, the soliton order gradually increases (2 to about 4) at the CF input. When CF is employed before NLF, the soliton order at the NLF input falls from 3 and remains constant (for the values considered in this simulation) at the NLF input even when the pump power is increased.

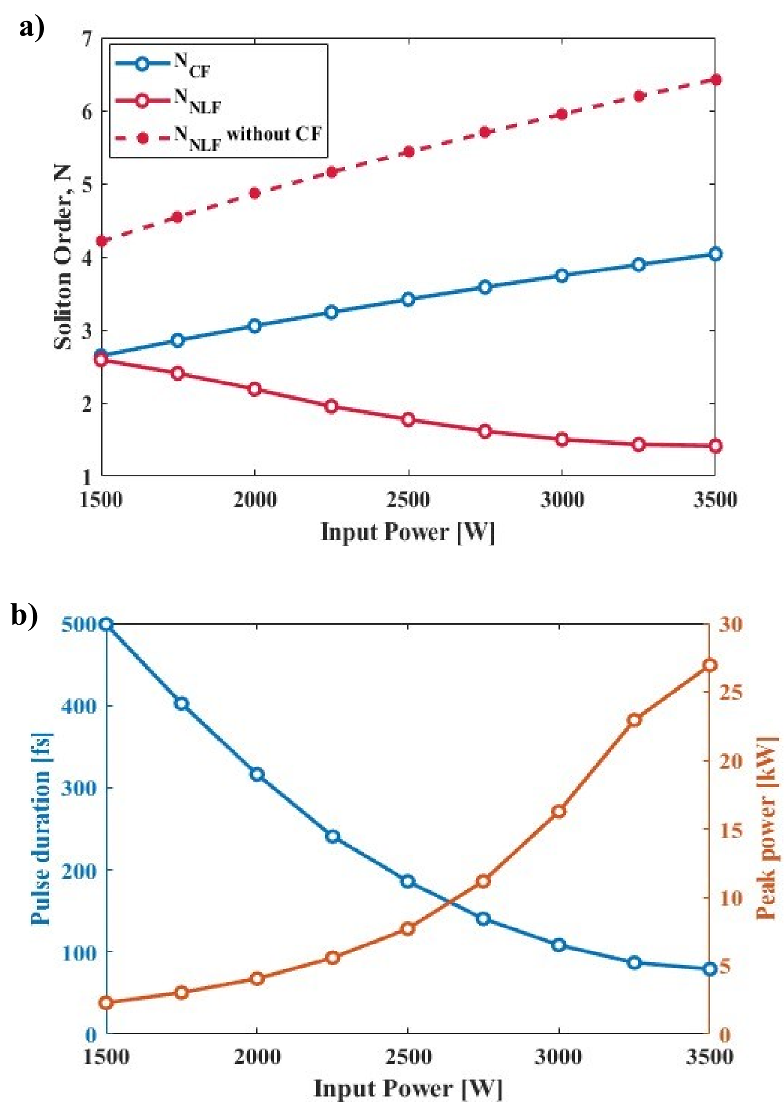

Figure 3.9. (a) N_{CF} and N_{NLF} (with or without CF) as a function of pump power (b) Duration and peak power of the resultant pulse at the CF output as a function of input power

3.2.2 Comparison of SSFS (in NLF) with and without CF:

If the pulse duration at the fiber's input is shorter, the wavelength shift from the SSFS will be larger since it rises proportionately with the fourth power of inverse pulse duration [11,15]. Consequently, fiber-based pulse compression of the input pulse is crucial to achieve high SSFS.

In Figure 3.10 (a) and (b) the comparison has been shown with and without the use of CF, respectively.

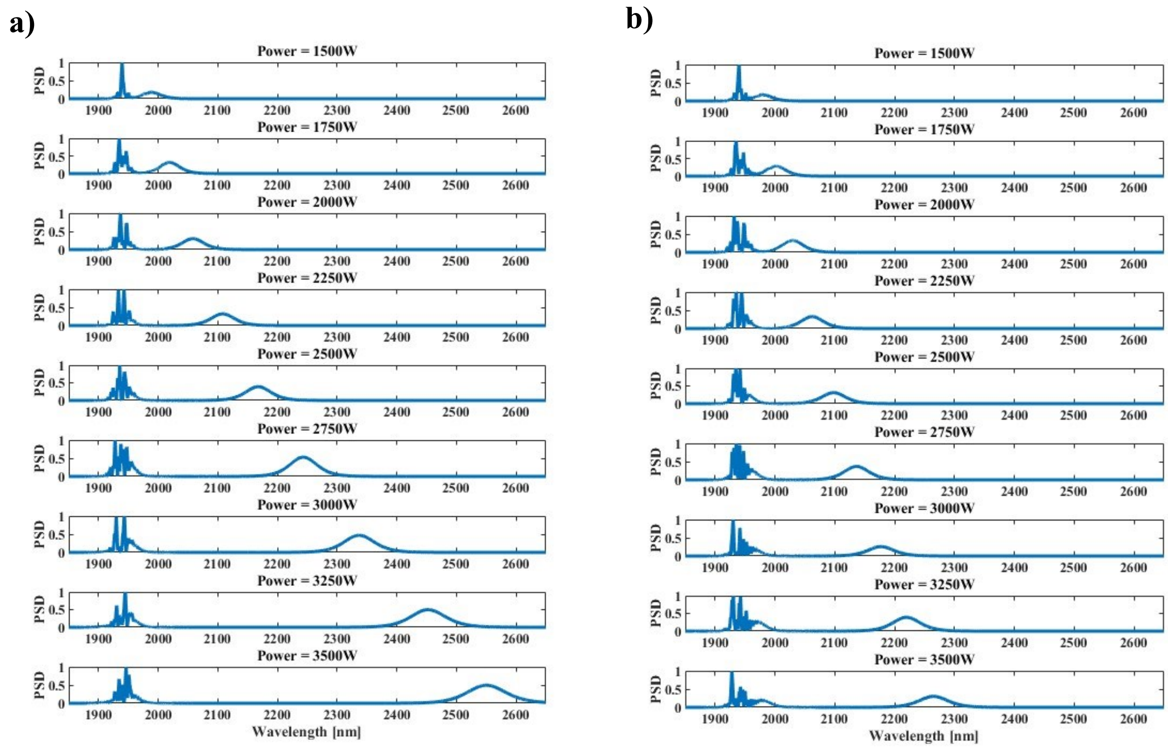

Figure 3.10. (a) SSFS through NLF with prior use of CF (b) SSFS through NLF without CF

It is obvious from Figure 3.10 that the use of only a CF is assisting in achieving more SSFS. The following Figure 3.11 shows the comparison of wavelength shifts as a function of pump power. The SSFS with CF is in the range of 50 nm to 611 nm. However, the SSFS (without CF) case is in the range of 39 nm to 326 nm. According to equation 2.52, with the increase of input power, this linear increase in SSFS remains valid only for the early stages of the soliton evolution in both experimental and numerical evolution. However, in practice, the saturation in the spectral shift occurs due to the continuous chirping and subsequent temporal broadening of the soliton, resulting from the effect of TOD. The intrinsic fiber losses are one of the main limiting factors when the pulse with wavelength > 2.2 μm propagates in a silica fiber.

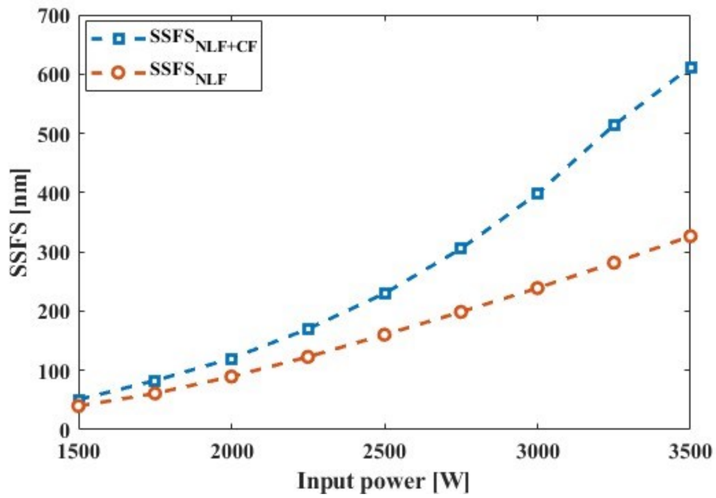

Figure 3.11. Comparison of SSFS through NLF with and without CF

3.2.3 Comparison of ECE (in NLF) with or without CF:

Increasing the energy input into the system is a method to improve SSFS in addition to the initial compression of the input pulse. Hence, fiber-based pulse compression stands as a crucial technique for attaining both high SSFS as well as ECE. The following filter equation has been used to estimate the ECE [8].

The global transmission function of this filtering system,

$$T = \exp\left(-\left(\frac{\lambda - \Lambda_0}{\Delta\lambda}\right)^m\right) \tag{3.9}$$

Here $\Delta\lambda$ is the bandwidth of the filter, λ is the input wavelength. Λ_0 and m are the wavelength at peak transmission and the order of super-Gaussian pulse, respectively. The following values were used in Figure 3.12: $\Delta\lambda$ =600 nm, λ = 1940 nm, Λ_0 = 2400 nm, and m = 100.

As shown in Figure 3.12, the soliton energy is estimated from the filtered data (under the curve area method). The total energy of the NLF output is also calculated in the same manner. The fraction of total energy imparted to the soliton is the ECE and the equation is as follows:

$$\mathrm{ECE}(\%) = \frac{\text{Energy of soliton}}{\text{Input energy}} \times 100\% \tag{3.10}$$

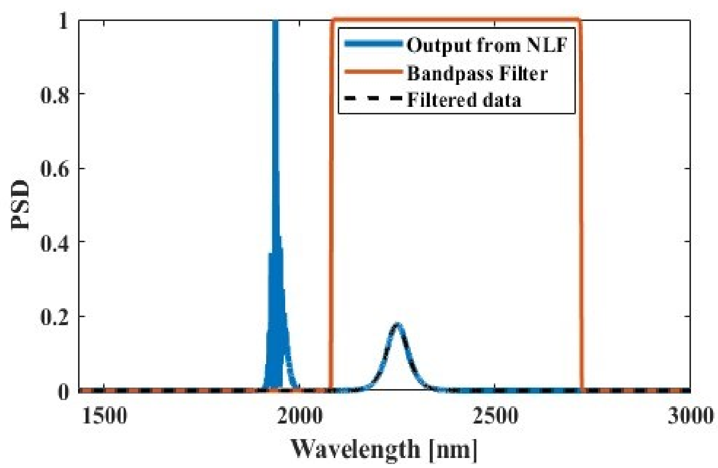

Figure 3.12. Filter for estimating ECE

The ECE comparison is displayed in Figure 3.13, where the ECE is calculated using equation 3.10 described earlier. The maximum ECE without CF is approximately 53.4%, but ECE when CF is utilized ranges from 56.4% to 74.5%. The usage of CF prior to NLF raises ECE in this instance, and the most compressed pulse achieves the maximum ECE of 75%. This is explained by the fact that, according to equation 2.51, the widths and peak powers of each fundamental soliton are connected to the width T_0 and peak power P_0 of input pulses. The energy of a soliton for $k = 1$ is equal to $2T_1P_1$. CF is used to increase the peak power of the input pulse at the NLF while simultaneously lowering the soliton order at the NLF input. As a result, after fission, the soliton has a high peak power P_1, which results in higher ECE.

However, if CF is not used prior to NLF, the order of soliton at the NLF input increases, which results in decreased ECE as shown in Figure 3.13. From this result, it is apparent that the insertion of the CF ensures that N_{NLF} is preserved, which further enhances the SSFS and ECE in the NLF.

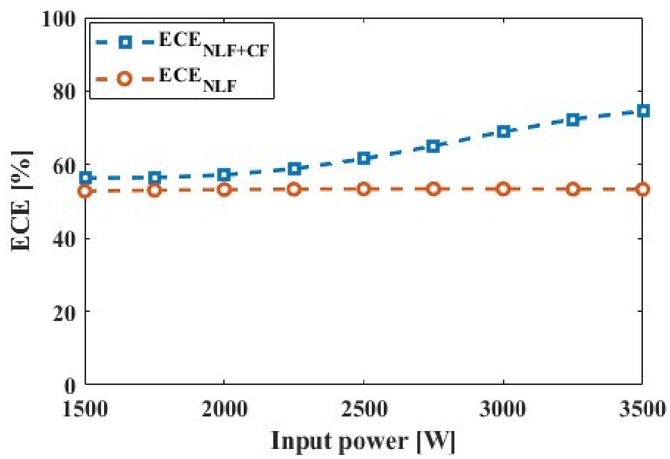

Figure 3.13. Comparison of ECE at NLF with or without CF

3.3 Experimental Findings

This section presents an elaborate discussion of the experimental setup and characteristics of the fiber used in the setup. Subsequently, the experimental results are presented and validated with numerical evolution.

3.3.1 Experimental Setup

Figure 3.14 depicts the schematic diagram of the experimental setup for our proposed SSFS system. A passively mode-locked thulium-doped fiber laser (TDFL, AdValue Photonics, model AP-ML) with nonlinear polarization rotation serves as the seeding oscillator. At a wavelength of 1940 nm, it creates pulses with a duration of 900 fs and a repetition rate of 30 MHz. Following the TDFL, the pulse enters the amplification stage, which consists of two erbium-doped fiber amplifiers (EDFAs) as pumps, two wavelength division multiplexers (WDMs) as combiners, and 32 cm long thulium-doped fiber (TDF, Coractive DCF-TM-6/125). In this setup, pulse amplification is achieved using a Thulium-Doped Fiber Amplifier (TDFA), which operates within the TDF. The TDFA is driven by a substantial power source of up to 1.7 W, delivered in the C band of the optical spectrum. This power is fed into the TDF from two EDFAs, strategically arranged to propagate both in the co-propagating direction and counter to it. The use of two WDMs in the setup ensures efficient coordination of optical signals during the amplification process. As a next step, the SMF-28 operates as a CF. The dispersive and nonlinear characteristics of the SMF-28 fiber are specified in section 3.3.2.1. The length of CF is varied from 0.6 m to 1.4 m in order to investigate the effect of CF on the enhancement of SSFS. Then the pulse propagates through the Raman shifting stage, consisting of 1.7 m long silica-based HNA fiber (NLF, Coractive SCF-UN). The input end of the HNA fiber is fusion spliced with the output of the CF. Section 3.3.2.2 contains details on the HNA fiber's dispersive and nonlinear properties.

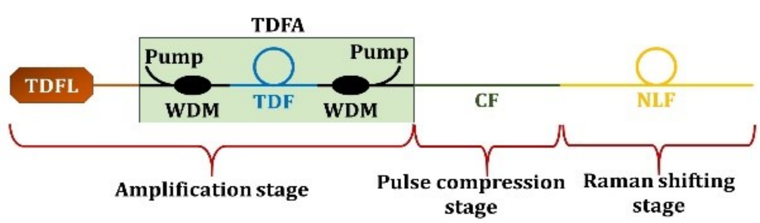

Figure 3.14. Experimental setup for SSFS system. TDFL: thulium-doped fiber laser; WDM: wavelength division multiplexer; TDF: thulium-doped fiber; TDFA: thulium-doped fiber amplifier; CF: compressing fiber; NLF: nonlinear fiber

The output of the NLF is examined using several measurement instruments, including a power meter (Newport 843-R), an intensity auto-correlator (Femtochrome research FR-103XL), and an optical spectrum analyzer (OSA, Yokogawa AQ6375B). A high-speed digital oscilloscope with 2.5

GHz bandwidth (Agilent, DSO-X92504A) was used to measure time characteristics. These devices allow for the characterization and analysis of the optical signals at the output of CF and NLF.

3.3.2 Fiber Characteristics

In this section, the fiber characteristics such as length, core diameter, dispersion, and nonlinearity of CF (SMF-28) and NLF (HNA) have been specified.

3.3.2.1 Compressing Fiber: SMF-28

The CF consists of a variable length of 0.6 m to 1.4 m of standard SMF-28 step-index silica fiber. The fiber parameters are taken from [31] and presented in table 3.1:

Table 3.1. Parameters for the SMF-28 fiber

Parameter	L (m)	γ_0 ($\mathrm{W^{-1}km^{-1}}$)	f_R	τ_1 (fs)	τ_2 (fs)
Value	$0.6-1.4$	0.8	0.18	12.2	32

As the spectrum of the compressed pulses does not shift in wavelength, the wavelength dependence of A_eff and n_2 is negligible. The SMF-28 operates with a core/cladding diameter of $8.2/125\ \mu$m, dispersion of $\beta_2 = -76\ \mathrm{ps^2/km}$ at the pump wavelength of 1940 nm [122,123]. For numerical analysis, the best match was determined to be a constant loss of 0.2 dB/km. The dispersion up to the 10th order is considered and modeled using a Taylor series expansion. The resulting dispersion curve is illustrated in the following Figure 3.15.

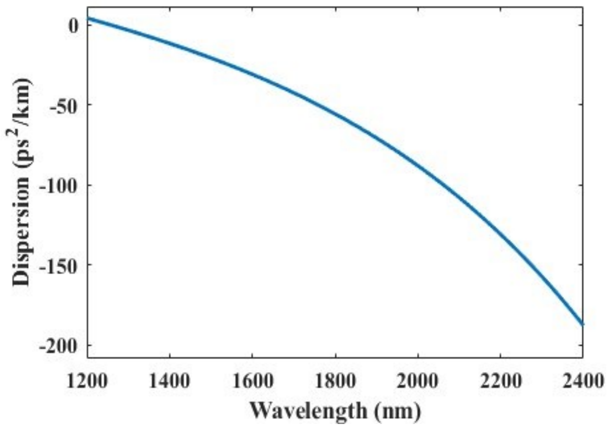

Figure 3.15. Group velocity dispersion for SMF-28 fiber.

3.3.2.2 Nonlinear Fiber: HNA

The NLF is a 1.7 m long silica-based HNA fiber (NLF, Coractive SCF-UN). The NA of a fiber is a dimensionless parameter that characterizes the light-gathering ability and light-carrying capacity of an optical fiber. The NA is primarily controlled by the refractive indices of the core and cladding materials and the geometry of the fiber. By adjusting core diameter, and designing the cladding appropriately, the NA of an optical fiber can be made high to meet specific performance requirements. This HNA fiber is customized to a small core and large NA to provide good confinement of the guided mode in the fiber core region. It has an NA of 0.23 and core/cladding diameters of 6/125 μm.

The wavelength dependence of A_{eff} and n_2 is negligible over the spectrum bandwidth used in this thesis. At the pump wavelength (1940 nm), the NLF exhibits a GVD of $-74\ \text{ps}^2/\text{km}$, an effective mode area of 36 μm^2 [31]. In Figure 3.16 (a), it is shown that the loss in silica becomes significant for wavelengths greater than 2200 nm. Since the pulse spectrum used in this thesis remains below this threshold, the impact of loss is minimal. Hence, for the purposes of numerical analysis, a constant loss of 0.2 dB/km has been assumed. These parameters characterize the NLF's optical properties and its response to optical signals at the specified wavelength. The input end of the HNA fiber is fusion spliced with the output of the CF, resulting in an insertion loss of 0.96 dB, with a transmittance of Γ = 81.5%.

The fiber parameters of HNA are taken from [31] and presented in Table 3.2:

Table 3.2. Parameters for the HNA fiber

Parameter	L (m)	γ_0 ($\mathrm{W^{-1}km^{-1}}$)	f_R	τ_1 (fs)	τ_2 (fs)
Value	1.7	2.5	0.18	12.2	32

The dispersion up to the 10th order is considered. Figure 3.16 indicates the wavelength-dependent GVD of the NLF from solving the characteristic equation of the fundamental mode in an optical fiber.

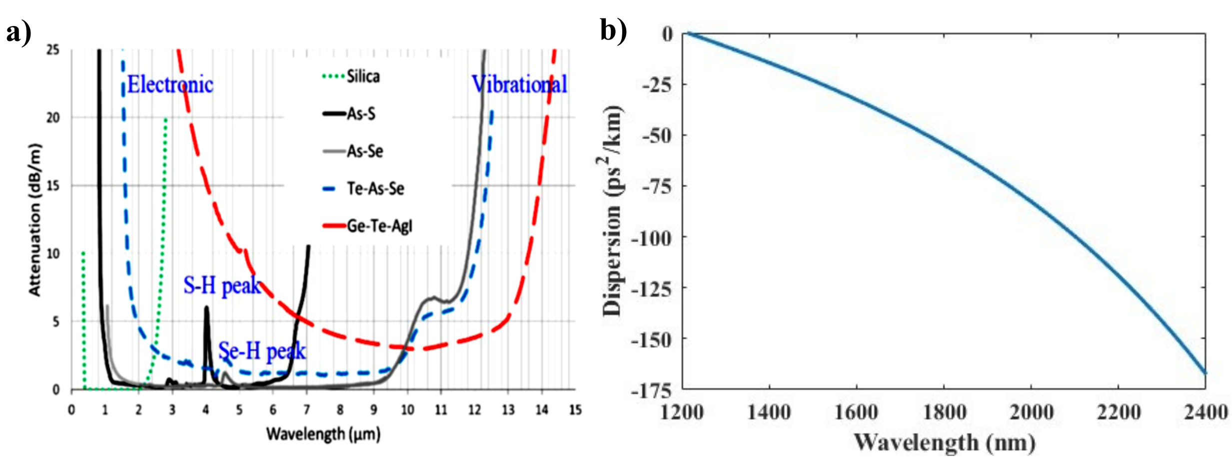

Figure 3.16. (a) MIR transmission spectrum of ChG optical fibers in comparison to silica. (from [124]*) (b) Group velocity dispersion for HNA fiber.*

3.3.3 Result and Discussion

For the experiment, variable CF lengths of 0.6 m to 1.4 m are taken into consideration. The experimentally measured peak power and FWHM duration at the CF output are presented in Figure 3.17(a). The soliton experiences temporal compression of up to 108 fs at the maximum compression point (CF length of 1 m), resulting in an increased peak power. The length required to attain its maximum compression point, the CF length of 1 m, is referred to as the maximum compression length (L_{c}). The pulse broadens and initiates the fission process beyond the L_{c}. The soliton order at the CF input (N_{CF}) remains 3 in all circumstances, provided that the input peak power, dispersive properties, and nonlinear features of the fiber remain constant. For the CF lengths from 0.6 m ~ 1 m depicted in Figure 3.17(b), the soliton order at NLF input, N_{NLF} (using equation 3.8), remains within 2. The N_{NLF} spikes again with a CF length increase that exceeds this threshold (L_{c}).

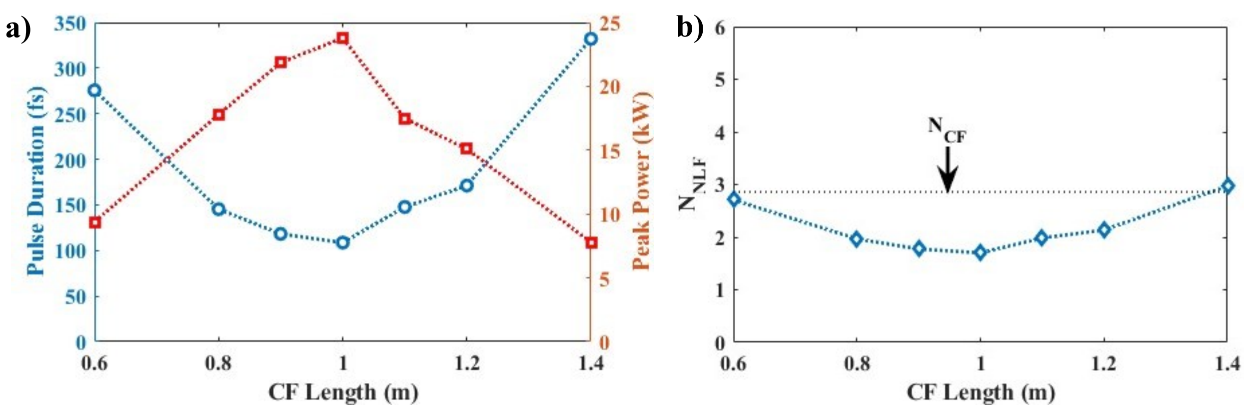

Figure 3.17. (a) Measured soliton duration and peak power at the CF output (b) Measured N_{NLF} as a function of variable CF length.

Figure 3.18 illustrates the experimental spectrum evolution at the NLF output, where the self-shifting fundamental soliton is observed at long wavelengths, and its residual power is at the pump wavelength. With the length of the CF increasing from 0.6 m to 1 m, the soliton experiences heightened SSFS. As the input pulse energy and NLF parameters were kept constant in both situations, it was demonstrated that solely by utilizing the variable length of CF prior to NLF, the SSFS was enhanced. The result can be explained by Gordon's formula that predicts the SSFS in any fiber [17,111]. According to equation (2.52), the SSFS in a fiber grows proportionally with inverse pulse duration to the fourth order, therefore reducing the pulse width even a little resulting in a substantial spectral shift of the soliton. When the input soliton is propagated through the CF, it experiences a reduction in soliton duration (FWHM), this compression of soliton duration serves as the primary factor for the observed enhancement of SSFS when CF is introduced before the NLF.

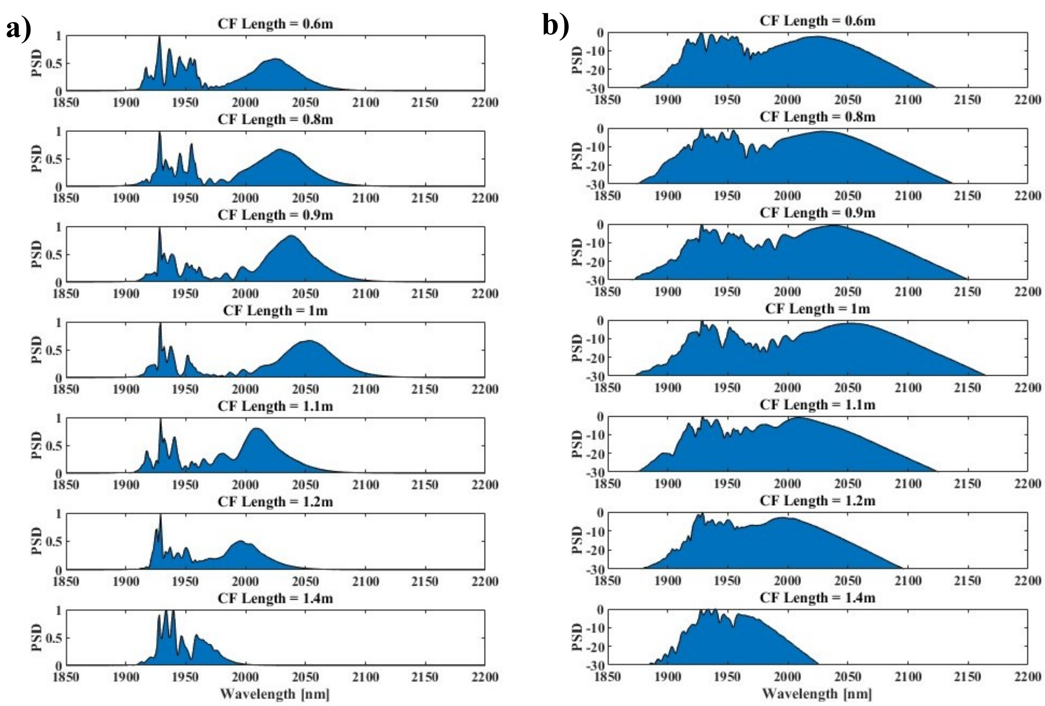

Figure 3.18. Experimental spectrum evolution at the output of the NLF as a function of variable CF length (a) linear (b) dB scale

Figure 3.19 displays the soliton's central wavelength shift with respect to the varied CF length. It further establishes that when the maximum compressed pulse from the CF is passed through the NLF, the soliton shifts the most after fission. Lower SSFS results from soliton fission occurring inside the CF when the length of CF is extended beyond the L_c.

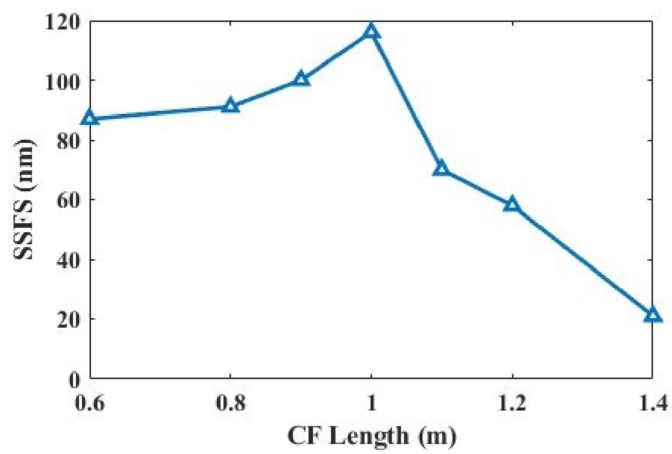

Figure 3.19. Experimental central wavelength shift as a function of variable CF length

3.4 Numerical Validation

Figure 3.20 shows the resultant pulse with the pedestal component at the output of CF. The simulation is performed by numerically solving the GNLSE of equation 2.41 using the adaptive step-size split-step Fourier method (SSFM).

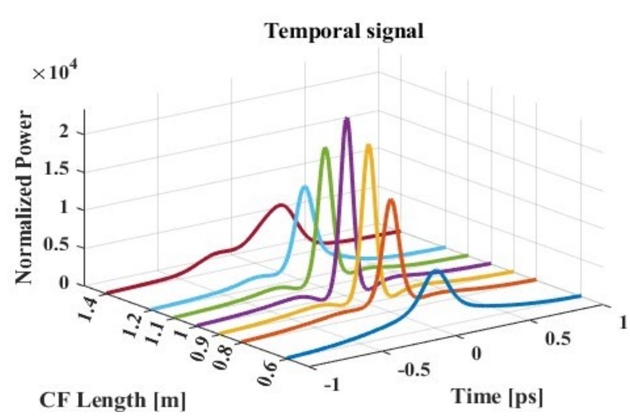

Figure 3.20. Numerical temporal evolution at the output of CF

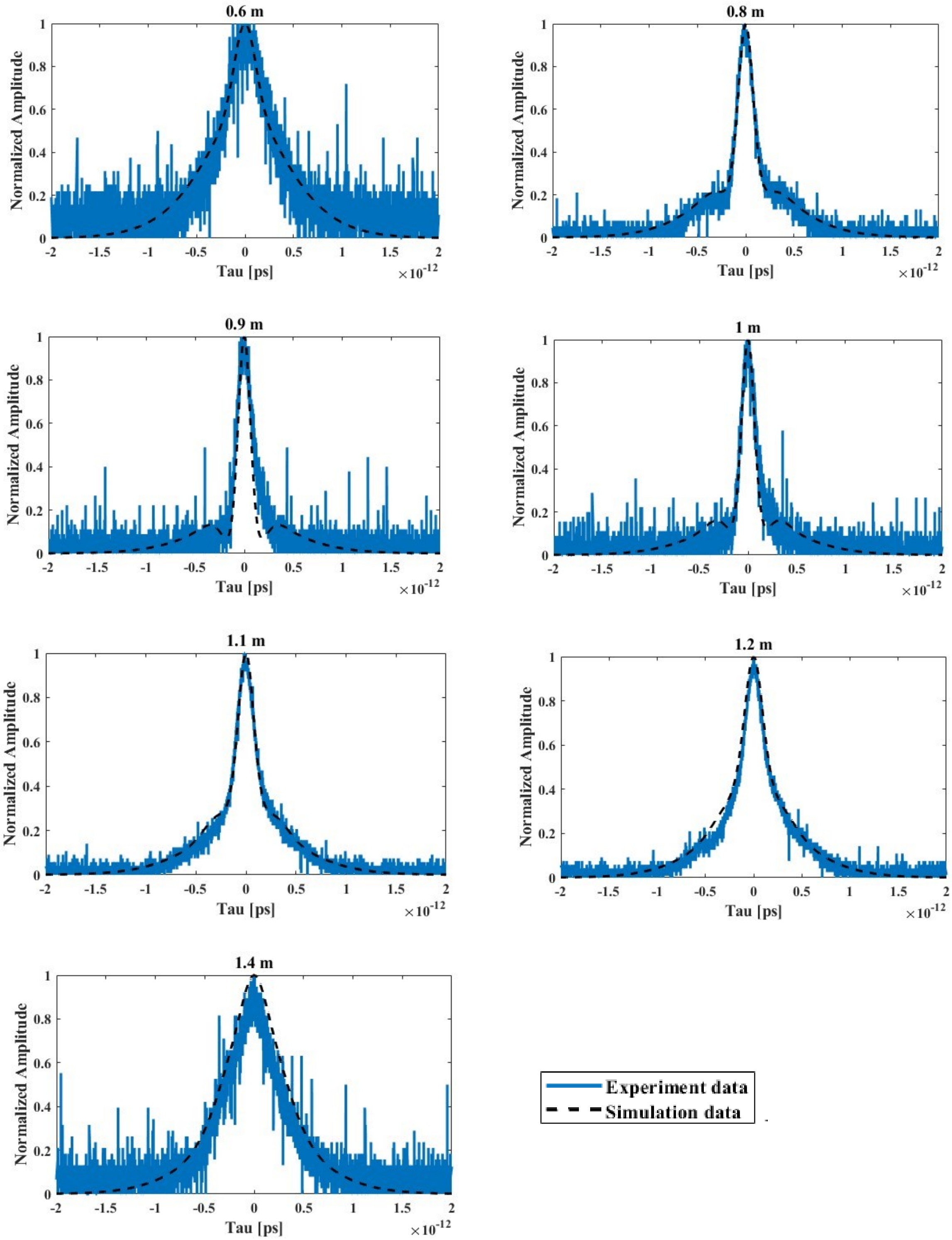

Figure 3.21. The auto-correlated simulated result with the experimental raw data from auto-correlator

The simulated auto-correlation trace is plotted in Figure 3.21 alongside the experimental result that the auto-correlator produced. This demonstrates how well the auto-correlated simulated result from CF fits the actual experimental data. Figure 3.22(a) presents the duration and peak power of the compressed pulse measured at the CF output. The soliton is compressed 7.55-fold from 750 fs to 98 fs for an increase of CF length from 0.6 m to 1 m. At 1 m of CF length, it reaches its maximum compression point, hence this length is the L_c. As the input peak power, dispersive, and nonlinear characteristics of fiber are kept in the same soliton order in the input of CF (N_{CF}) stays 3 for all cases. Figure 3.22(b) shows the N_{NLF} as a function of CF length. The recorded values align well with the experimental values depicted in Figure 3.17.

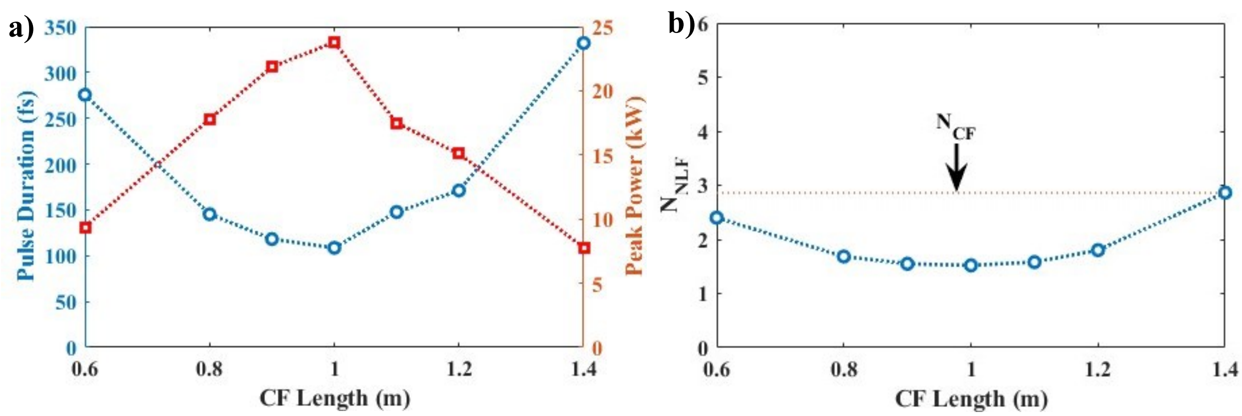

Figure 3.22. (a) Duration and peak power of soliton at the CF output (b) N_{NLF} as a function of variable CF length

Then the compressed pulse from CF is passed through the NLF where soliton experiences shifting towards a longer wavelength. In the following Figure 3.23, the resultant pulse at the output of NLF is presented, which matches closely with the depicted experimental one in Figure 3.18. As $N_{NLF} \cong 2$, fission in NLF leads to two fundamental solitons. One of them is a self-shifting fundamental soliton ($k = 1$) observed at longer wavelengths, while the other one ($k = 2$) remains at the pump wavelength.

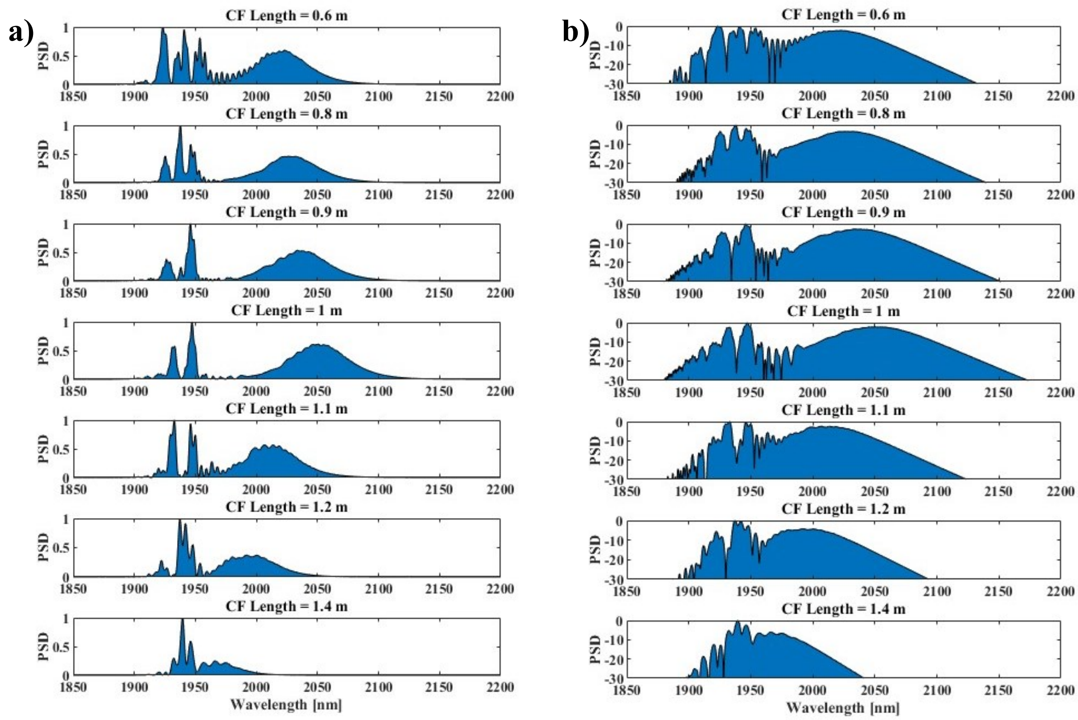

Figure 3.23. Numerical spectrum evolution at the output of the NLF as a function of variable CF length.

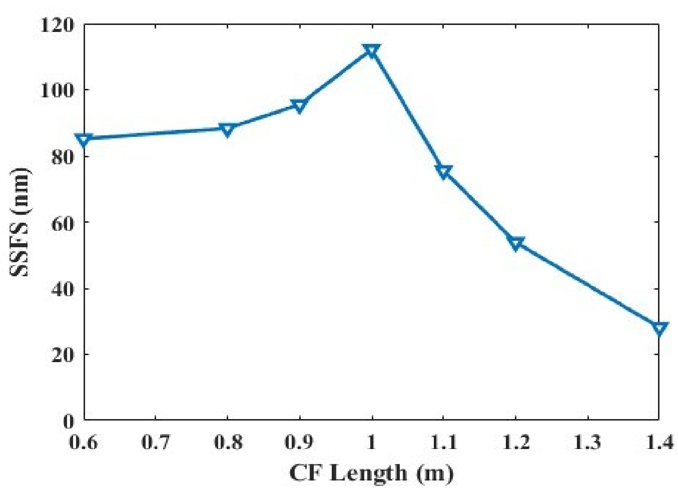

Figure 3.24. SSFS of the soliton as a function of the variable CF length.

The self-shifting soliton's center wavelength shift as a function of the variable CF length is shown in Figure 3.24, which also confirms that the highest compressed pulse point is where the greatest SSFS is obtained. From this result, it is apparent that the prudent choice of the length (up to maximum compression length) of the CF ensures that N_{NLF} is preserved, which further enhances the SSFS in the NLF.

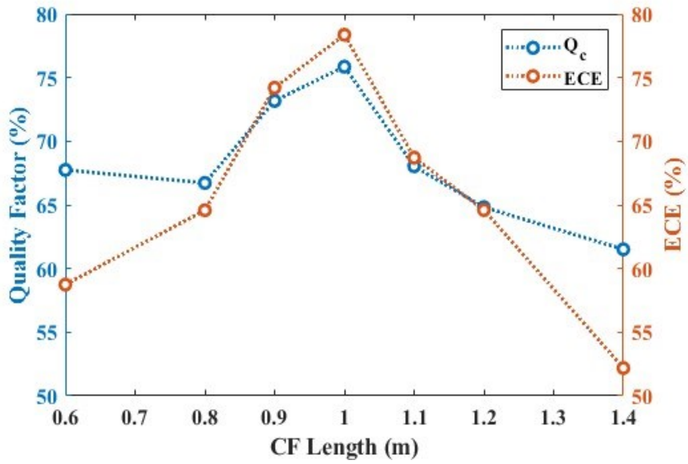

Figure 3.25. Measured ECE and transmission loss of the NLF as a function of the soliton central wavelength.

In Figure 3.25, the Q_{c} of the pulse is numerically evaluated using equation 3.3, which calculates the proportion of energy contained within the main lobe of the compressed pulse. The soliton's energy, which shifts to a longer wavelength, is expected to mirror the trend and quantity of Q_{c}. The proportion of energy in the soliton (ECE) is computed numerically and depicted in the same Figure 3.25. It is worth noting that the ECE exceeds the Q_{c} as the pulse is compressed with the CF length of 0.9 m ~ 1.1 m. At L_{CF}=1 m= L_{c}, the discrepancy is most pronounced, with Q_{c} and side lobes energy accounting for 76% and 24%, respectively, while ECE reaches 78%. The ECE surpassing Q_{c} indicates that energy outside of the main lobe has been utilized by the shifting soliton.

According to the inverse scattering method (ISM), the energy that each fundamental soliton labeled by k carries after fission can be predicted by [18,27,111]:

$$E_{\mathrm{k}} = \frac{2N + 1 - 2K}{N^2} E_0 \tag{3.11}$$

For $k = 1$ soliton, the $\mathrm{ECE_{ISM,1}}$ is 75% when CF length is equivalent to the L_c. However, the ECE in Figure 3.25 likewise exceeds $\mathrm{ECE_{ISM,1}}$. When the compressed pulse from the CF is inserted into the NLF, no additional energy is pumped, hence the extra energy had to have originated from the pedestal evolved during the pulse compression stage. A detailed investigation of the impact of pedestal energy is presented in the following chapter.

4. Chapter 4: Impact of Pedestal Energy on the SSFS

This chapter illustrates the process of formation of the pedestal in the pulse compression stage and investigates the effect of pedestal energy on the SSFS and ECE within the NLF.

4.1 Formation of Pedestal

The compressed pulse achieved through higher-order soliton compression yields the evolution of two side lobes, termed as pedestal.

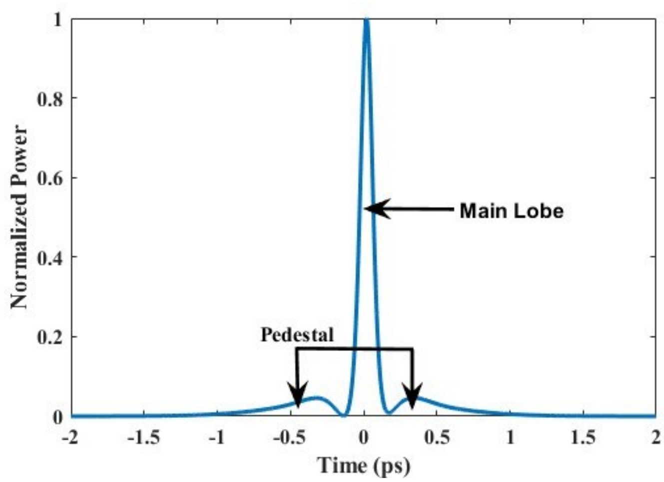

Figure 4.1. A compressed pulse with a short main lobe surrounded by the pedestal.

This is also explained as follows: the excess SPM effect, beyond that experienced by a fundamental soliton, introduces a nonlinear chirp to the pulse. Subsequently, the GVD effect translates this chirp into the pedestal component of the compressed pulse [36]. In the following Figure 4.2, the contour plot (temporal domain) of the maximum compressed pulse with pedestal has been shown as a function of CF length. It is apparent that as the pulse gets compressed, the pedestal starts to evolve. Those pedestal are commonly viewed as undesirable as they hold a significant portion of the energy from the original pulses which results in low-quality compressed pulses [20]. However, the impact of the pedestal in the context of SSFS remains relatively unexplored. In the subsequent section, the impact of the pedestal is thoroughly reviewed.

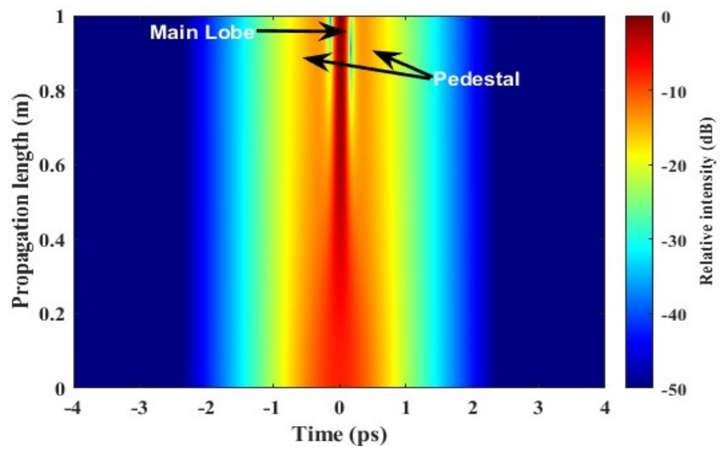

Figure 4.2. Time domain contour plot to show the evolution of compressed main lobe with pedestal as a function of CF length

4.2 Propagation of Pulse through Nonlinear Fiber

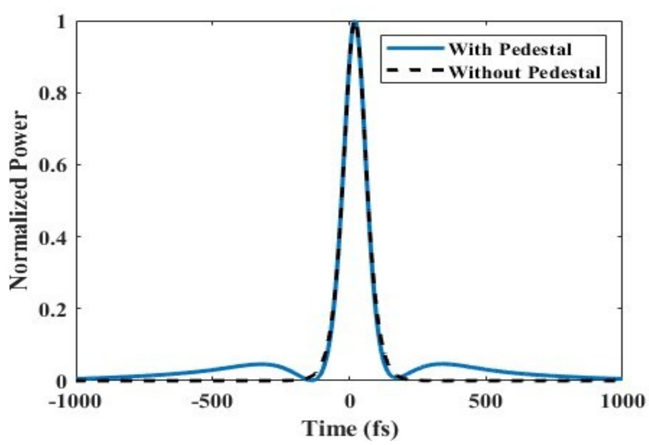

Figure 4.3. Input pulse shapes at the input of NLF with (blue line) or without (black dashed line) pedestal.

To investigate further the impact of the pedestal, two numerical cases are considered: the first is the maximum compressed pulse with the pedestal that is propagated by the 1.7 m long NLF (with the same fiber specifications). The second is an ideal sech pulse with the same initial peak power and duration as the compressed pulse, which is propagated over the same NLF. In Figure 4.3, the solitons at the NLF input have been shown, where the presence of a pedestal is apparent (blue curve) and the ideal sech curve is shown in a black dashed line.

4.2.1 Case of the Ideal Sech Pulse without Pedestal

Figure 4.4 illustrates the 2D plot (temporal domain) of the pulse propagation of an ideal $sech$ pulse throughout the NLF. SSFS begins as soon as the propagation length becomes $0.2\,m$ (approximately). After fission, ($k = 1$) shifts towards the longer wavelength whereas the other one stays at the pump wavelength.

In Figure 4.5, the central wavelength shift of the soliton as a function of the propagation length NLF is shown. Here, it is apparent that there is a continuous transfer of energy from lower to higher frequencies, which is the prime candidate for the explanation of such spectral shifts.

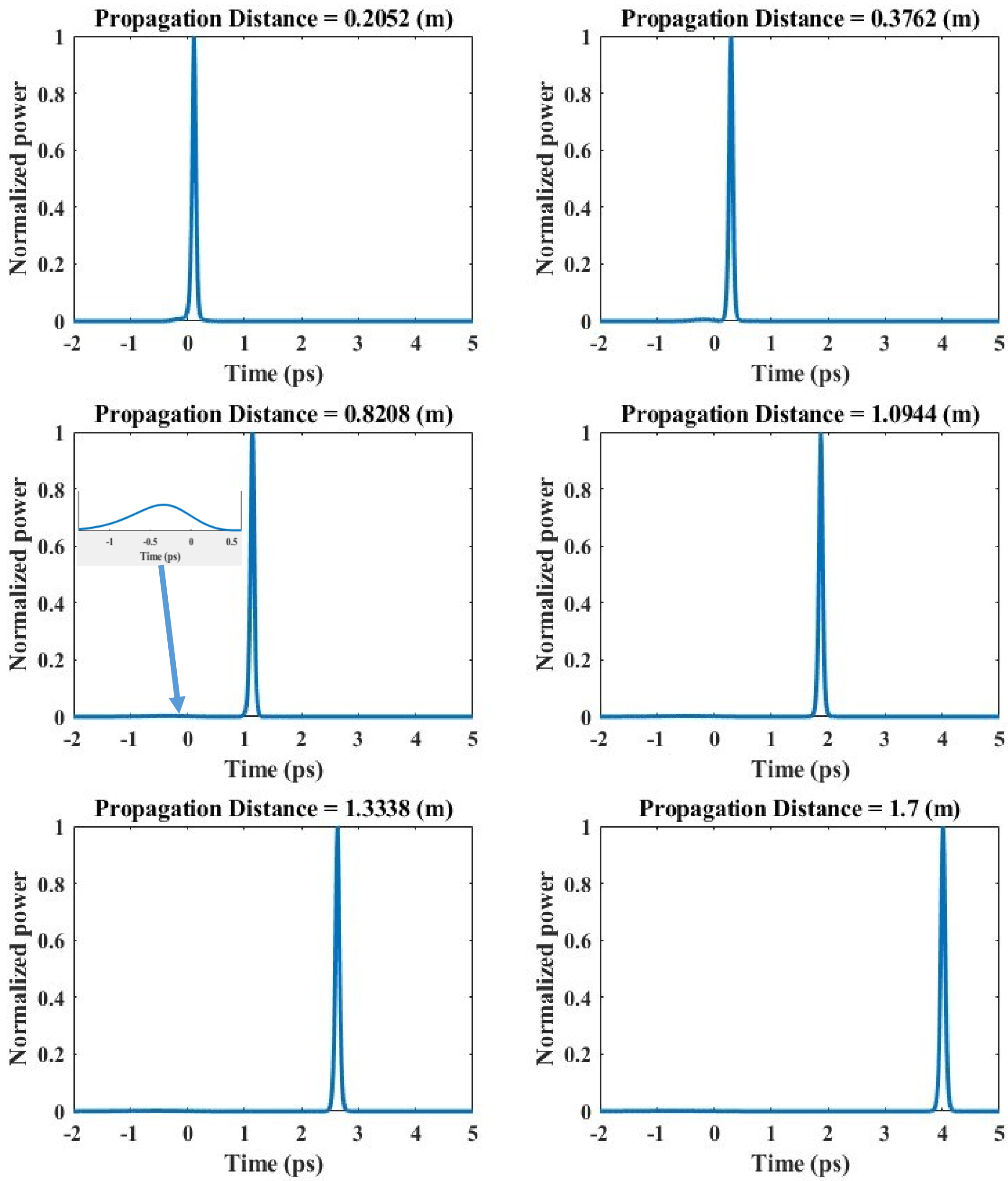

Figure 4.4. SSFS of the sech pulse in the time domain at different propagation distances of NLF

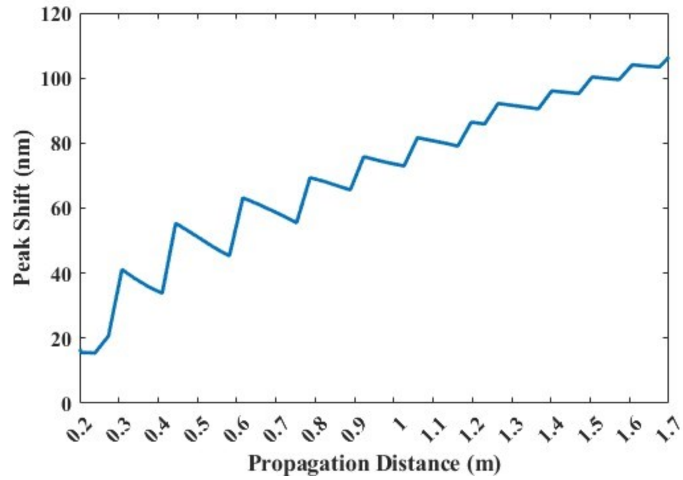

Figure 4.5. Central wavelength shift of soliton as a function of propagation distance of NLF

Figure 4.6 depicts the peak power and the duration of the wavelength-shifted soliton as a function of propagation length. The trend of fluctuation in peak power corresponds to that of the fluctuating soliton duration to maintain the soliton energy.

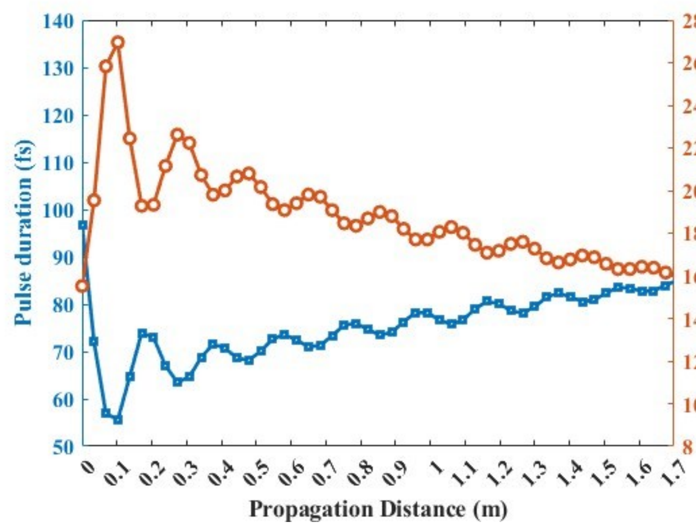

Figure 4.6. Peak power and pulse duration at each propagation distance in NLF

Figure 4.7 presents the soliton's energy (according to equation 3.5) with each propagating distance of NLF. Note in Figure 4.7 that the asymptotic trend of energy as a function of NLF length is an expected decrease caused by the one-to-one photon conversion of the Raman-induced SSFS.

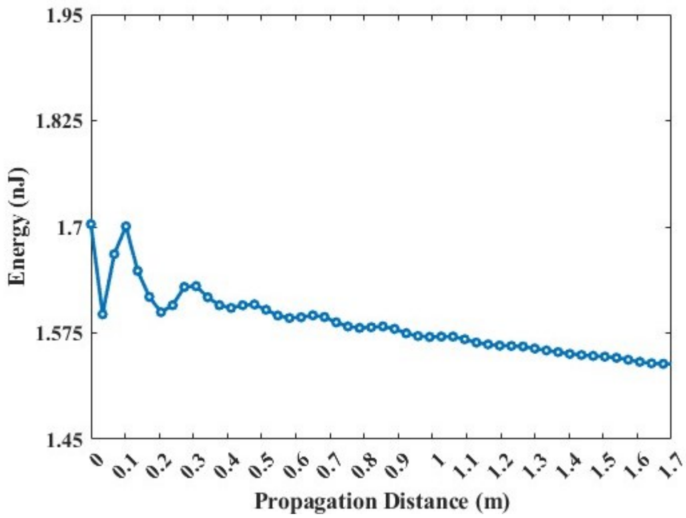

Figure 4.7. The energy of the shifting soliton at each propagation distance in NLF

Figure 4.8 shows a contour map of the propagated sech pulse in NLF in both the temporal and spectral domains. We can observe the pump residual on the left side and the continuously delayed soliton (in the time domain) or spectrally shifted soliton (in the frequency domain) on the right side as a function of propagation length.

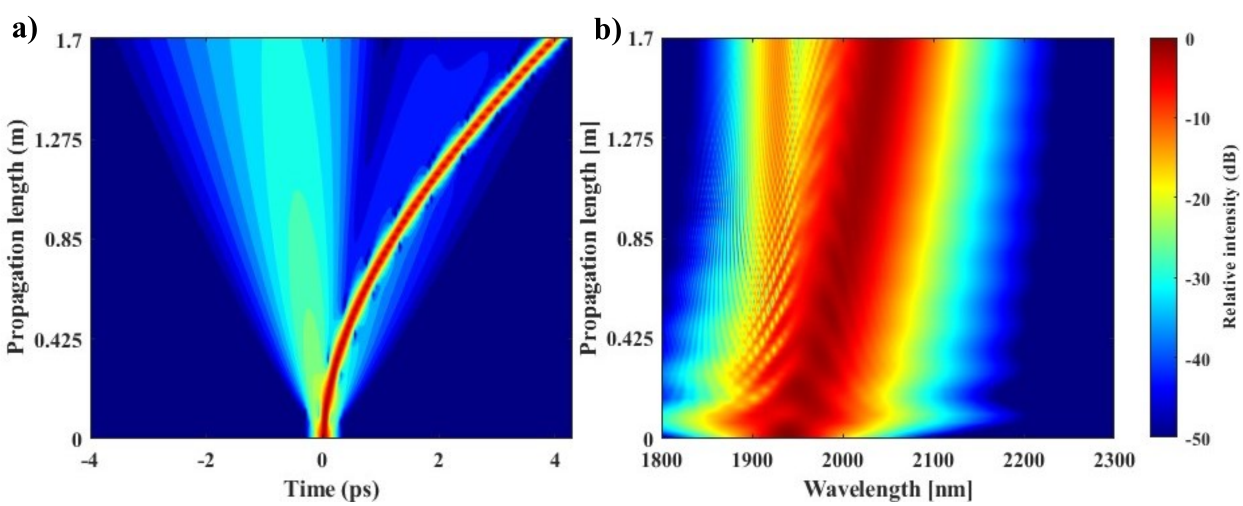

Figure 4.8. Contour plot of the sech pulse in NLF (a) Time domain (b) Frequency domain

4.2.2 Case of the Sech Pulse with Low Peak Gaussian Pulse

The same sech pulse combined with a low peak Gaussian pulse as a pedestal will be evaluated in this case. First, the pedestal component of the output from the CF is filtered in Figure 4.9(a), and the peak power and pulse width are extracted. Next, a Gaussian curve is plotted with the same peak power and pulse duration, delayed by 1 ps from the sech pulse. Finally, the sech pulse is combined with the Gaussian pulse (see Figure 4.9(b)).

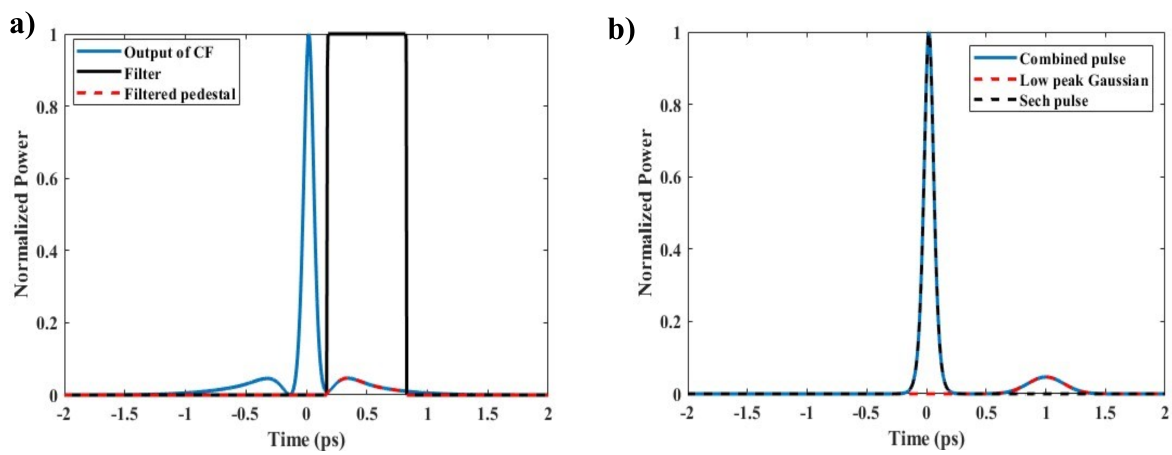

Figure 4.9. (a) Filtering pedestal from the compressed pulse (b) Combined pulse with a sech pulse as main lobe and low peak Gaussian pulse as a pedestal.

This combined pulse is now passed through the same length of NLF, and the following Figure 4.10 depicts the temporal profile of the pulse throughout the propagation distance. At the propagation distance of around 0.75 m, the shifting soliton gets superimposed with the Gaussian pulse. It is apparent from the figure that after collision the Gaussian pulse seems comparatively smaller than pre-collision stage. That indicates some energy transfer between the Gaussian pulse and the shifting soliton.

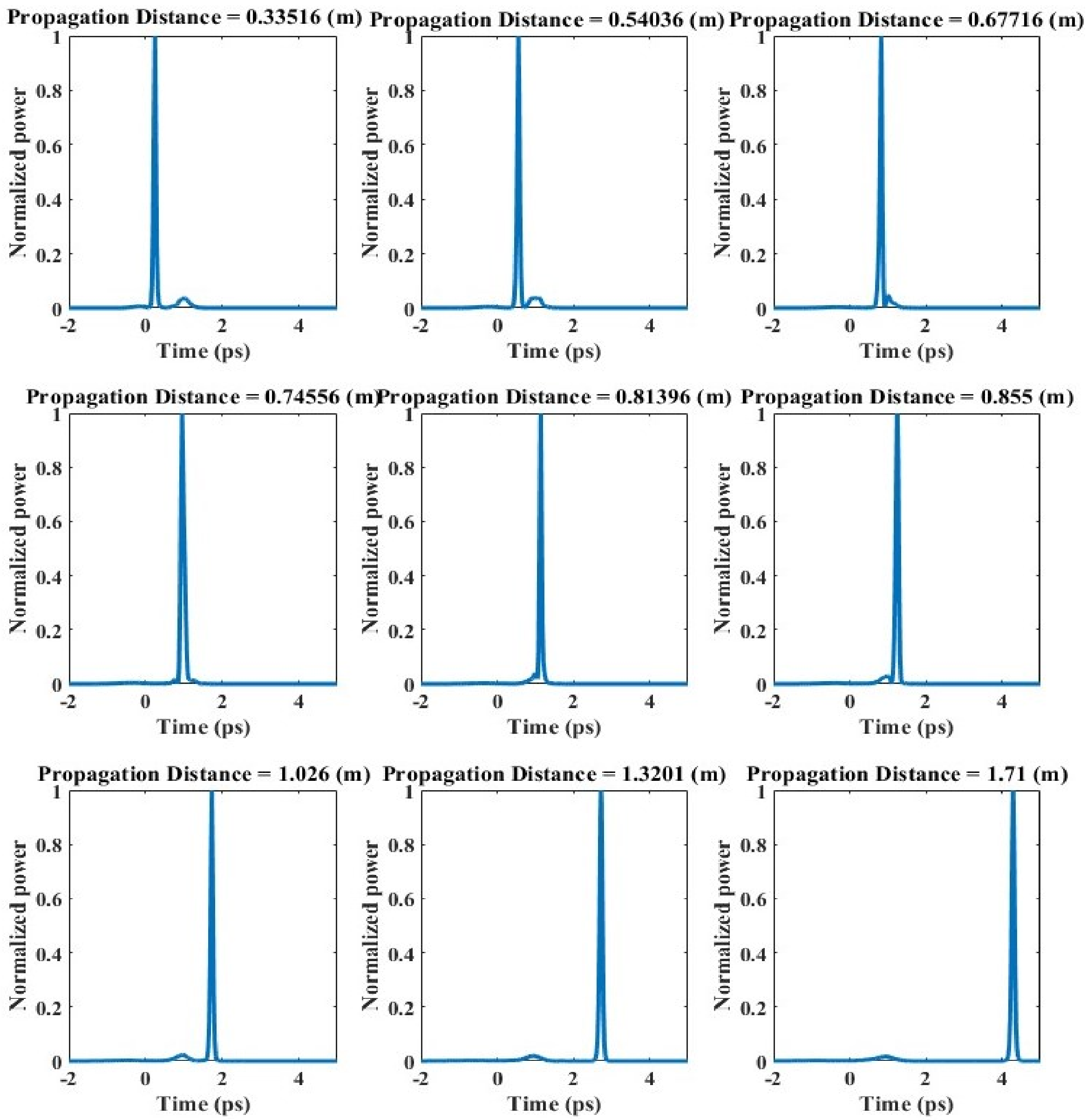

Figure 4.10. SSFS of the combined pulse in the time domain at different propagation distances of NLF

The next Figure 4.11(a) shows the peak power and pulse duration of the soliton during its propagation length of NLF. It can be observed from Figure 4.11(b) that until the propagation distance ≅ 0.45 m, the curve resembles the Figure 4.7. After that point, the shifting soliton starts to collide with the Gaussian pulse and the energy peaks at the collision point.

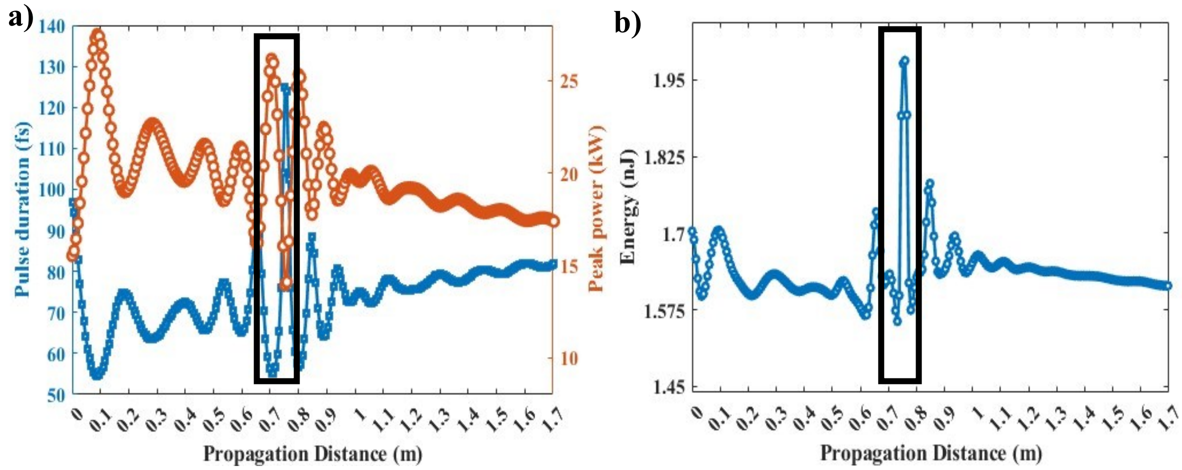

Figure 4.11. (a) Peak power and pulse duration at each propagation distance in NLF (b) The energy of the shifting soliton at each propagation distance in NLF

In Figure 4.12, the contour plot of the temporal domain and the spectral domain are shown, respectively. Raman-induced perturbation forces pulses to shed some energy early on, after which they reshape to form Raman solitons whose spectra redshift continually. The spectral fringes, on the other hand, result from the beating of two temporally separated optical pulses [125]. From the temporal domain, it is apparent that the collision of the shifting soliton and the Gaussian pulse starts around 0.45 m.

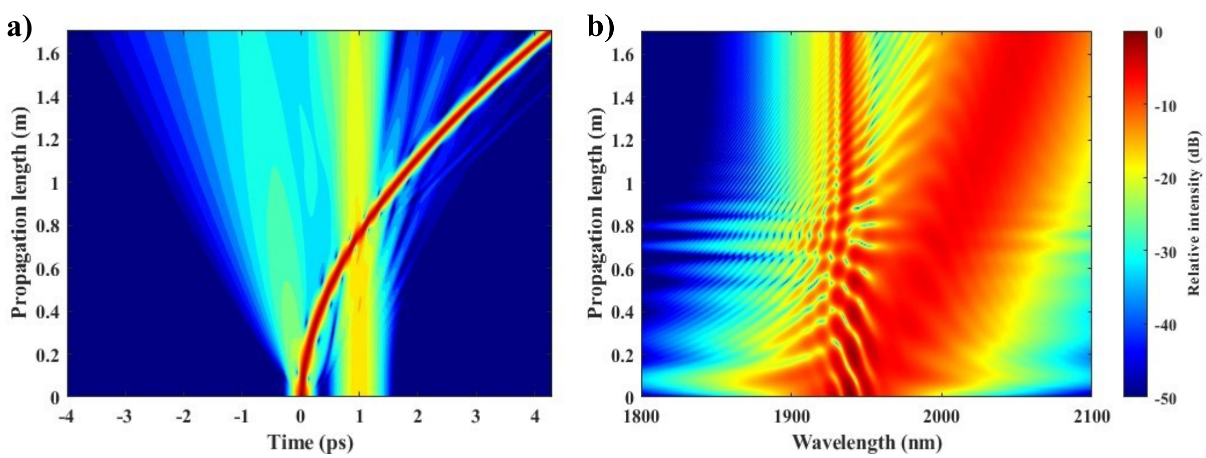

Figure 4.12. Contour plot of the sech pulse with the Gaussian pulse in NLF (a) Time domain (b) Frequency domain

Now to observe if any energy is transferred from the pedestal or not, the Gaussian pulse was filtered, and the energy is calculated. However, from the point the shifting soliton interacts with the pedestal, the pedestal (low peak Gaussian pulse) gets distorted and gains energy (momentarily) from the shifting soliton. Hence, the peak power and pulse duration are extracted from the filtered pulse and fitted with a Gaussian pulse (Figure 4.13(a)). Then the energy of the Gaussian pulse is calculated at each point of the distance of NLF (Figure 4.13(b)).

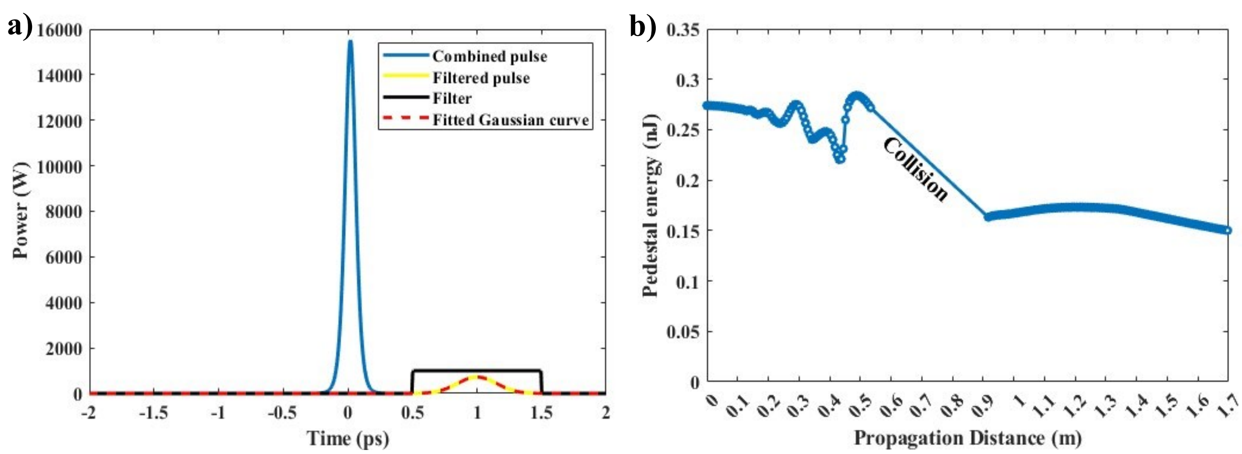

Figure 4.13. (a) Filtered pedestal in temporal domain (b) Pedestal energy at each propagation distance of NLF

Figure 4.13(b) shows how the energy of the Gaussian pulse increases in the pre-collision stage when the shifting soliton delays in time and approaches the Gaussian pulse. The energy then reclines after the collision, indicating that some energy is transmitted during the collision. Graphical observation from Figure 4.13(b) suggests that 32% energy from the Gaussian pulse is used. Furthermore, when compared to Figure 4.7's energy curve, Figure 4.11(b) confirms that the moving soliton preserves the energy obtained from the Gaussian curve.

These studies [126,127] have also shown that soliton interaction due to the collision can effectively change the amplitude of the solitons involved. Now one may ask why this energy transfer is happening. In our case, two temporally separated optical pulses of the same wavelength propagate inside a single-mode fiber. The leading pulse is a sech pulse and a dominant one due to its relative intensity. The sech pulse sheds some energy to form into a soliton, whose spectra continuously redshift and temporally overlap with the low peak Gaussian pulse. Note that if there is some temporal overlap between the pulses, energy redistribution happens due to inter-pulse Raman scattering [125,128,129]. This is particularly significant in soliton dynamics because the shifting soliton effectively captures energy from the Gaussian pulse through this process, enhancing its own energy and shifting its frequency further.

Effect of variable temporal separation:

In this case, the low peak Gaussian pulse is separated by 1 ps. Additionally, other scenarios were considered, where the Gaussian pulse is separated by 1~3 ps. As shown in Figure 4.14, increasing the temporal separation from the sech pulse results in a slight reduction in energy transfer. Therefore, in the case of real pedestal adjacent to the main lobe will ensure higher energy transfer.

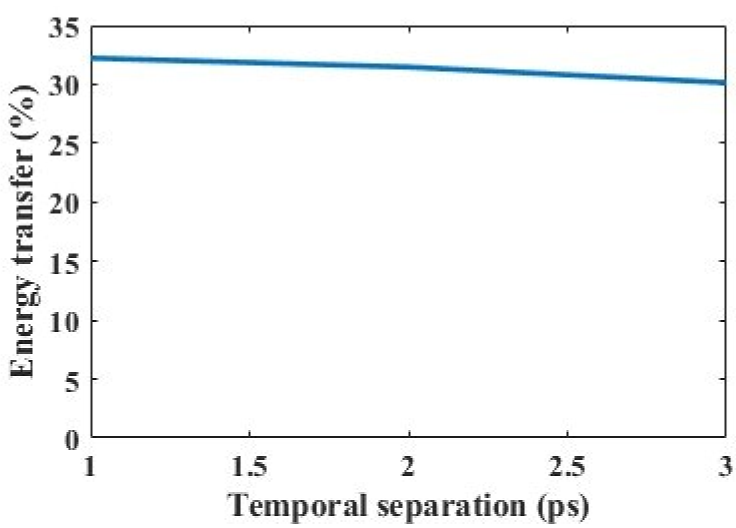

Figure 4.14. Percentage of energy transfer as a function of the temporal separation of Gaussian pulse

Effect of variable peak power:

Here, the peak power of the 1 ps temporally separated Gaussian pulse has been taken as 2.5-10% of the peak power of the sech pulse. Figure 4.15 indicates that, with the increase of the peak power of the Gaussian pulse, the amount of energy transferred to the shifting soliton is increased.

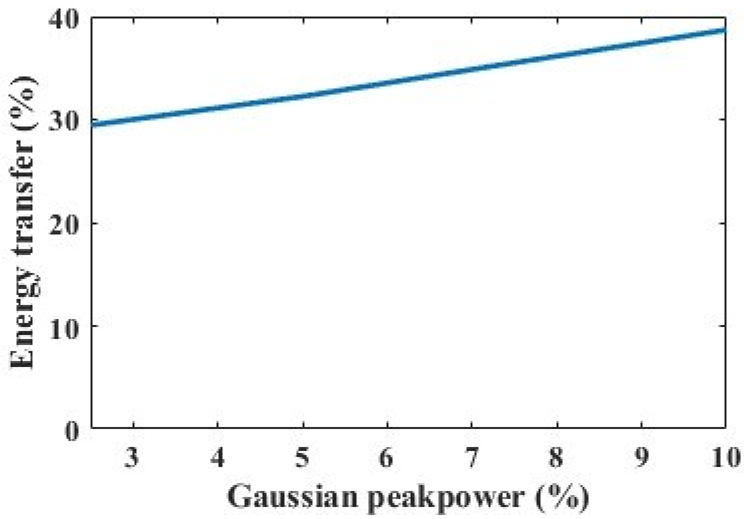

Figure 4.15. Percentage of energy transfer as a function of the peak power of Gaussian pulse

An interesting phenomenon is noted while the peak power of the Gaussian pulse is extended beyond 10% of the sech pulse. It is observed that within NLF, the sech pulse continues to delay and approaches the Gaussian pulse. When the leading pulse (Sech pulse) approaches the trailing pulse (Gaussian pulse), they exchange energy via inter-pulse Raman scattering. As a result, the following pulse gains energy, compresses inside the NLF, and eventually fissions. The fissioned new soliton begins to move away from the other one. As the leading pulse had a higher peak power it catches up with the trailing pulse after propagating a certain distance. In the following Figure 4.16 shows the contour plot when peak power of the Gaussian pulse is 20%, 25%, and 50% of the sech pulse.

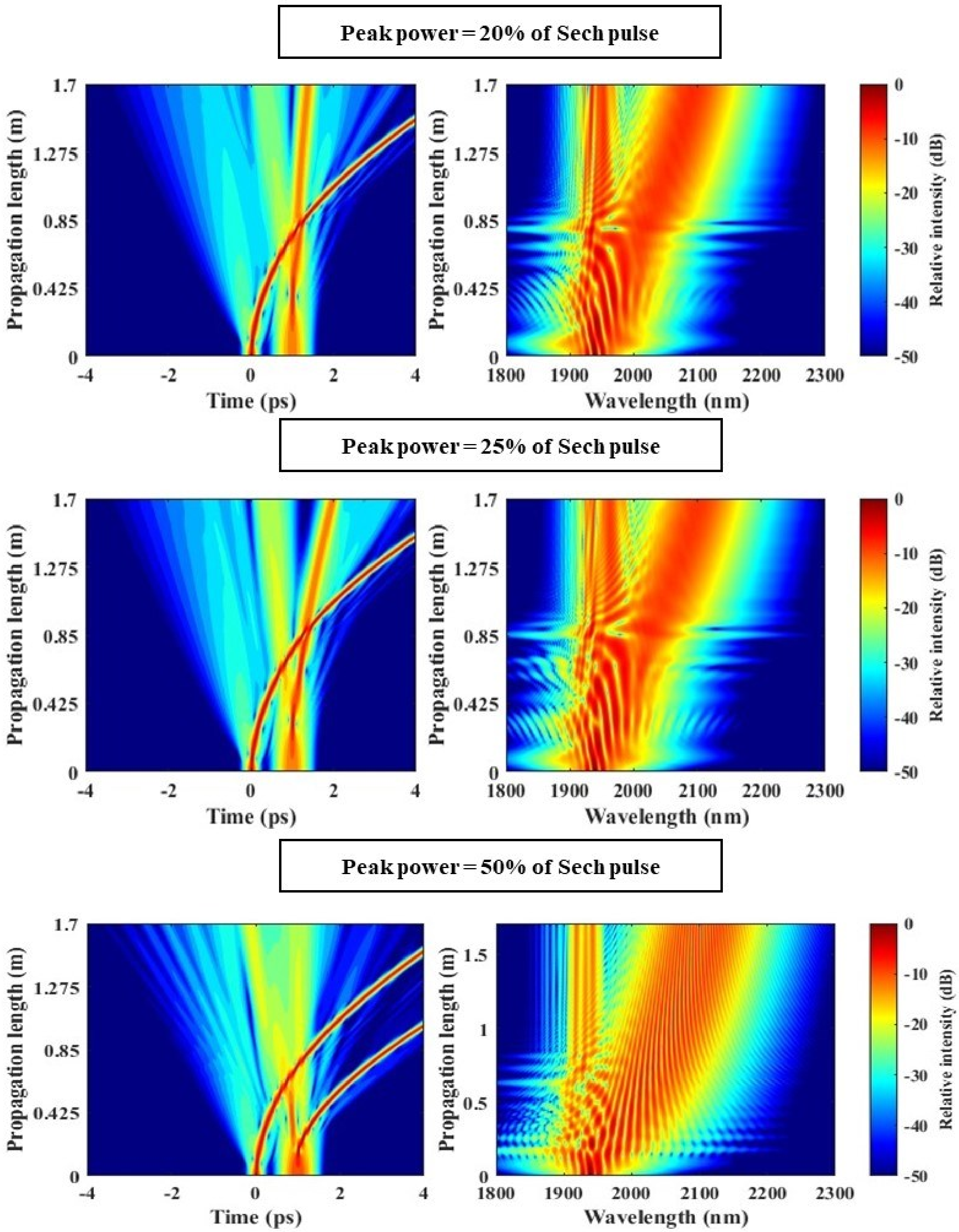

Figure 4.16. Contour plot of sech pulse with Gaussian pulse for various peak power

For the peak power of 20% and 25%, the sech pulse crosses the Gaussian pulse. The Gusiian pulse then transfers energy from it, and then delays at a reduced speed. However, when the peak power of Gaussian reaches 50% of that of the sech pulse, both pulses never get merged but interact via inter-pulse Raman gain and both move towards longer wavelength. A fringe pattern is observed in the spectrum domain for this case., which can be explained as follows. When one pulse interacts with another, it produces a dispersive wave that releases energy. The red-shifting of the pulses (due to different initial peak powers) causes interference in the radiation released by each pulse, resulting in the fringe pattern in Figure 4.16. An investigation demonstrated that soliton collisions can produce dispersive waves [130].

This phenomenon also indicates that if the energy of the pedestal (proportional to peak power) becomes higher, then it might not comply with the soliton order preservation theory as multiple solitons will be involved, which will result in reduced ECE. Hence, the pedestal will be problematic in systems that involve a higher-order soliton with a comparatively large N. The reason behind that is, during compression, the higher the soliton number, the more energy will be directed towards the pedestal [20,121]. If the pedestal is strong relative to the soliton, the interference between the pedestal and the soliton can distort the soliton's shape, making its propagation less efficient. Therefore, for applications requiring efficient soliton propagation, it's crucial to manage the soliton number N to control the energy distribution between the main pulse and the pedestal.

Effect of variable pulse duration:

For the Gaussian pulse, the pulse duration is varied from 100 fs to 400 fs. Figure 4.17 shows that a temporally stretched pulse width of the Gaussian pulse results in better energy transfer from the

Gaussian to the shifting soliton. This temporal stretching can be done for real pedestal cases by utilizing chirp in the input pulse.

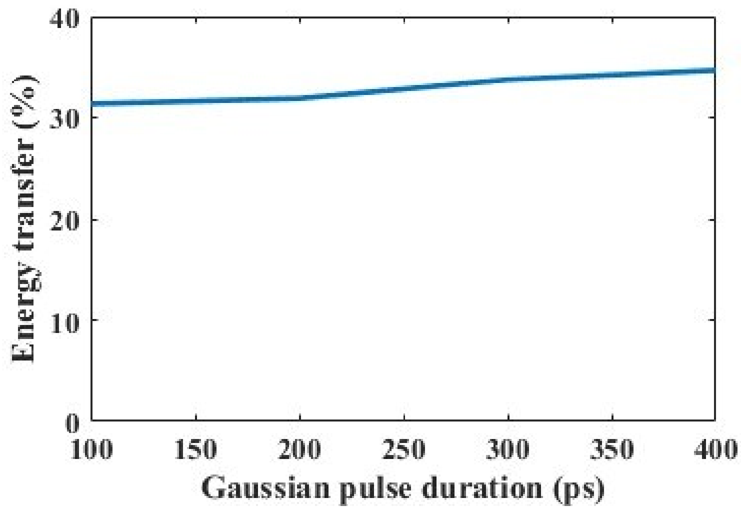

Figure 4.17. Percentage of energy transfer from the Gaussian pulse as a function of the duration of the Gaussian pulse

Effect of variable initial wavelength:

Figure 4.18 shows that when the initial wavelength of the Gaussian pulse is altered, it starts to delay in time and moves away from the shifting soliton. As the shifting soliton has more intensity, hence it catches up with the Gaussian pulse and merges with it. However, the NLF length requirement to happen the temporal overlap between the Gaussian pulse and the shifting soliton depends on the wavelength separation between them. If the wavelength separation is greater, then the NLF length required is also higher. The following Figure 4.18 shows the contour plot of the cases where the initial wavelength separation is 0, 25, and 50 nm for L_{NLF} of 1.7 m, 3 m, and 6 m, respectively.

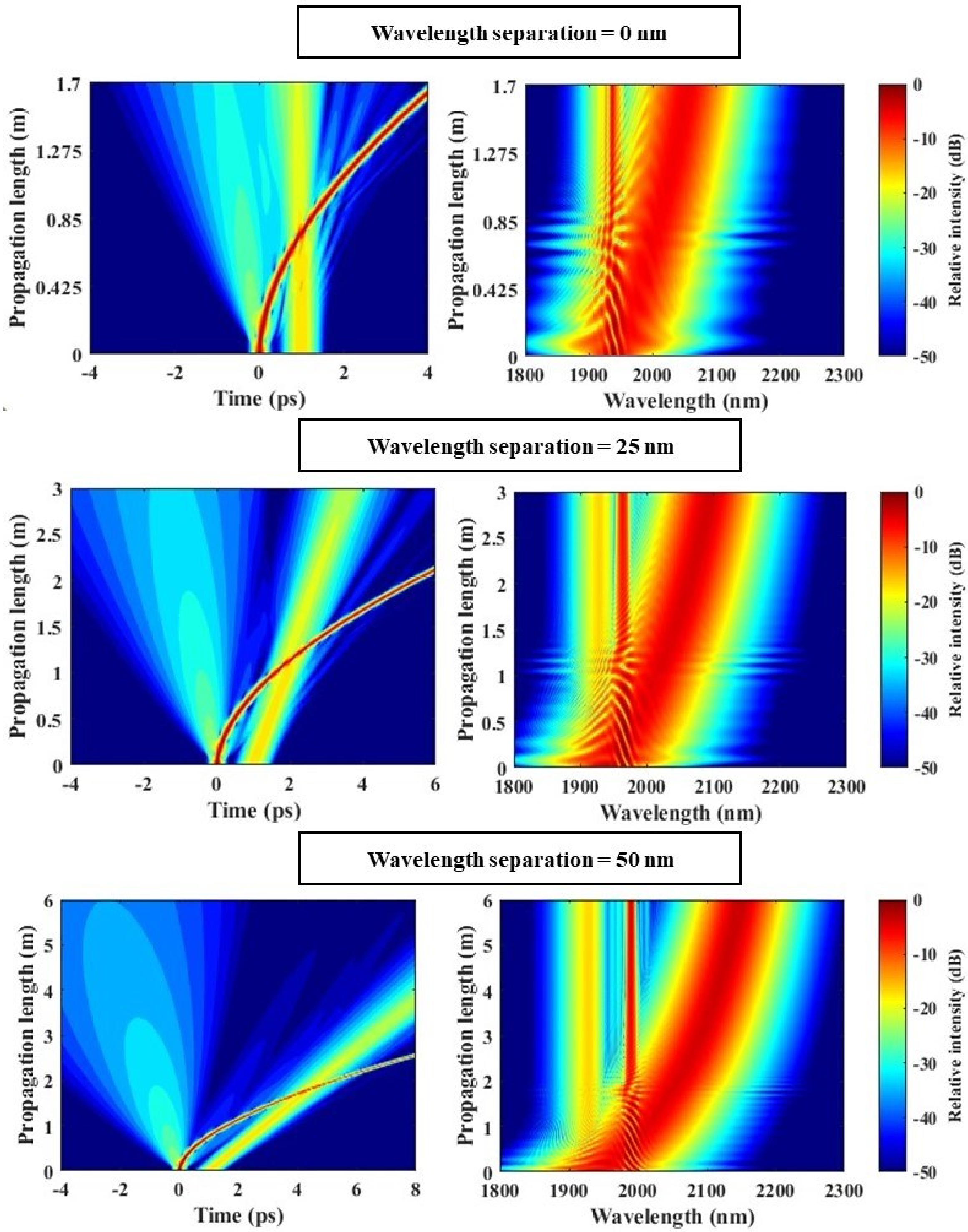

Figure 4.18. Contour plot of the sech pulse with Gaussian pulse for various initial wavelength separation

The following Figure 4.19 demonstrates that there is only a slight increase if the initial wavelength of the Gaussian pulse is varied.

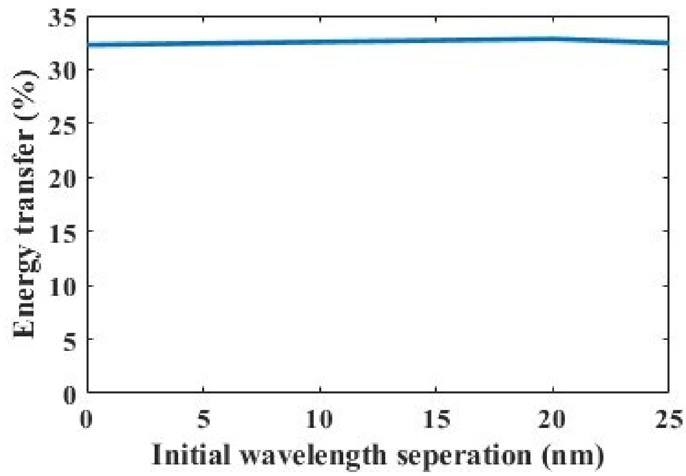

Figure 4.19. Percentage of energy transfer from the Gaussian pulse as a function of the initial wavelength separation

To summarize, raising the peak power or total energy of the Gaussian pulse has the most impact on the energy transfer from the Gaussian pulse. Keeping this in mind, the actual case of the pedestal is first analyzed and then optimized in the following sections.

4.2.3 Case of the Compressed Pulse with Pedestal

Figure 4.20 shows the plot of SSFS in the time domain at different propagation distances of NLF. At a distance of 0.2 m, peak shifting due to SSFS starts to occur, and at 0.45 m (approximately) the shifting soliton overlaps with the right pedestal. It is evident from Figure 4.20 that after the overlap the right pedestal becomes smaller than the left side, which indicates the power transfer from the right-side pedestal to the spectrally shifted soliton.

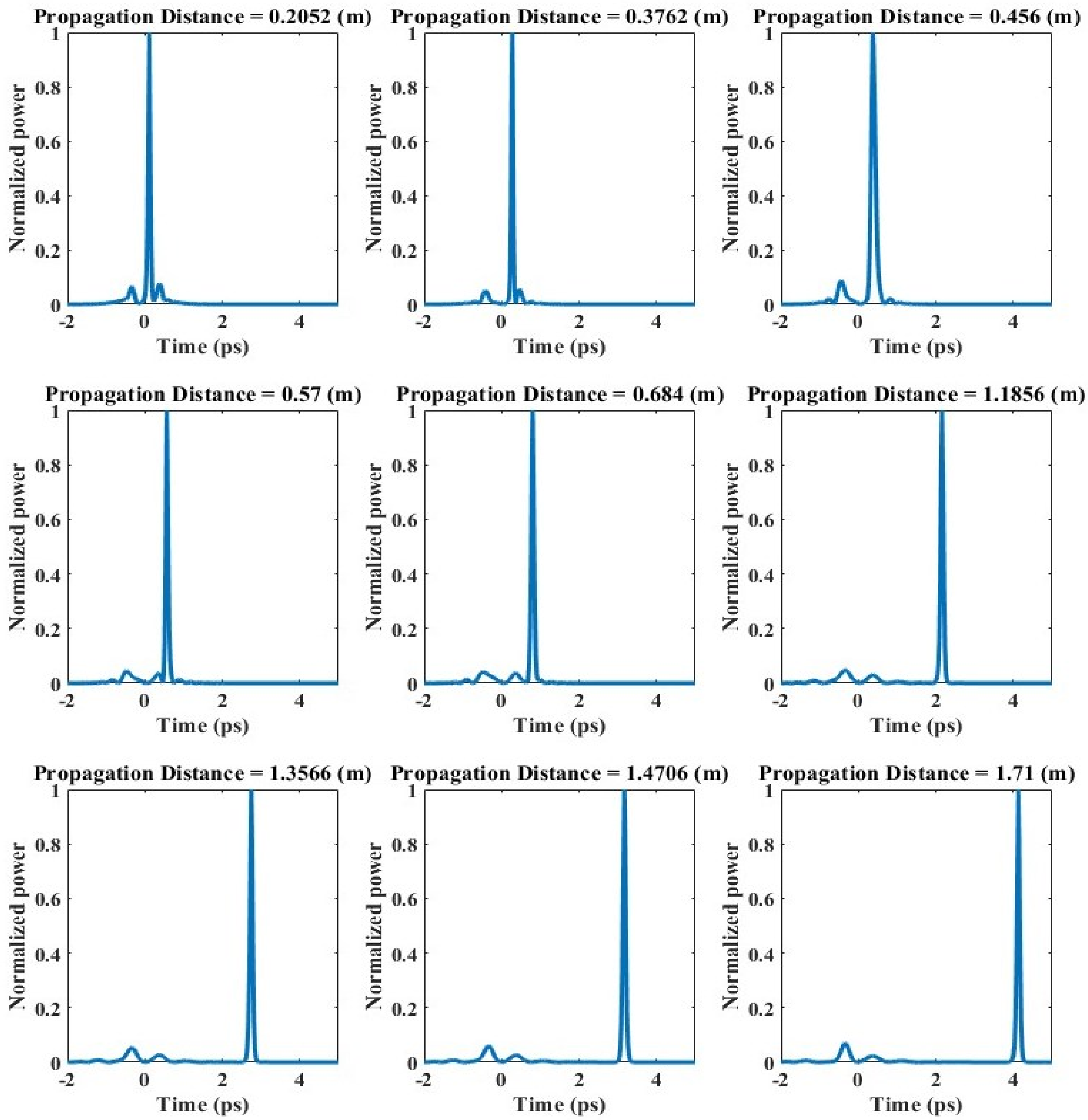

Figure 4.20. SSFS of the actual compressed pulse accompanied by its pedestal in the time domain at different propagation distances of NLF

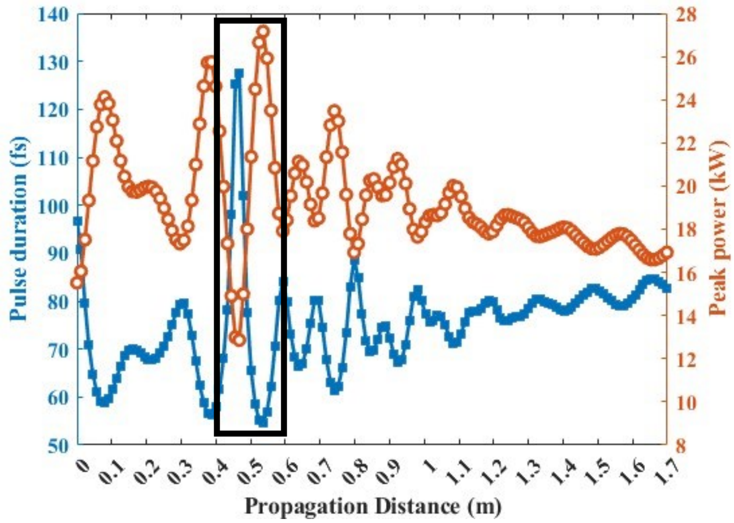

Figure 4.21. Peak power and pulse duration at each propagation distance in NLF

Figure 4.21 proves that this overlap elevates the peak power, subsequently leading to a reduction in soliton duration. This reduction in duration enhances the SSFS eventually. Figure 4.22 confirms that the overlap between the pedestal and the shifting soliton results in further improvement in the soliton energy (derived from equation 3.5). Note that if the increase in energy were due to momentary superposition, the energy level would return to its pre-interference level after the overlap. However, after the interference region (highlighted box), the soliton consistently retains higher energy than the ideal sech pulse case in Fig. 4.7 as it propagates, this indicates retention of the transferred energy.

Figure 4.23(a) verifies that following fission, the shifting soliton is superimposed on only the right pedestal. Graphically, it can be observed that some energy is being transferred from the right pedestal to the main lobe at the propagation distance of 0.45 m (approximately). The energy transfer from the pedestal to the shifting soliton is primarily driven by the inter-pulse Raman effect [125,128,129]. Here, after temporal overlap between the pedestal and the shifting soliton, the pedestal components start pumping the shifting soliton, which results in the soliton acquiring energy from the pedestal, increasing its intensity and further shifting toward a longer wavelength.

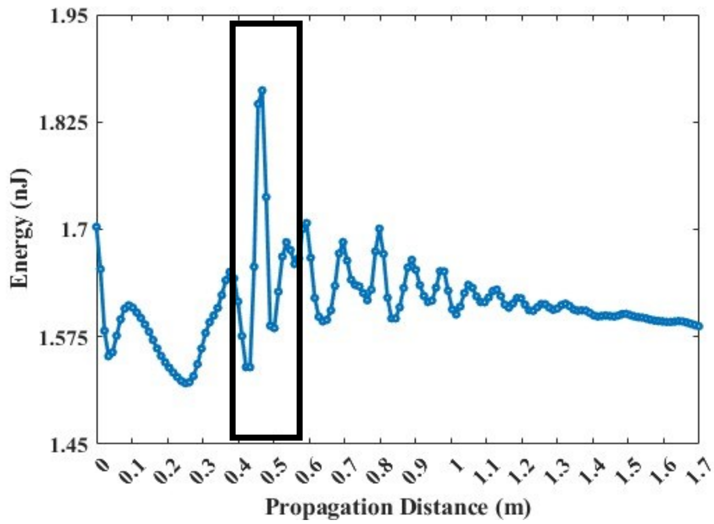

Figure 4.22. The energy of the soliton at each propagation distance in NLF

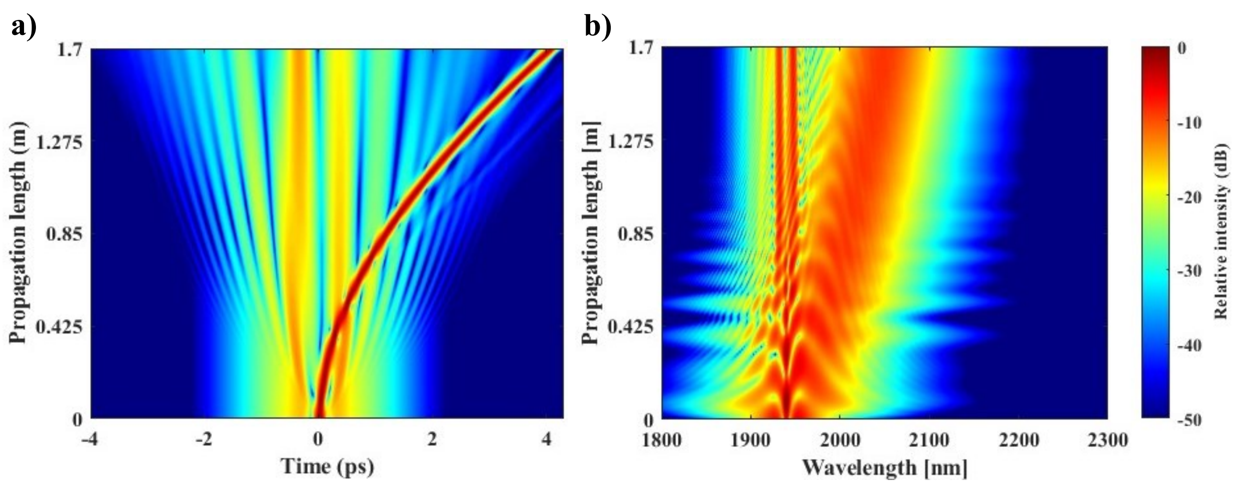

Figure 4.23. Contour plot of compressed pulse (with pedestal) propagated through NLF (a) Time domain (b) Frequency domain

Next, the pedestal is filtered and the energy at each propagation point of NLF (according to the area under the curve method) is plotted in the following Figure 4.24. The superposition of the shifting soliton on the pedestal impedes the filtering of the pedestal; hence, the energy computed for the pre- and post-collision stages. Furthermore, graphical observation from Figure 4.24 reveals that approximately 52% of the energy allocated to the right pedestal of the compressed pulse is retrieved and utilized throughout the SSFS process, hence enhancing its effectiveness. Hence, despite the evolving pedestal, pulse pre-compression using CF is demonstrated to be beneficial in the context of SSFS, as it facilitates partial retrieval of pedestal energy.

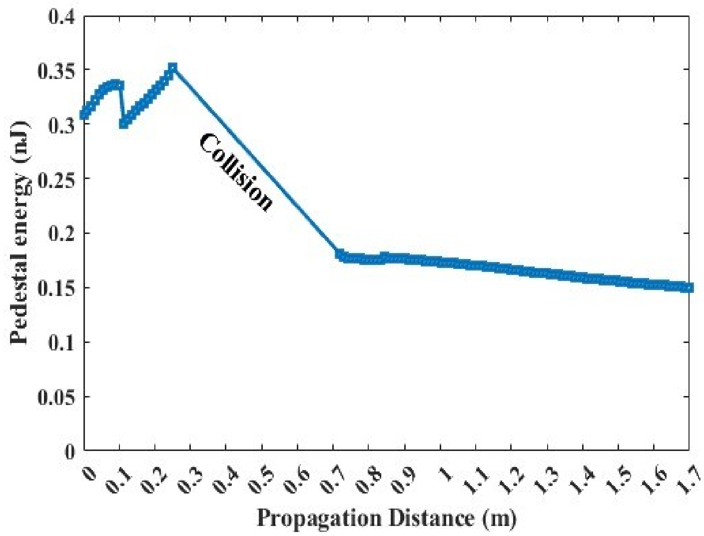

Figure 4.24. Pedestal energy at each propagation distance of NLF

4.2.4 Comparison of Wavelength Shift due to SSFS with/without Pedestal

The sech pulse was fitted with the central peak of the original compressed pulse. Therefore, the sech pulse has the same energy as the central lobe of the compressed pulse. However, Figure 4.25 indicates that the SSFS in NLF remains 5 nm higher in the compressed pulse case than in the case where the pedestal didn't evolve (sech pulse). This further indicates that the energy in the pedestal is getting partly recycled, hence improving the SSFS in NLF. Furthermore, as shown by calculating from Figures 4.7 and 4.22, the spectrally shifted soliton carries 3% more energy than without the pedestal case, explaining why the ECE is greater than the expected ECE_{ISM}. Hence, despite the fact that pulse pre-compression enhances the energy transfer to the pedestal, the partial recycling of this pedestal energy by the shifting soliton limits the energy loss, enabling an optimal SSFS and ECE for a CF length equal to the maximum compression length.

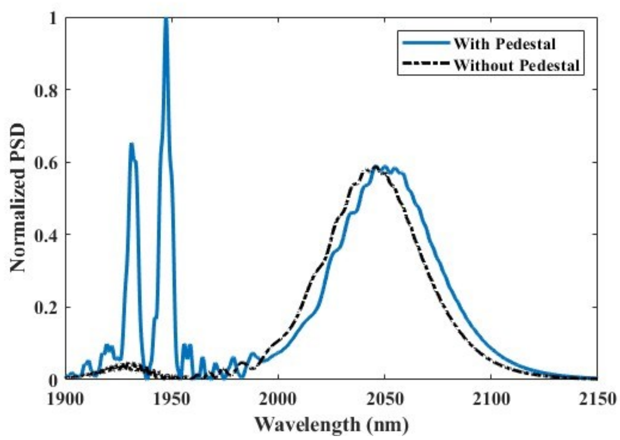

Figure 4.25. Output pulse shapes after propagation through NLF with (blue line) or without (black dashed line) pedestal.

4.2.5 Optimizing the Shape of the Pedestal

Based on the study involving the sech pulse combined with a low peak Gaussian, it appears that raising the pedestal's energy (proportional to peak power) will result in a better transfer of energy towards the moving soliton than changing parameters. It was demonstrated that the shifting soliton gets superimposed only on the right-side pedestal, which suggest that increasing energy content in the right-side pedestal will be a better strategy to optimize the shape of the compressed pulse.

In the case of the pulse propagating through a medium with third-order dispersion (TOD), asymmetric spectral broadening can occur. This can lead to one side of the pulse (either the leading or trailing edge) spreading out more than the other, causing an asymmetric energy distribution during compression. As a result, the pulse can develop an asymmetric pedestal, with one side of the pulse having more energy than the other [131,132]. As chirping the input pulse significantly affects the spectral domain, the combination of chirp and TOD can lead to a more pronounced asymmetric broadening of the pulse. With the assistance of both phenomena, an optimized compressed pulse shape is formed with asymmetric pedestal (Figure 4.26), where most of the energy resides in the right-side pedestal.

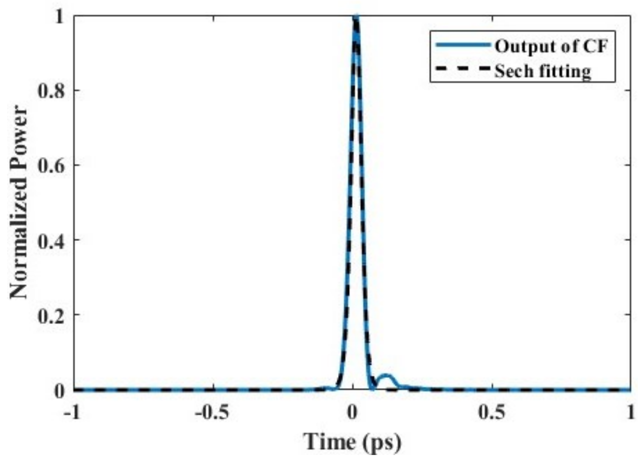

Figure 4.26. Optimized compressed pulse shape with maximum energy in the right pedestal

In Figure 4.26, the shape of the compressed pulse is optimized with $Q_c = 90.48\%$, where the right pedestal contains 7.06% of energy. Figure 4.27 shows the 2D and Contour plot of the chirped compressed pulse propagated through NLF. After propagation through the NLF, the wavelength shift is 182 nm and the ECE is 91.65%. Numerical analysis suggests that as high as 26% energy from the right pedestal is utilized during the SSFS of shifting soliton, which means 20% of the energy from the pedestal is getting recycled.

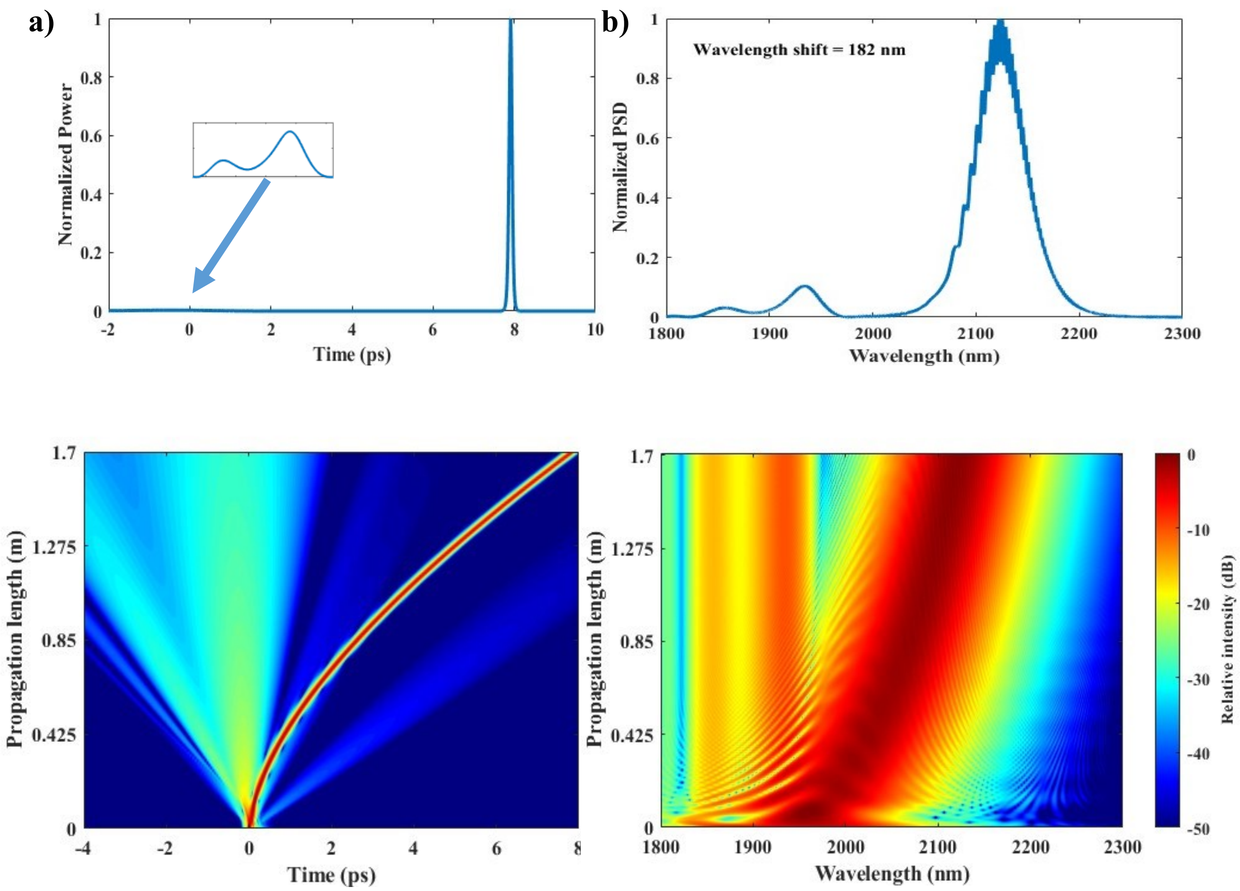

Figure 4.27. 2D and Contour plot of chirped compressed pulse propagated through NLF (a) Time domain (b) Frequency domain

Conclusion

This thesis dissertation discusses the optimal design conditions of an SSFS-based wavelength converter with pulse pre-compression. However, in the pulse pre-compression stage, the compressed pulse achieved through higher-order soliton compression leads to a compressed main lobe surrounded by the pedestal. Accordingly, it appears that there is a trade-off between reducing the pulse width through pulse pre-compression before the SSFS stage and transferring energy to the pedestal. Further investigation reveals that during SSFS, as high as 26% of pedestal energy is effectively recycled by the shifting soliton to simultaneously maximize SSFS and ECE. Later, an optimised compressed pulse shape was proposed, resulting in a wavelength shift of 182 nm and an ECE of 91.65%, with 26% of energy from the right-pedestal being utilized during the SSFS of shifting soliton.

Future Directions

The interaction between a shifting soliton and its accompanying pedestal in nonlinear optical fibers presents a wide scope for further research. The fiber parameters (e.g., dispersion or nonlinearity profile) and pulse characteristics (e.g., chirp and dependences on the initial values of relative phase) can be varied numerically to map the conditions under which energy transfer is optimized or minimized. Then an experimental verification of those predictions would be of considerable interest.

Reference

1. "Extending opportunities," Nat. Photonics **6**(7), 407–407 (2012).

2. T. P. J. Blaikie, J. Couper, G. Hancock, P. L. Hurst, R. Peverall, G. Richmond, G. A. D. Ritchie, D. Taylor, and K. Valentine, "Portable Device for Measuring Breath Acetone Based on Sample Preconcentration and Cavity Enhanced Spectroscopy," Anal. Chem. **88**(22), 11016–11021 (2016).

3. P. M. Santos, E. R. Pereira-Filho, and L. E. Rodriguez-Saona, "Application of Hand-Held and Portable Infrared Spectrometers in Bovine Milk Analysis," J. Agric. Food Chem. **61**(6), 1205–1211 (2013).

4. L. M. F. Barreira, Y. Xue, G. Duporté, J. Parshintsev, K. Hartonen, M. Jussila, M. Kulmala, and M.-L. Riekkola, "Potential of needle trap microextraction–portable gas chromatography–mass spectrometry for measurement of atmospheric volatile compounds," Atmos. Meas. Tech. **9**(8), 3661–3671 (2016).

5. Y. Huang, J. Jivraj, J. Zhou, J. Ramjist, R. Wong, X. Gu, and V. X. D. Yang, "Pulsed and CW adjustable 1942 nm single-mode all-fiber Tm-doped fiber laser system for surgical laser soft tissue ablation applications," Opt. Express **24**(15), 16674 (2016).

6. I. Alamgir, F. St-Hilaire, and M. Rochette, "All-fiber nonlinear optical wavelength conversion system from the C-band to the mid-infrared," Opt. Lett. **45**(4), 857 (2020).

7. L. Li, N. Abdukerim, and M. Rochette, "Mid-infrared wavelength conversion from As_2Se_3 microwires," Opt. Lett. **42**(3), 639 (2017).

8. S. Venck, F. St-Hilaire, L. Brilland, A. N. Ghosh, R. Chahal, C. Caillaud, M. Meneghetti,

J. Troles, F. Joulain, S. Cozic, S. Poulain, G. Huss, M. Rochette, J. M. Dudley, and T. Sylvestre, "2–10 µm Mid-Infrared Fiber-Based Supercontinuum Laser Source: Experiment and Simulation," Laser Photon. Rev. **14**(6), (2020).

9. A. Al-kadry, M. El Amraoui, Y. Messaddeq, and M. Rochette, "Two octaves mid-infrared supercontinuum generation in As_2Se_3 microwires," Opt. Express **22**(25), 31131 (2014).

10. N. Singh, D. D. Hudson, Y. Yu, C. Grillet, S. D. Jackson, A. Casas-Bedoya, A. Read, P. Atanackovic, S. G. Duvall, S. Palomba, B. Luther-Davies, S. Madden, D. J. Moss, and B. J. Eggleton, "Midinfrared supercontinuum generation from 2 to 6 µm in a silicon nanowire," Optica **2**(9), 797 (2015).

11. R. Kormokar, M. H. M. Shamim, and M. Rochette, "High-order analytical formulation of soliton self-frequency shift," J. Opt. Soc. Am. B **38**(2), 466 (2021).

12. A. Al-Kadry and M. Rochette, "Maximized Soliton Self-Frequency Shift in Non-Uniform Microwires by the Control of Third-Order Dispersion Perturbation," J. Light. Technol. **31**(9), 1462–1467 (2013).

13. M. Y. Koptev, E. A. Anashkina, A. V. Andrianov, V. V. Dorofeev, A. F. Kosolapov, S. V. Muravyev, and A. V Kim, "Widely tunable mid-infrared fiber laser source based on soliton self-frequency shift in microstructured tellurite fiber," Opt. Lett. **40**(17), 4094 (2015).

14. I. Alamgir, M. H. M. Shamim, W. Correr, Y. Messaddeq, and M. Rochette, "Mid-infrared soliton self-frequency shift in chalcogenide glass," Opt. Lett. **46**(21), 5513 (2021).

15. J.-C. Gauthier, M. Olivier, P. Paradis, M.-F. Dumas, M. Bernier, and R. Vallée, "Femtosecond tunable solitons up to 4.8 µm using soliton self-frequency shift in an InF3 fiber," Sci. Rep. **12**(1), 15898 (2022).

16. B. Li, M. Wang, K. Charan, M. Li, and C. Xu, "Investigation of the long wavelength limit of soliton self-frequency shift in a silica fiber," Opt. Express **26**(15), 19637 (2018).

17. J. P. Gordon, "Theory of the soliton self-frequency shift," Opt. Lett. **11**(10), 662 (1986).

18. R. Kormokar, M. H. M. Shamim, and M. Rochette, "Energy conversion efficiency from a high-order soliton to fundamental solitons in the presence of Raman scattering," J. Opt. Soc. Am. B **40**(2), 412 (2023).

19. Q. Ran, H. Li, Q. Wang, and Y. Zhang, "Self-compression of mJ pulses to 10 fs in a hollow-core waveguide: effects of higher-order dispersion," J. Opt. Soc. Am. B **39**(3), A1 (2022).

20. Kai Choong Chan and Hai Feng Liu, "Short pulse generation by higher order soliton-effect compression: effects of optical fiber characteristics," IEEE J. Quantum Electron. **31**(12), 2226–2235 (1995).

21. M. D. Pelusi and Hai-Feng Liu, "Higher order soliton pulse compression in dispersion-decreasing optical fibers," IEEE J. Quantum Electron. **33**(8), 1430–1439 (1997).

22. Q. Li, K. Senthilnathan, K. Nakkeeran, and P. K. A. Wai, "Nearly chirp- and pedestal-free pulse compression in nonlinear fiber Bragg gratings," J. Opt. Soc. Am. B **26**(3), 432 (2009).

23. R. H. Stolen, J. Botineau, and A. Ashkin, "Intensity discrimination of optical pulses with birefringent fibers," Opt. Lett. **7**(10), 512 (1982).

24. J.-L. Tapié and G. Mourou, "Shaping of clean, femtosecond pulses at 1053 μm for chirped-pulse amplification," Opt. Lett. **17**(2), 136 (1992).

25. O. Pottiez, E. . Kuzin, B. Ibarra-Escamilla, and F. M. Martínez, "Easily tuneable nonlinear optical loop mirror including low-birefringence, highly twisted fibre with invariant output

polarisation," Opt. Commun. **229**(1–6), 147–159 (2004).

26. P. Beaud, W. Hodel, B. Zysset, and H. Weber, "Ultrashort pulse propagation, pulse breakup, and fundamental soliton formation in a single-mode optical fiber," IEEE J. Quantum Electron. **23**(11), 1938–1946 (1987).

27. Y. Kodama and A. Hasegawa, "Nonlinear pulse propagation in a monomode dielectric guide," IEEE J. Quantum Electron. **23**(5), 510–524 (1987).

28. K. Tai, N. Bekki, and A. Hasegawa, "Fission of optical solitons induced by stimulated Raman effect," Opt. Lett. **13**(5), 392 (1988).

29. L. F. Mollenauer, R. H. Stolen, and J. P. Gordon, "Experimental Observation of Picosecond Pulse Narrowing and Solitons in Optical Fibers," Phys. Rev. Lett. **45**(13), 1095–1098 (1980).

30. J. Satsuma and N. Yajima, "B. Initial Value Problems of One-Dimensional Self-Modulation of Nonlinear Waves in Dispersive Media," Prog. Theor. Phys. Suppl. **55**, 284–306 (1974).

31. M. H. M. Shamim, I. Alamgir, and M. Rochette, "Soliton Order Preservation for Self-Frequency Shift With High Efficiency and Broad Tunability," J. Light. Technol. **41**(5), 1539–1544 (2023).

32. Y. Matsuo, N. Nishizawa, M. Mori, and T. Goto, "Characteristics of Wavelength Tunable Femtosecond Soliton Pulse Generation Using Femtosecond Pump Laser and Polarization Maintaining Fiber," Opt. Rev. **7**(4), 309–316 (2000).

33. W. J. Tomlinson, R. H. Stolen, and C. V. Shank, "Compression of optical pulses chirped by self-phase modulation in fibers," J. Opt. Soc. Am. B **1**(2), 139 (1984).

34. A. A. Amorim, M. V. Tognetti, P. Oliveira, J. L. Silva, L. M. Bernardo, F. X. Kärtner, and H. M. Crespo, "Sub-two-cycle pulses by soliton self-compression in highly nonlinear photonic crystal fibers," Opt. Lett. **34**(24), 3851 (2009).

35. A. Ben Salem, R. Cherif, and M. Zghal, "Soliton-self compression in highly nonlinear chalcogenide photonic nanowires with ultralow pulse energy," Opt. Express **19**(21), 19955 (2011).

36. T. Inoue and S. Namiki, "Pulse compression techniques using highly nonlinear fibers," Laser Photon. Rev. **2**(1–2), 83–99 (2008).

37. R. Kormokar and M. Rochette, "Soliton self-frequency shift prediction in amplifying fibers using the moment method," J. Opt. Soc. Am. B **41**(7), 1628 (2024).

38. M. H. M. Shamim, I. Alamgir, W. Correr, Y. Messaddeq, and M. Rochette, "Soliton Self-Frequency Shift in a Cascade of Silica, Fluoride, and Chalcogenide Fibers," J. Light. Technol. 1–7 (2024).

39. A. M. Al-kadry and M. Rochette, "Mid-infrared sources based on the soliton self-frequency shift," J. Opt. Soc. Am. B **29**(6), 1347 (2012).

40. M. Rochette, "The tapering of optical fibers," in *Mid-Infrared Fiber Photonics*, S. Jackson, R. Vallee, and M. Bernier, eds. (Elsevier, 2021).

41. I. Alamgir and M. Rochette, "Thulium-doped fiber laser mode-locked by nonlinear polarization rotation in a chalcogenide tapered fiber," Opt. Express **30**(9), 14300 (2022).

42. L. Li, N. Abdukerim, and M. Rochette, "Chalcogenide optical microwires cladded with fluorine-based CYTOP," Opt. Express **24**(17), 18931 (2016).

43. L. Li, A. Al-Kadry, N. Abdukerim, and M. Rochette, "Design, fabrication and characterization of PC, COP and PMMA-cladded As_2Se_3 microwires," Opt. Mater. Express **6**(3), 912 (2016).

44. A. Al-Kadry, M. El Amraoui, Y. Messaddeq, and M. Rochette, "Mode-locked fiber laser based on chalcogenide microwires," Opt. Lett. **40**(18), 4309 (2015).

45. E. Meyer-Scott, A. Dot, R. Ahmad, L. Li, M. Rochette, and T. Jennewein, "Power-efficient production of photon pairs in a tapered chalcogenide microwire," Appl. Phys. Lett. **106**(8), (2015).

46. A. Dot, E. Meyer-Scott, R. Ahmad, M. Rochette, and T. Jennewein, "Converting one photon into two via four-wave mixing in optical fibers," Phys. Rev. A **90**(4), 043808 (2014).

47. R. Ahmad and M. Rochette, "All-Chalcogenide Raman-Parametric Laser, Wavelength Converter, and Amplifier in a Single Microwire," IEEE J. Sel. Top. Quantum Electron. **20**(5), 299–304 (2014).

48. J.-C. Beugnot, R. Ahmad, M. Rochette, V. Laude, H. Maillotte, and T. Sylvestre, "Reduction and control of stimulated Brillouin scattering in polymer-coated chalcogenide optical microwires," Opt. Lett. **39**(3), 482 (2014).

49. A. Velazquez-Benitez, R. Ahmad, T. North, M. Gorjan, J. Hernandez-Cordero, and M. Rochette, "All-Optical Broadband Variable Optical Attenuator Based on an As2Se3 Microwire," IEEE Photonics Technol. Lett. **25**(7), 697–700 (2013).

50. C. Baker and M. Rochette, "Birefringence Engineering and High Nonlinearity in Eccentric-Core As2Se3-PMMA Microtapers," J. Light. Technol. **31**(1), 171–176 (2013).

51. C. Baker and M. Rochette, "High Nonlinearity and Single-Mode Transmission in Tapered

Multimode $\hbox{As}_{2}\hbox{Se}_{3}$-PMMA Fibers," IEEE Photonics J. **4**(3), 960–969 (2012).

52. C. Baker and M. Rochette, "A generalized heat-brush approach for precise control of the waist profile in fiber tapers," Opt. Mater. Express **1**(6), 1065 (2011).

53. R. Ahmad and M. Rochette, "Photosensitivity at 1550 nm and Bragg grating inscription in As2Se3 microwires for sensing applications," in *Advanced Photonics* (OSA, 2011), p. SOWE1.

54. R. Ahmad, M. Rochette, and C. Baker, "Fabrication of Bragg gratings in subwavelength diameter As2Se3 chalcogenide wires," Opt. Lett. **36**(15), 2886 (2011).

55. C. Baker and M. Rochette, "Highly nonlinear hybrid AsSe-PMMA microtapers," Opt. Express **18**(12), 12391 (2010).

56. M. Rezaei, G. T. Zeweldi, M. H. M. Shamim, and M. Rochette, "Single-mode optical fiber couplers made of fluoride glass," Opt. Express **31**(17), 27183 (2023).

57. B. Gholipour, S. R. Elliott, M. J. Müller, M. Wuttig, D. W. Hewak, B. E. Hayden, Y. Li, S. S. Jo, R. Jaramillo, R. E. Simpson, J. Tominaga, Y. Cui, A. Mandal, B. J. Eggleton, M. Rochette, M. Rezaei, I. Alamgir, H. M. Shamim, R. Kormokar, A. Anjum, G. T. Zeweldi, T. S. Karnik, J. Hu, S. O. Kasap, G. Belev, and A. Reznik, "Roadmap on chalcogenide photonics," J. Phys. Photonics **5**(1), 012501 (2023).

58. M. Rezaei, M. H. M. Shamim, M. El Amraoui, Y. Messaddeq, and M. Rochette, "Nonlinear chalcogenide optical fiber couplers," Opt. Express **30**(12), 20288 (2022).

59. M. Rezaei and M. Rochette, "All-chalcogenide single-mode optical fiber couplers," Opt. Lett. **44**(21), 5266 (2019).

60. F. Tavakoli, A. Rekik, and M. Rochette, "Broadband and Wavelength-Dependent Chalcogenide Optical Fiber Couplers," IEEE Photonics Technol. Lett. **29**(9), 735–738 (2017).

61. A. Anjum and M. Rochette, "All-fiber nonlinear multimode interference saturable absorber in reflection mode," Opt. Fiber Technol. **74**, 103092 (2022).

62. K. Zhang and M. Rochette, "All-Fiber Saturable Absorber Using Nonlinear Multimode Interference in a Chalcogenide Fiber," J. Light. Technol. **38**(22), 6321–6326 (2020).

63. K. Zhang, I. Alamgir, and M. Rochette, "Mid-infrared compatible tunable bandpass filter based on multimode interference in chalcogenide fiber," J. Light. Technol. **38**(4), 857–863 (2020).

64. K. Zhang, Y.-A. Peter, and M. Rochette, "Chalcogenide Fabry–Perot Fiber Tunable Filter," IEEE Photonics Technol. Lett. **30**(23), 2013–2016 (2018).

65. A. Salehiomran and M. Rochette, "A Frequency Domain Design Approach for the Generation of Arbitrary Transfer Function Based on Generalized Optical Transversal Filters," J. Light. Technol. **31**(3), 407–413 (2013).

66. M. Rochette, "All-optical PMD monitor for optical signals at 40 Gb/s and beyond," in *2009 IEEE LEOS Annual Meeting Conference Proceedings* (IEEE, 2009), pp. 393–394.

67. J. Qiu, K. Sun, M. Rochette, and L. R. Chen, "Reconfigurable All-Optical Multilogic Gate (xor, and, and or) Based on Cross-Phase Modulation in a Highly Nonlinear Fiber," IEEE Photonics Technol. Lett. **22**(16), 1199–1201 (2010).

68. F. Vanier, F. Côté, M. El Amraoui, Y. Messaddeq, Y.-A. Peter, and M. Rochette, "Low-threshold lasing at 1975 nm in thulium-doped tellurite glass microspheres," Opt. Lett.

40(22), 5227 (2015).

69. F. Vanier, Y.-A. Peter, and M. Rochette, "Cascaded Raman lasing in packaged high quality As2S3 microspheres," Opt. Express **22**(23), 28731 (2014).

70. F. Vanier, M. Rochette, N. Godbout, and Y.-A. Peter, "Raman lasing in As2S3 high-Q whispering gallery mode resonators," Opt. Lett. **38**(23), 4966 (2013).

71. M. I. Kayes, N. Abdukerim, A. Rekik, and M. Rochette, "Free-running mode-locked laser based dual-comb spectroscopy," Opt. Lett. **43**(23), 5809 (2018).

72. M. Imrul Kayes and M. Rochette, "Fourier transform spectroscopy by repetition rate sweeping of a single electro-optic frequency comb," Opt. Lett. **43**(5), 967 (2018).

73. N. Abdukerim, I. Alamgir, and M. Rochette, "Pulse characterization by cross-phase modulation in chalcogenide glass," Opt. Lett. **43**(19), 4771 (2018).

74. N. Abdukerim, I. Alamgir, and M. Rochette, "All-fiber frequency-resolved optical gating pulse characterization from chalcogenide glass," Opt. Lett. **43**(14), 3228 (2018).

75. I. Alamgir, N. Abdukerim, and M. Rochette, "In situ fabrication of far-detuned optical fiber wavelength converters," Opt. Lett. **44**(18), 4467 (2019).

76. M. Rochette, "Design and fabrication of nonlinear optical waveguides for far-detuned wavelength conversion to the mid-infrared," Adv. Opt. Technol. **7**(5), 321–326 (2018).

77. M. R. Fernández-Ruiz, L. Lei, M. Rochette, and J. Azaña, "All-optical wavelength conversion based on time-domain holography," Opt. Express **23**(17), 22847 (2015).

78. T. Godin, Y. Combes, R. Ahmad, M. Rochette, T. Sylvestre, and J. M. Dudley, "Far-detuned mid-infrared frequency conversion via normal dispersion modulation instability in

chalcogenide microwires," Opt. Lett. **39**(7), 1885 (2014).

79. A. Pasquazi, R. Ahmad, M. Rochette, M. Lamont, B. E. Little, S. T. Chu, R. Morandotti, and D. J. Moss, "All-optical wavelength conversion in an integrated ring resonator," Opt. Express **18**(4), 3858 (2010).

80. I. Alamgir, M. Hosne Mobarok Shamim, W. Correr, Y. Messaddeq, and M. Rochette, "Supercontinuum generation optimization in a dispersion-varying chalcogenide fiber," Opt. Commun. **565**, 130685 (2024).

81. D. D. Hudson, S. Antipov, L. Li, I. Alamgir, T. Hu, M. El Amraoui, Y. Messaddeq, M. Rochette, S. D. Jackson, and A. Fuerbach, "Toward all-fiber supercontinuum spanning the mid-infrared," Optica **4**(10), 1163 (2017).

82. A. Al-Kadry, L. Li, M. El Amraoui, T. North, Y. Messaddeq, and M. Rochette, "Broadband supercontinuum generation in all-normal dispersion chalcogenide microwires," Opt. Lett. **40**(20), 4687 (2015).

83. A. Al-kadry, C. Baker, M. El Amraoui, Y. Messaddeq, and M. Rochette, "Broadband supercontinuum generation in As2Se3 chalcogenide wires by avoiding the two-photon absorption effects," Opt. Lett. **38**(7), 1185 (2013).

84. M. I. Kayes and M. Rochette, "Precise Distance Measurement by a Single Electro-Optic Frequency Comb," IEEE Photonics Technol. Lett. **31**(10), 775–778 (2019).

85. M. Imrul Kayes and M. Rochette, "Optical frequency comb generation with ultra-narrow spectral lines," Opt. Lett. **42**(14), 2718 (2017).

86. T. North, A. Al-Kadry, and M. Rochette, "Analysis of Self-Pulsating Sources Based on Cascaded Regeneration and Soliton Self-Frequency Shifting," IEEE J. Sel. Top. Quantum

Electron. **20**(5), 612–618 (2014).

87. T. North and M. Rochette, "Regenerative self-pulsating sources of large bandwidths," Opt. Lett. **39**(1), 174 (2014).

88. T. North and M. Rochette, "Analysis of Self-Pulsating Sources Based on Regenerative SPM: Ignition, Pulse Characteristics and Stability," J. Light. Technol. **31**(23), 3700–3706 (2013).

89. T. North and M. Rochette, "Raman-induced noiselike pulses in a highly nonlinear and dispersive all-fiber ring laser," Opt. Lett. **38**(6), 890 (2013).

90. T. North and M. Rochette, "Broadband self-pulsating fiber laser based on soliton self-frequency shift and regenerative self-phase modulation," Opt. Lett. **37**(14), 2799 (2012).

91. T. North and M. Rochette, "Fabrication and characterization of a pulsed fiber ring laser based on As2S3," Opt. Lett. **37**(4), 716 (2012).

92. K. Sun, M. Rochette, and L. R. Chen, "Output characterization of a self-pulsating and aperiodic optical fiber source based on cascaded regeneration," Opt. Express **17**(12), 10419 (2009).

93. M. Rochette, L. R. Chen, K. Sun, and J. Hernandez-Cordero, "Multiwavelength and Tunable Self-Pulsating Fiber Cavity Based on Regenerative SPM Spectral Broadening and Filtering," IEEE Photonics Technol. Lett. **20**(17), 1497–1499 (2008).

94. I. Alamgir, M. Rezaei, and M. Rochette, "Fiber optical parametric oscillator made of soft glass," Opt. Lett. **47**(14), 3451 (2022).

95. M. Rezaei and M. Rochette, "All-chalcogenide ring fiber laser," Opt. Fiber Technol. **71**,

102900 (2022).

96. N. Abdukerim, L. Li, M. El Amraoui, Y. Messaddeq, and M. Rochette, "2 μ m Raman fiber laser based on a multimaterial chalcogenide microwire," Appl. Phys. Lett. **110**(16), (2017).

97. N. Abdukerim, L. Li, and M. Rochette, "Chalcogenide-based optical parametric oscillator at 2 μm," Opt. Lett. **41**(18), 4364 (2016).

98. A. Salehiomran, R. Modirnia, B. Boulet, and M. Rochette, "Optical Parametric Oscillator Longitudinal Modes Suppression Based on Smith Predictor Control Scheme," IEEE Trans. Control Syst. Technol. **22**(5), 2064–2072 (2014).

99. A. Salehiomran and M. Rochette, "A Nonlinear Model for the Operation of Fiber Optical Parametric Oscillators in the Steady State," IEEE Photonics Technol. Lett. **25**(10), 981–984 (2013).

100. R. Ahmad and M. Rochette, "Raman lasing in a chalcogenide microwire-based Fabry–Perot cavity," Opt. Lett. **37**(21), 4549 (2012).

101. M. Gorjan, T. North, and M. Rochette, "Model of the amplified spontaneous emission generation in thulium-doped silica fibers," J. Opt. Soc. Am. B **29**(10), 2886 (2012).

102. R. Ahmad and M. Rochette, "Chalcogenide microwire based Raman laser," Appl. Phys. Lett. **101**(10), (2012).

103. R. Ahmad and M. Rochette, "Chalcogenide optical parametric oscillator," Opt. Express **20**(9), 10095 (2012).

104. R. Ahmad and M. Rochette, "High efficiency and ultra broadband optical parametric four-wave mixing in chalcogenide-PMMA hybrid microwires," Opt. Express **20**(9), 9572 (2012).

105. W. Lin, M.-H. Bussières-Hersir, M. Auger, A. Vincelette, and M. Rochette, "3 kW forward-pumped fiber laser via pump recycler," Appl. Opt. **62**(17), 4490 (2023).

106. N. Abdukerim, M. I. Kayes, A. Rekik, and M. Rochette, "Bidirectional mode-locked thulium-doped fiber laser," Appl. Opt. **57**(25), 7198 (2018).

107. C. Jia, B. J. Shastri, N. Abdukerim, M. Rochette, P. R. Prucnal, M. Saad, and L. R. Chen, "Passively synchronized Q-switched and mode-locked dual-band Tm3+:ZBLAN fiber lasers using a common graphene saturable absorber," Sci. Rep. **6**(1), 36071 (2016).

108. C. Jia, X. Liang, M. Rochette, and L. R. Chen, "Alternate Wavelength Switching in a Widely Tunable Dual-Wavelength Tm-Doped Fiber Laser at 1900 nm," IEEE Photonics J. **7**(4), 1–7 (2015).

109. A. Salehiomran and M. Rochette, "An All-Pole-Type Cavity Based on Smith Predictor to Achieve Single Longitudinal Mode Fiber Lasers," IEEE Photonics Technol. Lett. **25**(21), 2141–2144 (2013).

110. J. Hernandez-Cordero, L. R. Chen, and M. Rochette, "Multirate and Dual-Wavelength Semiconductor Fiber Laser," IEEE Photonics Technol. Lett. **21**(12), 808–810 (2009).

111. G. P. Agrawal, *Nonlinear Fiber Optics*, 4th ed. (AcademicPress, San Diego, 2007).

112. Frederick Wooten, *Optical Properties of Solids* (Academic Press, 1972).

113. P. A. Franken, A. E. Hill, C. W. Peters, and G. Weinreich, "Generation of Optical Harmonics," Phys. Rev. Lett. **7**(4), 118–119 (1961).

114. K. J. Blow and D. Wood, "Theoretical description of transient stimulated Raman scattering in optical fibers," IEEE J. Quantum Electron. **25**(12), 2665–2673 (1989).

115. R. H. Stolen, W. J. Tomlinson, H. A. Haus, and J. P. Gordon, "Raman response function of silica-core fibers," J. Opt. Soc. Am. B **6**(6), 1159 (1989).

116. O. V. Sinkin, R. Holzlohner, J. Zweck, and C. R. Menyuk, "Optimization of the split-step fourier method in modeling optical-fiber communications systems," J. Light. Technol. **21**(1), 61–68 (2003).

117. H. Haus and M. Islam, "Theory of the soliton laser," IEEE J. Quantum Electron. **21**(8), 1172–1188 (1985).

118. J. W. Choi, B.-U. Sohn, G. F. R. Chen, D. K. T. Ng, and D. T. H. Tan, "Soliton-effect optical pulse compression in CMOS-compatible ultra-silicon-rich nitride waveguides," APL Photonics **4**(11), (2019).

119. N. González-Baquedano, I. Torres-Gómez, N. Arzate, A. Ferrando, and D. E. Ceballos-Herrera, "Pulse quality analysis on soliton pulse compression and soliton self-frequency shift in a hollow-core photonic bandgap fiber," Opt. Express **21**(7), 9132 (2013).

120. K.-T. Chan and W.-H. Cao, "Enhanced compression of fundamental solitons in dispersion decreasing fibers due to the combined effects of negative third-order dispersion and Raman self-scattering," Opt. Commun. **184**(5–6), 463–474 (2000).

121. Q. Li, J. N. Kutz, and P. K. A. Wai, "Cascaded higher-order soliton for non-adiabatic pulse compression," J. Opt. Soc. Am. B **27**(11), 2180 (2010).

122. P. Ciąćka, A. Rampur, A. Heidt, T. Feurer, and M. Klimczak, "Dispersion measurement of ultra-high numerical aperture fibers covering thulium, holmium, and erbium emission wavelengths," J. Opt. Soc. Am. B **35**(6), 1301 (2018).

123. T. Boilard, R. Vallée, and M. Bernier, "Probing the dispersive properties of optical fibers

with an array of femtosecond-written fiber Bragg gratings," Sci. Rep. **12**(1), 4350 (2022).

124. Y. Wu, M. Meneghetti, J. Troles, and J.-L. Adam, "Chalcogenide Microstructured Optical Fibers for Mid-Infrared Supercontinuum Generation: Interest, Fabrication, and Applications," Appl. Sci. **8**(9), 1637 (2018).

125. P. Balla, S. Buch, and G. P. Agrawal, "Effect of Raman scattering on soliton interactions in optical fibers," J. Opt. Soc. Am. B **34**(6), 1247 (2017).

126. R. Radhakrishnan, P. Tchofo Dinda, and G. Millot, "Efficient control of the energy exchange due to the Manakov vector-soliton collision," Phys. Rev. E **69**(4), 046607 (2004).

127. M. F. Saleh, A. Armaroli, A. Marini, and F. Biancalana, "Strong Raman-induced noninstantaneous soliton interactions in gas-filled photonic crystal fibers," Opt. Lett. **40**(17), 4058 (2015).

128. B. J. Hong and C. C. Yang, "Interactions between femtosecond solitons in optical fibers," J. Opt. Soc. Am. B **8**(5), 1114 (1991).

129. F. Luan, D. V. Skryabin, A. V. Yulin, and J. C. Knight, "Energy exchange between colliding solitons in photonic crystal fibers," Opt. Express **14**(21), 9844 (2006).

130. M. Erkintalo, G. Genty, and J. M. Dudley, "Experimental signatures of dispersive waves emitted during soliton collisions," Opt. Express **18**(13), 13379 (2010).

131. J. Liao, Y. Gao, Y. Sun, L. Ma, Z. Lu, and X. Li, "Effects of third-order dispersion on temporal soliton compression in dispersion-engineered silicon photonic crystal waveguides," Photonics Res. **8**(5), 729 (2020).

132. K. C. Chan and H. F. Liu, "Effect of third-order dispersion on soliton-effect pulse

compression," Opt. Lett. **19**(1), 49 (1994).

Appendix

MATLAB function for solving GNLSE:

```
function [A, Af] = GNLSE_SSFM_func(E, L, h_ratio, gamma0, taushock, chi, fR, betas,
maxorder, wrel, dt, lossw, shift, npts, nplots)

% Francois St-Hilaire, MEng, McGill University

% Adapted from a J.M. Dudley code (Femto-ST)
% This function solves the GNLSE
% With a SSFM and adaptive step size method.
% Inputs : E = Initial time domain envelope
    % L= Fiber length
    % h_ratio = Inverse of max phase shift per step
    % gamma0 = NL parameter at center wavelength
    % taushock = shock timescale
    % chi = Ramain gain FT(h_R)
    % fR = Raman fraction
    % betas = vector of beta coefficients [B2 B3 B4 B5...]
    % maxorder = max beta order
    % wrel = relative angular frequency vector centered at wo
    % w0 = reference frequency
    % t = time vector
    % dt = time increment
    % lossw = losses [1/m]
    % shift = shift amount from frequency window
    % npts = number of discretization points
    % nplots = number of saved propagation points

% Outputs: A = Pulse envelope saved at nplots points in z
    % Af = Pulse spectrum saved at nplots points in z

Efftshift = (E);
Z = 0;
ind1 = [(2:npts) 1];
ind2 = [npts (1:npts-1)];
sel = (L/(nplots-1));
plotsel = sel;
plotn = 1;
A = zeros(nplots,npts);                    % time-domain field array
Af = zeros(nplots,npts);                  % freq-domain field array
E = fftshift(E);
EFT = fft(E);
A(1,:) = fftshift(E);
Af(1,:) = fftshift(circshift((EFT),shift));
```

```
beta = 0;
    for ii = 2: maxorder
    beta = beta + betas (ii-1).*wrel.^(ii)./factorial(ii);
    end
beta = fftshift (beta);

k = 0;
    while z<L
    k = k+1;
    %% Nonlinear step
    AO = E;
    peakP = max(abs (E).^2);
    h = (1./(gamma0.*peakP))./h_ratio;
    IFT = fft (abs (AO).^2);
    Iz = (1-fR)*(abs (AO).^2)+fR*ifft(chi.*IFT);
    NLfn = AO.*Iz;
    A1 = AO-h/2*1/(2*dt).*gamma0.*taushock.*(NLfn (ind1)-NLfn(ind2));
    IFT = fft(abs (A1).^2);
    Izh = (1-fR)*(abs (A1).^2)+fR*ifft(chi.*IFT);
    NLfn = A1.*Izh;
    A1 = AO-h.*1i.*gamma0.*A1.*(Izh-Iz)-h.*1./(2.*dt).*gamma0.*
    taushock.*(NLfn(ind1)-NLfn (ind2));
    E = A1.*exp(-1i.*gamma.*h.*Iz);
    %% Dispersion birefringence step
    Betaop = exp(-1i*h*beta);
    EFT = circshift(fft (E), shift);
    EFT = EFT.*betaop;
    %% Include loss
    EFT = EFT.*(fftshift(exp(-lossw.*h))
    E = ifft (circshift (EFT,-shift));
    z = z+h;
    %% save
        if (z > plotsel)
        plotsel = plotsel+sel;
        plotn = plotn+1;
        A(plotn,:) = fftshift (E);
        Af (plotn,:) = fftshift (EFT);
        end
    end
end
```